International Scientific-Technical and Production Journal

The Paton WELDING JOURNAL

September 2006 # 9

English translation of the monthly «Avtomaticheskaya Svarka» (Automatic Welding) journal published in Russian since 1948

Founders: *E.O. Paton Electric Welding Institute of the NAS of Ukraine International Association «Welding»* ***Publisher:*** *International Association «Welding»*

Editor-in-Chief B.E.Paton

Editorial board:

Yu.S.Borisov V.F.Grabin
Yu.Ya.Gretskii A.Ya.Ishchenko
B.V.Khitrovskaya V.F.Khorunov
I.V.Krivtsun
S.I.Kuchuk-Yatsenko
Yu.N.Lankin V.K.Lebedev
V.N.Lipodaev L.M.Lobanov
V.I.Makhnenko A.A.Mazur
V.F.Moshkin O.K.Nazarenko
I.K.Pokhodnya I.A.Ryabtsev
Yu.A.Sterenbogen N.M.Voropai
K.A.Yushchenko
A.T.Zelnichenko

International editorial council:

N.P.Alyoshin (Russia)
B.Braithwaite (UK)
C.Boucher (France)
Guan Qiao (China)
U.Diltey (Germany)
P.Seyffarth (Germany)
A.S.Zubchenko (Russia)
T.Eagar (USA)
K.Inoue (Japan)
N.I.Nikiforov (Russia)
B.E.Paton (Ukraine)
Ya.Pilarczyk (Poland)
D. von Hofe (Germany)
Zhang Yanmin (China)
V.K.Sheleg (Belarus)

Promotion group:
V.N.Lipodaev, V.I.Lokteva
A.T.Zelnichenko (exec. director)
Translators:
I.N.Kutianova, V.N.Mironenko,
T.K.Vasilenko, N.V.Yalanskaya
Editor
N.A.Dmitrieva
Electron galley:
I.S.Batasheva, T.Yu.Snegiryova

Address:
E.O. Paton Electric Welding Institute,
International Association «Welding»,
11, Bozhenko str., 03680, Kyiv, Ukraine
Tel.: (38044) 287 67 57
Fax: (38044) 528 04 86
E-mail: journal@paton.kiev.ua
http://www.nas.gov.ua/pwj

State Registration Certificate
KV 4790 of 09.01.2001

Subscriptions:
$324, 12 issues per year,
postage and packaging included.
Back issues available.

All rights reserved.
This publication and each of the articles contained herein are protected by copyright. Permission to reproduce material contained in this journal must be obtained in writing from the Publisher.
Copies of individual articles may be obtained from the Publisher.

CONTENTS

SCIENTIFIC AND TECHNICAL

Lobanov L.M., Kirian V.I., Knysh V.V. and **Prokopenko G.I.** Improvement of fatigue resistance of welded joints in metal structures by high-frequency mechanical peening (Review) 2

Gretsky Yu.Ya. Main aspects of weldability of structural cast irons 9

Skulsky V.Yu. Effect of the degree of alloying of heat-resistant chromium steels on hardness of metal within the welded joint zone 17

Shonin V.A., Mashin V.S., Khaskin V.Yu. and **Nedej T.N.** Residual stresses in butt joints of thin sheets from alloy AMg6 after arc and laser-arc welding 20

Denisevich E.A. Calculation technique for defining parameters of soldered seam solidification 25

Ulshin V.A., Kharlamov M.Yu., Borisov Yu.S. and **Astakhov E.A.** Dynamics of movement and heating of powder in detonation spraying of coatings 29

INDUSTRIAL

Lankin Yu.N., Moskalenko A.A., Tyukalov V.G., Kuran R.I. and **Popov S.V.** Electroslag welding of blast furnace housing 35

Poznyakov V.D., Kasatkin S.B. and **Dovzhenko V.A.** Structure and cold resistance of welded joints in steel 09G2S after repair welding 37

Klimpel A., Lisiecki A., Janicki D. and **Stano S.** High power diode laser welding of aluminum alloy EN AW-1050 A 43

BRIEF INFORMATION

Kozulin S.M., **Sushchuk-Slyusarenko I.I.** and **Lychko I.I.** Influence of ESC parameters on the quality of reconditioned gear teeth 47

Cooperation raises investigation efficiency and reduces costs 50

Developed at PWI 46, 51, 52

© PWI, International Association «Welding», 2006

IMPROVEMENT OF FATIGUE RESISTANCE OF WELDED JOINTS IN METAL STRUCTURES BY HIGH-FREQUENCY MECHANICAL PEENING (REVIEW)

L.M. LOBANOV[1], **V.I. KIRIAN**[1], **V.V. KNYSH**[1] and **G.I. PROKOPENKO**[2]
[1]E.O. Paton Electric Welding Institute, NASU, Kiev, Ukraine
[2]G.V. Kurdyumov Institute of Metal Physics, NASU, Kiev, Ukraine

Results of studying the effectiveness of application of high-frequency mechanical peening (HFMP) to improve the fatigue resistance of welded joints on steels of different strength classes and aluminium alloys have been generalized. General regularities are established of variation of fatigue resistance of welded joints as a result of HFMP, determined by the mechanical properties of the material, level of concentration of working stresses, asymmetry of external loading cycle, magnitude and sign of the residual stresses induced by treatment in the concentrator zone. A procedure is developed for calculation-based prediction of the effectiveness of HFMP, depending on the above factors.

Keywords: steels, aluminium alloys, welded joints, stress concentration, residual stresses, fatigue resistance, high-frequency mechanical peening, ultrasonic treatment

High-frequency mechanical peening (HFMP) is a further step in development of the technologies of surface plastic deformation of metal. Such technologies include shot hardening, roll treatment, hammering with one- and multi-striker tools with pneumatic or electromechanical drive, plastic reduction, explosion treatment, etc. [1--5]. They are mainly applied to improve the fatigue resistance of machine parts and welded joints of structures for various applications.

The possibility of applying ultrasonic technology for improvement of service properties of welded structures was substantiated for the first time at the N.E. Bauman MHTU in 1959 in work [6], which is devoted to ultrasonic treatment of welded joints for redistribution of residual stresses. Later on studies of lowering residual stresses in welded joints by ultrasonic treatment were continued in [7–11], and were aimed primarily at ensuring the dimensional stability of welded structure elements in service. At the same time, studied was the influence of ultrasonic oscillations on the change of inner stresses in steels, shock action of the tool on the degree of metal strengthening, its wear resistance, inducing residual stresses on its surface [12--15]. In [16] the mechanism of ultrasonic impact treatment was studied. In individual studies attempts were made to use ultrasonic technologies to improve the fatigue resistance of machine parts [17, 18], corrosion fatigue strength of steel [19], as well as surfaced propeller shafts [20].

Ultrasonic technology consists of impact treatment of the metal surface by high-strength strikers, mechanical oscillations of which are excited by ultrasonic generator through a radiator (converter of electrical oscillations into mechanical vibrations). Depending on the addressed technology tasks, standard or specially developed ultrasonic generators and tools with magnetostriction or piezo-ceramic radiators of 0.3–2.5 kW output power are used [10, 21–24].

Surface plastic deformation by shocks following each other at a high frequency, can be applied by three schematics (Figure 1).

In the first case (Figure 1, *a*), the work tool in the form of a hardened sphere, hard alloy or diamond tip is rigidly coupled with the edge of ultrasonic concentrator. The entire oscillatory system is pressed to the surface with force F_{st} = 100--200 Pa and slides freely along the guides. At treatment of strong materials the tool bounces off the part surface, so that effective treatment requires significant pressing forces F_{st} and residual power of ultrasonic radiators.

In the second case (Figure 1, *b*) the working tool is not rigidly coupled to the concentrator and is fastened in special mandrels. It is called an intermediate striker element. At the end of 1960s and beginning of 1970s such a treatment method was proposed by scientists of the USA, Ukraine and Russia. In this case, the entire radiator also slides freely in the guides and is pressed to the part surface with force F_{st}, which is, however, much smaller than in the first case and usually equal to 30–50 Pa. This gives rise to forced oscillations of the intermediate element in a certain gap (~ 0.01 mm), which is automatically set at excitation of ultrasonic oscillations. From the diagram it is seen that presence of a gap is a mandatory condition for development of vibrations of the deforming element. Investigations showed that intensive plastic deformation of the metal surface proceeds with such a method of transfer of ultrasonic energy into the treated item.

Also known is a method of surface treatment using ultrasound (Figure 1, *c*). In this case, the radiator is rigidly fixed (for instance, in the machine tool carriage) and a fixed gap $h \approx 0.01$ mm is set between the intermediate element and the part surface, while the element proper is pressed up to the end face of ultra-

© L.M. LOBANOV, V.I. KIRIAN, V.V. KNYSH and G.I. PROKOPENKO, 2006

sonic wave guide with a small force of about 10 Pa. When ultrasonic oscillations are switched on, the element starts vibrating in the gap at a certain frequency.

From Figure 1 it is seen that in the second and third cases this frequency is essentially lower than that of ultrasonic oscillations and is equal to 1–3 kHz on average. When multi-striker tools with striker number of 3 to 10 and more are used the total shock frequency can be higher than these values, because of the strikers vibrating out of phase and their vibrations in the gap being of a stochastic nature. Nonetheless, only the first case can be regarded as ultrasonic treatment proper, when the tool oscillates at ultrasonic frequency. In the second and third cases the ultrasound is used only as a drive for forced oscillations of the tool in a certain gap. Such a type of treatment is called ultrasonic impact treatment. In foreign publication the term «ultrasonic peening» is used. However, as the tool oscillates in the gap with a lower frequency than that of ultrasound, it is more appropriate to use the term of «high-frequency mechanical peening» (HFMP).

First investigations of the applicability of ultrasonic technologies to increase the fatigue resistance of welded joints were conducted at the E.O. Paton Electric Welding Institute in 1982. HFMP was used for treatment of the zone of weld to base metal transition in welded joints, which is prone to fatigue damage, by the schematic given in Figure 1, *b*. A sphere of 16 mm diameter was used as the striker. Its mechanical vibrations were induced by a batch-produced magnetostriction transducer PMS-15A-18 and ultrasonic generator UZG-10M. Frequency of ultrasonic oscillations was equal to 27.5 kHz. Such a kind of HFMP resulted in intensive plastic deformation of metal to the depth of 0.3–1.0 mm, depending on the kind of material and its mechanical properties. This led to ensuring a smoother transition from the weld to the base metal, and, therefore, to lowering of the concentration of working stresses in the joint. In addition, compressive residual stresses developed in the surface layers of the treated section. As a result of such a treatment, cyclic fatigue life of butt joints of low-carbon steel increased 18 to 20 times.

By the initiative of Prof. Boris E. Paton, in 1983 the E.O. Paton Electric Welding Institute started systematic studies associated with development of a readily adaptable-to-fabrication process of increasing the fatigue resistance of welded joints of high-strength steel for application in ship-building structures. They were conducted jointly with TsNII «Prometej» (St.-Petersburg, Russia) and «Severnoe Mashinostroitelnoe Predpriyatie» — SMP (Severodvinsk, Russia). Investigations were conducted on two types of welded joints — butt joint and joint with transverse fillet welds. HFMP of welded joints was performed at SMP using a compact manual tool with magnetostriction transducer and multielement working tool [21, 22]. The source of oscillation excitation was a thyristor ultrasonic generator device UTGU-1.2-27 with up to 1.2 kW output power. The following HFMP parameters were varied during investigations: amplitude of ultrasonic radiator oscillations rate of tool displacement; number of tool passes; width of treated zone.

A high effectiveness of HFMP of welded joints on high-strength structural steels was established at different kinds of loading in a broad range of variation of the coefficient of cycle asymmetry (Table, Nos. 2–8). Variation of the width of the treated zone of the joints did not have any influence on the cyclic fatigue life of the joints. Width of the treated zone in the range of 4 to 7 mm, and tool displacement rate of about 0.5 m/min were selected as the optimum strengthening parameters. The following turned out to be the main causes for increase of the cyclic fatigue life and endurance limit of welded joints at HFMP:

• relieving the tensile and inducing the favourable residual compressive stresses in the concentrator zones;

• lowering the concentration of working stresses;

• deformation strengthening of the surface layer of metal.

It should be noted that the work of the E.O. Paton Electric Welding Institute of the NAS of Ukraine on development of the HFMP process and technology, as well as evaluation of the effectiveness of their ap-

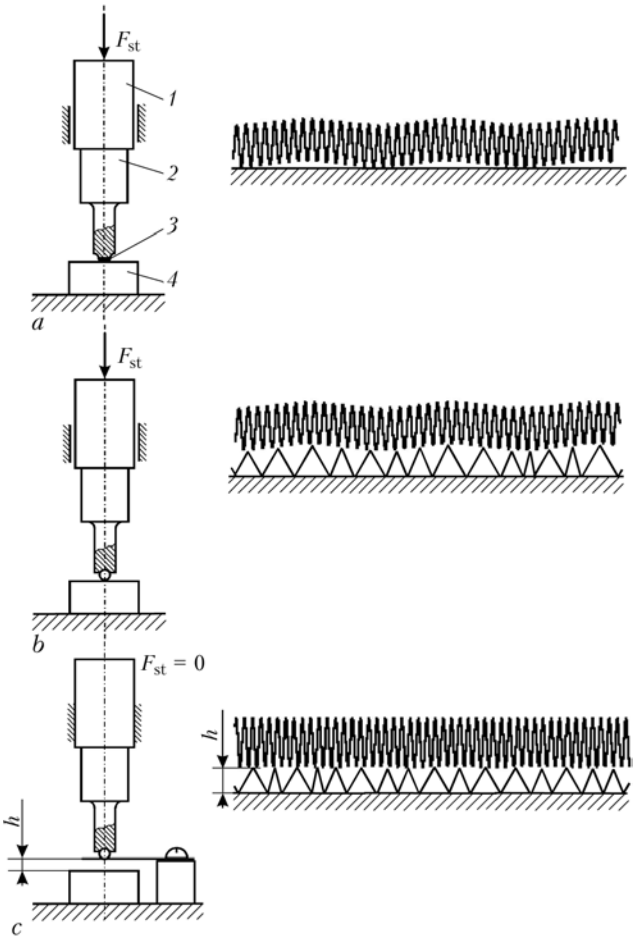

Figure 1. Schematic of HFMP implantation [10]: *a* — rigid fastening of the damping element (striker) with acoustic system pressing with force F_{st}; *b* — the same, but with passive deforming element; *c* — with oscillations of deforming element in gap *h*; *1* — radiator; *2* — waveguide; *3* — deforming element; *4* — treated part

Effectiveness of HFMP of welded joints

No.	Grade of welded metal	σ_t, MPa	Thickness, mm	Joint type	Test conditions		σ_R, MPa, at $N = 2\cdot10^6$ cycle		$\Delta\sigma_R$, MPa / %	Information source, note
					Kind of loading	R_σ	Initial	As-treated		
1	St.3sp	458	20	Butt	Tension	0	140	220	80 / 57	[3, 25–28, 43, 55]
2	High-strength	>1000	20	Same	Bending	--1	180	300	120 / 66	Same
3		>1000	20	»	Same	--1	140	260	120 / 86	»
4		>1000	20	»	Tension	0	110	140	30 / 27	Same, weld convexity exceeded standard tolerance
5		>1000	20	»	Bending	0.6	135	175	40 / 30	[3, 25–28, 43, 55, 56], σ_R at $N = 5\cdot10^6$ cycle
6		>1000	30	With transverse stiffeners welded by fillet welds	Same	--1	80	240	160 / 200	Same
7		>1000	30	Same	»	0	110	230	120 / 109	
8		>1000	30	»	»	0.6	80	105	25 / 31	
9	Austenitic	–	80	»	»	0	110	205	95 / 86	[25, 35, 43], σ_R at $N = 4\cdot10^6$ cycle
10		–	80	With longitudinal strap welded on by fillet welds	»	0	100	190	90 / 90	[25, 35, 43], full penetration joint
11	Å690	823–876	9.5	Tee	»	0.1	135	397	260 / 192	[33]
12		836	9.5	Butt	Tension	0.1	129	224	95 / 74	[34]
13	Å460	589	10	Tee	Bending	0.1	168	290	122 / 73	[34]
14	Aluminuim alloy 6061 T6	290	8	Butt	Tension	0.1	71	86	15 / 21	[34]
15	Aluminuim alloy AA5083	335	8	Overlap joint with transverse fillet welds	Same	0.1	19.8	35.1	15.3 / 78	[53]
16		335	8	With longitudinal straps welded by fillet welds	»	0.1	35	68	33 / 95	[53]
17	WELDOX 420	573	20	With transverse stiffeners welded by fillet welds	Bending	0.1	198	327	129 / 65	[47], wrought element of 5 mm diameter
18		573	20	Same	Same	0.1	198	341	143 / 72	[47], wrought element of 3 mm diameter
19	Ò Ì ÑÐ	σ_y = 420	20	»	»	0.1	178	351	173 / 97	[46]
20	St3sp	460	30	»	Tension	0	113	167	54 / 49	PWI data
21	St3sp	460	30	»	Same	0	113	164	51 / 48	PWI data. Tool with peizoeceramic transducer. Wrought element diameter of 3 mm
22		460	30	»	»	0	113	164	51 / 48	Same, 2 mm diameter of wrought element
23	09G2SYuCh	550	14	With longitudinal stiffeners welded by fillet welds	»	0	96	156	60 / 62	PWI data

Table (cont.)

No.	Grade of welded metal	σ_t, MPa	Thickness, mm	Joint type	Test conditions		σ_R, MPa, at $N = 2\cdot10^6$ cycle		$\Delta\sigma_R$, MPa / %	Information source, note
					Kind of loading		Initial			
24	15KhSND	520	14	With longitudinal stiffeners welded by fillet welds	Tension	0	86	180	94 / 110	PWI data
25	WELDOX 700	800	6	Same	Same	0.1	86	190	104 / 120	[54]
26	Q235B	435.5	8	Butt	»	0.1	148.5	234	85.5 / 57	[52], tool with piezoceramic transducer
27		435.5	8	Cruciform	4-point bending	0.25	142.5	234	91.5 / 64	
28		435.5	8	Same	Same	–0.5	165	282	117 / 71	

plication to increase the fatigue resistance of welded joints, was performed jointly with TSNII «Prometej» and SMP [25–31].

Results of these investigations were used at TsNII «Prometej» when writing technological recommendations on HFMP application to improve the fatigue resistance of welded joints of ship hull structures.

Further investigations at the E.O. Paton Electric Welding Institute on expansion of HFMP applications to improve the fatigue resistance of welded structures were conducted jointly with the enterprises and organizations of Mintyazhmash, Minaviaprom, Mintransstroj, State Administration of Railway Transportation of Ukraine and other departments. Several studies were performed jointly with the «Severnaya» Science-Technology Company — SNTC (Severodvinsk, Russia), GIPRONIIAVIAPROM (Moscow, Russia), NKMZ (Kramatorks, Ukraine), Institute of Welding (France), etc. Results of these and other experimental studies of the effectiveness of HFMP application to increase the fatigue resistance of welded joints on steels of different strength classes and aluminium alloys are given in the Table. They include the experimental studies performed by the Institute of Welding of France in 1990–1991 on samples with transverse fillet welds (high-strength steel) strengthened using HFMP at the E.O. Paton Electric Welding Institute. Results of this work are presented in the joint publication [32]. Further on, similar studies were continued by the Institute of Welding of France on welded joints of low-carbon steel and aluminium alloy [33, 34]. They showed that the effectiveness of HFMP of welded joints decreases with lowering of steel strength (see the Table, Nos. 11, 13).

In 1992–1993 the E.O. Paton Electric Welding Institute together with GIPRONIIAVIAPROM conducted investigations of the rationality of applying HFMP of welded components from austenitic steels in construction of a cryogenic wind tunnel. It is established that in welded joints after HFMP the sites of fatigue crack initiation are the unwelded slots in the fillet weld roots, and not the zone of weld-to-base metal transition as usual. Based on the obtained investigation results (see the Table, Nos. 9, 10), recommendations were issued on design of welded components and HFMP application to the most heavily loaded elements of the cryogenic wind tunnel being designed [35].

In 1987–1993 the E.O. Paton Electric Welding Institute together with NKMZ (Kramatorsk) conducted studies of fatigue resistance of welded joints at cyclic compression. Such a loading mode is characteristic for the load-carrying elements of dragline excavator booms. It is shown that redistribution of residual welding stresses in the concentrator zones as a result of HFMP eliminates formation of fatigue cracks in weldments, characteristic for load-carrying elements of booms [36, 37].

Substantiation of HFMP application to improve the fatigue resistance of tubular weldments goes back to 1991–2001. In this case, HFMP technology was selected allowing for the features of the stress-strain state in the zone of the brace joining the girth of tubular structure elements. It is established that the positive influence of HFMP begins to be manifested in the region of fatigue lives greater than 10^4 cycles, and leads to a 2 times increase of endurance limit. Positive influence of HFMP of tubular connections is manifested both in terms of the criterion of crack initiation, and that of complete fracture [38, 39]. Study [40] substantiated the rationality of application and established the high effectiveness of HFMP for extension of the life of nodal connections in tubular truss welded structures, subjected to alternating loading in service. Positive effect is achieved irrespective of the degree of fatigue damage accumulated by a structure at the stage of structure operation before HFMP application.

Proceeding from the results of fatigue testing of large-scale welded models of connections of solid-wall span structures of a new type for railway bridges [41], obtained at the E.O. Paton Electric Welding Institute and experimental trials at the Voronezh Bridge Works and test ring railroad of VNII of Railway Transportation HFMP was recommended for application in bridge construction. By the decision of the Technical Council of State Administration of Railway Transportation of Ukraine, UkrPROEKTSTALKONSTRUKTSIYA included this type of treatment into the project documentation for experimental typical welded span structures of bridges for the railways of Ukraine. The necessary correction of HFMP process parameters was conducted allowing for the design features of welded connections of span structures.

In [26] it is established that anisotropy of plastic properties due to local plastic deformation of HFMP metal, does not lead to lowering of welded joint fracture toughness, characterized by critical crack tip opening displacement at low temperatures. This enabled regarding HFMP as a strengthening method which is not hazardous for the load-carrying capacity of welded structures, operated at lower climatic temperatures. More over, under the conditions of low climatic temperatures (to –60 °C) as shown in [42], at repeated-shock loading HFMP of welded joints of low-alloyed steels is the most effective measure to increase their fatigue resistance compared to other kinds of treatment (mechanical removal of weld reinforcement, argon-arc, explosion).

Starting from 1994–1995, the results of studies on increase of welded joint fatigue resistance under the impact of HFMP and development of the respective process equipment are reported in IIW Congresses [43, 44]. In 1997–1999 under IIW co-operative program «Testing the methods of strengthening treatments of welded joints» [45], the Department of Welded Structure Strength of the E.O. Paton Electric Welding Institute performed two studies under contracts with SNTC (Severodvinsk), which demonstrated HFMP advantages compared to pneumatic peening, shot blasting and argon-arc surface melting [46, 47]. Investigations were conducted on welded joints of Swedish low-alloyed steel WELDOX 420. HFMP process parameters were corrected to achieve the maximum effect (see the Table, Nos. 17, 18).

The considered test results were obtained on welded joints, HFMP of which was performed using equipment based on magnetostriction transducers [21, 22, 30–32, 44]. On the other hand, such work related to development of process equipment for HFMP of metals and welded structures using piezoceramic transducers has been performed in Ukraine for a long time [4, 23, 24, 48]. Application of piezoceramic radiators has a number of advantages, the main of which are improved efficiency of the units, lowering of their weight and power consumption, and absence of water cooling.

Such a unit was developed in Kiev at «Ultramet» enterprise with participation of the staff of the E.O. Paton Electric Welding Institute of the NAS of Ukraine [49–51]. Optimum power of the generators and radiators based on piezoceramics is in the range of 0.3 to 0.5 kW. The unit was tried out at the E.O. Paton Electric Welding Institute on welded joints of high-strength and low-carbon steel with transverse fillet welds. For comparison similar samples were treated by HFMP using tools with both the magnetostriction and piezoceramic transducers, both tool types having heads with striker-needles of 3 mm diameter. The features of tool heads on piezoceramic transducers are protected by patents [48–50] and USSR authors' certificates [23].

Process parameters (tool displacement rate, number of passes, width of the treated zone, force of tool clamping, amplitude of ultrasonic oscillations of the waveguide edge) of joint treatment were assumed to be identical for both tool types. Samples from high-strength steel were tested for three-point bending, and those from low-carbon steel — by axial loading. Investigations showed that at application of low-carbon steel use of a tool with magnetostriction or piezoceramic transducers leads to practically the same increase of endurance limits of the welded joint compared to the initial condition (see the Table, Nos. 20, 21). It is quite probable to achieve a somewhat higher efficiency of HFMP at treatment of high-strength steel welded joints using a tool with a magnetostriction transducer. An essential dependence of HFMP effect on its process parameters is also confirmed. Positive results were also obtained in China, when using equipment with piezoceramic transducers for HFMP of welded joints [52] (see the Table, Nos. 26–28).

HFMP can be applied to improve the fatigue resistance of welded joints on steels of different strength classes, including aluminium alloys. However, for aluminium alloy joints the optimum parameters of HFMP differ from parameters of treatment of steel welded joints. At optimum parameters of HFMP of aluminium alloy welded joints an increase of endurance limits of overlap joints with transverse and longitudinal welds by 78 and 95 % was obtained at $N = 2.10^6$ cycles, respectively (see the Table, Nos. 15, 16) [53]. On the other hand, treatment of aluminium alloy welded joints by the technology corresponding to that for similar welded joints of steels, increases the endurance limit by 21 % (see the Table, Nos. 12, 14) [34].

In [53] it is established that the effectiveness of HFMP of butt joints of AMg6 aluminium alloys depends on the power of ultrasonic generator and transducer, diameter of the applied needle-strikers and asymmetry of external loading cycle. One of the important conclusions from these studies consists in that in the case of aluminium alloy welded joints the best results are achieved when using ultrasonic unit with a piezoceramic transducer (consumed power of 0.3 kW) compared to magnetostriction ones.

A priori it is assumed that the highest HFMP effect is achieved at formation of compressive residual stresses in the concentrator zone, equal to or higher than the steel yield limit σ_y. The E.O. Paton Electric Welding Institute developed a procedure of calculation of the effectiveness of the methods of improving the welded joint fatigue life, which allows establishing the optimum value of the formed residual compressive stresses in the concentrator zone, at which the maximum increase of the welded joint endurance limit is

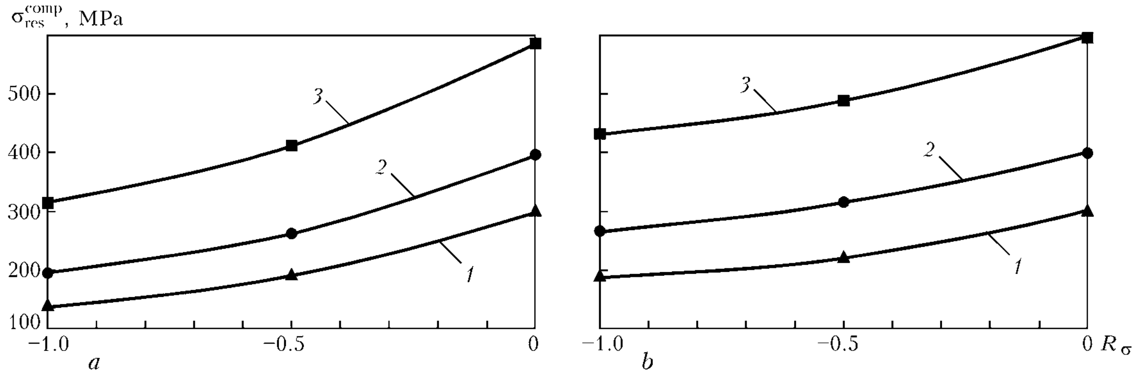

Figure 2. Dependence of HFMP induced optimum residual compressive stresses in the stress raiser zone on coefficient of asymmetry of external loading cycle at which the maximum increase of endurance limits is achieved: *a* — butt joint; *b* — joint with transverse fillet welds; *1–3* — low-carbon, low-alloyed and high-strength steels, respectively

achieved [3]. In this case, the mechanical properties of the material, concentration of working stresses, asymmetry of the external loading cycle, magnitude of compressive residual stresses formed by treatment in the concentrator zone, are taken into account. Analysis showed that in most of the cases the value of the residual compressive stresses should be in the range of (0.5–0.7)σ_y. Figure 2 shows the variation of optimum values of compressive residual stresses for two types of welded joints (butt and with transverse fillet welds) of steels of three strength classes — low-carbon (σ_y = 300 MPa), low-alloy (σ_y = 400 MPa) and high-strength (σ_y = 600 MPa), depending on the coefficient of asymmetry of the external loading cycle R_σ. The presented data are indicative of an essential influence of R_σ on the optimum value of compressive residual stresses formed in concentrator zones using HFMP, which provide the maximum possible increase of endurance limits and increase of cyclic fatigue life of welded joints. In the region of the impact of alternating loads the optimum value of compressive residual stresses generated by treatment is much lower than σ_y of the appropriate steel. It reaches the steel yield limit only at from-zero cycle (R_σ = 0). Thus, optimization of HFMP parameters allows achieving the maximum effect at an essential lowering of its labour consumption.

In conclusion it should be noted that HFMP is an efficient and cost-effective method to improve the fatigue resistance of welded joints of different strength classes and aluminium alloys. Effectiveness of HFMP of welded joints increases:

• with increase of the initial material strength. In case of butt joints on low-carbon steels increase of endurance limit $\Delta\sigma_R$ is equal to 57 (see the Table, No. 1), and for high-strength steel it is 74 % (No. 12). On joints with transverse fillet welds increase of $\Delta\sigma_R$ is equal to 65–72 (Nos. 17, 18), and those of high-strength steel 109 % (No. 7);

• for welded joints with a high initial concentration of working stresses due to the weld shape. While for butt joint of high-strength steel $\Delta\sigma_R$ = 66 (see the Table, No. 2), in the case of a joint with transverse fillet welds $\Delta\sigma_R$ = 200 % (No. 6);

• at lowering of the coefficient of asymmetry of the external loading cycle R_σ. Variation of R_σ from +0.6 to –1.0 leads to increase of $\Delta\sigma_R$ of high-strength steel welded joint with transverse fillet welds from 31 to 200 % (see the Table, Nos. 6–8). The same regularity is preserved also in butt joints of high-strength steel ($\Delta\sigma_R$ rises from 30 to 86 %, see Nos. 2, 3, 5).

The level of increase of welded joint fatigue resistance essentially depends on HFMP parameters. Their selection (PWI developed the appropriate procedure) allows achieving a quite significant increase of endurance limit $\Delta\sigma_R$.

HFMP of welded joints using equipment based on magnetostriction and peizoceramic transducers at identical treatment process parameters leads to practically the same increase of welded joint fatigue resistance of low and medium-strength steels. The advantage of magnetostriction transducers can be observed in the case of high-strength steels.

As a result of plastic deformation at HFMP, local strengthening of metal in the zone of weld to base metal transition does not lower the fracture toughness of welded joint as a whole, which is determined by the parameters of non-linear fracture mechanics (critical crack opening displacement) at low climatic temperatures (to –60 °C). This allows recommending HFMP technology for improvement of fatigue resistance of welded joints on metal structures operating at temperatures down to –60 °C.

Obtained results of experimental investigations of the effectiveness of HFMP application for improvement of the fatigue resistance of welded joints on steels of different classes of strength and aluminium alloys, experience of its application in ship-building, pilot-production trials in bridge-construction for the newly built and currently operated span structures and in other industries can be the basis for inclusion of this kind of cold working into the codes for welded structure design and fabrication.

1. Paton, B.E. (2000) Modern trends of improving the strength and life of welded structures. *The Paton Welding J.*, **9/10**, 2–8.
2. Trufyakov, V.I. (1998) Improvement of fatigue resistance of welded joints and structures. *Avtomatich. Svarka*, **11**, 11–19.
3. Trufyakov, V.I., Mikheev, P.P., Kudryavtsev, Y.F. (1995) *Fatigue strength of welded structures. Residual stresses and improvement treatments*. London: Harword Acad. Publ.

4. Lurie, G.B., Shtejnberg, Ya.I. (1971) *Strengthening-finishing treatment of functional surfaces of machine parts by surface plastic deformation*. Moscow: Mashinostroenie.
5. Kudryavtsev, I.V., Naumenkov, N.E. (1976) *Fatigue of welded structures*. Moscow: Mashinostroenie.
6. Mordvintseva, A.V. (1959) Ultrasonic treatment of welded joints to relieve the residual stresses. Application of ultrasound in welding engineering. In: *Transact. of N.E. Bauman MVTU*, Issue 45, 32--43.
7. Polotsky, I.G., Nedoseka, A.Ya., Prokopenko, G.I. et al. (1974) Lowering of residual welding stresses by ultrasonic treatment. *Avtomatich. Svarka*, **5**, 74–75.
8. Yanchenko, Yu.A., Sagalevich, V.M. (1978) Effect of ultrasonic treatment on relaxation of residual stresses and strains in high-strength steel welded joints. *Vestnik Mashinostroeniya*, **1**, 60–63.
9. Kholopov, Yu.V. (1973) Ultrasonic treatment of metal welded joints to relieve the residual stresses. *Svarochn. Proizvodstvo*, **12**, 20--23.
10. Prokopenko, G.I., Nedoseka, A.Ya., Gruzd, A.A. et al. (1995) Development and optimization of equipment and process of ultrasonic peening treatment of welded joints to relax the residual stresses. *Tekhnich. Diagnostika i Nerazrush. Kontrol*, **3**, 14–22.
11. Krivko, V.P., Prokopenko, G.I. (1979) Ultrasonic treatment of welded joints. *Svarochn. Proizvodstvo*, **5**, 32.
12. Pogodina-Alekseeva, K.M., Kremlev, E.M. (1967) Effect of ultrasonic oscillations on relieving of internal stresses in some steels. *Ultrazvuk. Tekhnika*, Issue 4, 28–33.
13. Nerubaj, M.S. (1968) Effect of ultrasonic oscillations of the tool on work hardening and residual stresses of the surface. *Vestnik Mashinostroeniya*, **10**, 65--67.
14. Stepanov, V.G., Statnikov, E.Sh., Klestov, M.I. et al. (1974) Residual stresses at strengthening of YuZ steel welded joints by ultrasonic peening tool. *Tekhnologiya Sudostroeniya*, **7**, 32--34.
15. Mukhanov, I.I., Golubev, Yu.M. (1966) Strengthening of steel parts by a ball vibrating with ultrasonic frequency. *Vestnik Mashinostroeniya*, **11**, 52--53.
16. Badalyan, V.G., Kazantsev, V.F., Statnikov, E.Sh. et al. (1979) Mechanism of ultrasonic impact treatment of welded joints. *Ibid*., **8**, 56–58.
17. Markov, A.I. (1975) Application of ultrasound in mechanical treatment and surface strengthening of hard-to-work materials. In: *Industrial application of ultrasound*. Moscow: Mashinostroenie; Sofia: Tekhnika.
18. Kulemin, A.V., Kononov, V.V., Stebelkov, I.A. (1981) Improvement of fatigue strength of parts by ultrasonic surface treatment. *Problemy Prochnosti*, **1**, 70–74.
19. Stepanov, V.G., Statnikov, E.Sh., Klestov, M.I. et al. (1975) Corrosion-fatigue strength of YuZ steel in strengthening by ultrasonic tool. *Tekhnologiya Sudostroeniya*, **1**, 70–74.
20. Kravtsov, T.G., Ryzhov, N.F., Statnikov, E.Sh. et al. (1981) Increase of fatigue resistance of hardfaced shafts by ultrasonic treatment. *Avtomatich. Svarka*, **10**, 35–38.
21. Statnikov, E.Sh., Zhuravlyov, L.V., Alekseev, A.F. (1975) *Ultrasonic head for deformation strengthening and relaxation treatment*. USSR author's cert. 472782.
22. Statnikov, E.Sh., Shevtsov, E.M., Kulikov, V.F. (1977) Ultrasonic impact tool for strengthening of welds and relaxation of residual stresses. In: *New physical methods of intensification of technological processes*. Moscow: Metallurgiya.
23. Prokopenko, G.I., Krivko, V.P. (1978) *Ultrasonic multibit tool*. USSR author's cert. 1143.
24. Krasovsky, T.A., Prokopenko, G.I., Tverdokhleb, A.F. *Device for ultrasonic treatment*. Pat. 8366 Ukraine. Publ. 29.03.96.
25. Trufyakov, V.I., Mikheev, P.P., Statnikov, E.Sh. et al. (1989) *Increase of fatigue strength of metal structure welded joints by ultrasonic peening treatment*: Inform. letter. Kiev: PWI.
26. Mikheev, P.P. (1990) Increase of fatigue resistance of metal structure welded joints by ultrasonic peening treatment. In: *Transact. of PWI on Problems of Welding and Special Electrometallurgy*. Kiev: Naukova Dumka.
27. Mikheev, P.P., Nedoseka, A.Ya., Parkhomenko, I.V. (1984) Efficiency of application of ultrasonic peening treatment to increase the fatigue resistance of welded joints. *Avtomatich. Svarka*, **3**, 4--7.
28. Mikheev, P.P., Nedoseka, A.Ya., Parkhomenko, I.V. et al. (1986) Increase of fatigue resistance of welded joints by ultrasonic peening treatment. In: *Ultrasonic oscillations and their effect on mechanical characteristics of structural materials*. Ed. by V.A. Kuzmenko. Kiev: Naukova Dumka.
29. Statnikov, E.Sh., Trufyakov, V.I., Mikheev, P.P. et al. *Method of treatment of welded metal structures*. USSR author's cert. 1420035. Filed 23.02.87. Publ. 30.08.88.
30. Paton, B.E., Lobanov, L.M., Statnikov, E.Sh. et al. *Method of ultrasonic peening treatment and operational technological complex for its realization*. Pat. 2031144 RF. Filed 11.05.90. Publ. 1995.
31. Paton, B.E., Lobanov, L.M., Statnikov, E.Sh. et al. *Method of ultrasonic peening treatment and operational technological complex for its realization*. Pat. 12741 Ukraine. Filed 11.05.90. Publ. 28.02.97.
32. Paton, B.E., Lobanov, L.M., Statnikov, E.Sh. et al. *Procede de travail par chocs aux ultra-sons et ensemble technologique operationnel pour le travail par chocs aux ultrasons*. Pat. 105608 France. Filed 08.05.90. Publ. 22.11.91.
33. Castellucci, P., Trufiakov, V.I., Mikheev, P.P. et al. (1991) Le martelage par ultrasons des soudures en acier HLE. *Soudage et Techniques Connexes*, 45(**5 / 6**), 31–37.
34. Janosh, I.I., Koneczny, H., Debiez, S. et al. (1995) Improvement of fatigue strength in welded joint (in HSS and in aluminium alloy) by ultrasonic hammer peening. *IIW Doc. 1594–95*.
35. Trufiakov, V.I., Mikheev, P.P., Kuzmenko, A.Z. et al. (1993) Methods of improvement of fatigue resistance in welded connections of wind tunnels. In: *Investigation of characteristics of steels for cryogenic wind tunnel*: Transact. of GIPRONIIAVIAPROM, Issue 33, 68--84.
36. Burenko, A.G., Dobykina, E.K., Mikheev, P.P. et al. (1993) Improvement of fatigue resistance in load-carrying of welded structures under cyclic compression. *Avtomatich. Svarka*, **3**, 8–12.
37. Kudryavtsev, Y.F., Trufiakov, V.I., Mikheev, P.P. et al. (1994) Increasing the fatigue strength of welded joints in cyclic compression. *IIW Doc XIII-1569–94*.
38. Mikheev, P.P., Garf, E.F., Kuzmenko, A.Z. et al. (1992) Improvement of fatigue resistance of tubular welded connections by ultrasonic peening treatment. *Avtomatich. Svarka*, **11 / 12**, 32--35.
39. Mikheev, P.P., Garf, E.F., Kuzmenko, F.Z. et al. (1996) Improvement of fatigue resistance of tubular welded connections by ultrasonic peening. *Int. J. Offshore and Polar Eng*., **6**, 304–307.
40. Garf, E.F., Litvinenko, A.E., Smirnov, A.Kh. (2001) Assessment of fatigue life of tubular connections subjected to ultrasonic peening treatment. *The Paton Welding J*., **2**, 16–19.
41. Kudryavtsev, Yu.F., Korshun, V.F., Kuzmenko, A.Z. (1989) Increasing the cyclic life of welded joints by ultrasonic peening treatment. *Avtomatich. Svarka*, **7**, 24--28.
42. Degtyarev, V.A., Shulginov, B.S. (2000) Assessment of efficiency of methods of increasing the fatigue resistance in welded joints subjected to impact loading under low temperature conditions. *Problemy Prochnosti*, **6**, 115–123.
43. Trufiakov, V.I., Mikheev, P.P., Kudryavtsev, Y.F. et al. (1995) Ultrasonic impact treatment of welded joints. *IIW Doc. XIII-1609–95*.
44. Statnikov, E.Sh., Trufiakov, V.I., Mikheev, P.P. et al. (1996) Specification for welded toe improvement by ultrasonic impact treatment. *IIW Doc. XIII-1617--96*.
45. Haagensen, P.I. (1994) Collaborative test program on improvement methods. *IIW Doc. XIII-WG2-30--94*.
46. Trufiakov, V.I., Statnikov, E.Sh., Mikheev, P.P. et al. (1998) The efficiency of ultrasonic impact treatment for improving the fatigue strength of welded joints. *IIW Doc. XIII-1745--98*.
47. Statnikov, E.Sh., Muktepavel, V.O., Trufiakov, V.I. et al. (2000) Comparison of ultrasonic impact treatment (UIT) and other fatigue life improvement methods. *IIW Doc. XIII-1817--00*.
48. Prokopenko, G.I., Kozlov, A.V. *Ultrasonic head for surface strengthening of metallic surfaces*. Pat. 13936 Ukraine. Publ. 25.04.97.
49. Prokopenko, G.I., Klejman, Ya.I., Kozlov, O.V. et al. *Device for ultrasonic impact treatment of metals*. Pat. 47536 Ukraine. Publ. 15.07.2002.
50. Prokopenko, G., Klejman, J., Kozlov, O. et al. *Device for ultrasonic peening treatment of metals*. Pat. 6467321.2002 USA.
51. Lobanov, L.M., Mikheev, P.P., Prokopenko, G.I. et al. *Method of high-frequency peening of metal structure welded joints*. Pat. 60390 Ukraine. Publ. 15.10.2003.
52. Lixing, H., Dongpo, W., Yujeng, Zh. et al. (2000) Investigation on improving fatigue properties of welded joints by ultrasonic peening method. *IIW Doc. XIII-1812–00*.
53. Trufyakov, V.I., Shonin, V.A., Mashin, V.S. et al. (2001) Application of high-frequency peening to improve the fatigue resistance of butt welded joints in aluminium alloys. *The Paton Welding J*., **7**, 6–10.
54. Haagensen, P.J., Statnikov, E.Sh., Lopez-Martinez, L. (1998) Introductory fatigue tests on welded joints in high strength steel and aluminium improved by various method including ultrasonic impact treatment (UIT). *IIW Doc. XIII-1748--98*.
55. Mikheev, P.P., Statnikov, E.Sh., Kuzmenko, A.Z. (1991) Improvement of fatigue resistance in metal structure welded joints by ultrasonic impact treatment. In: *Abstr. of Int. Conf. on Ultrasound in Technology of Machine-Building-91*. Arkhangelsk.
56. Aranovsky, D.E., Statnikov, E.Sh., Mikheev, P.P. (1991) Investigation of efficiency of ultrasonic impact treatment of typical welded joints. *Ibid*.

MAIN ASPECTS OF WELDABILITY OF STRUCTURAL CAST IRONS

Yu.Ya. GRETSKY
E.O. Paton Electric Welding Institute, NASU, Kiev, Ukraine

The role of composition, structure and mechanical properties of cast iron castings are considered from the view point of welding. The main factors are named, which determine considerable difficulties in making the composite readily workable welded joints in welding cast iron products without high preheating or subsequent heat treatment. The influence of the graphite phase and metal base oxidation products on the basic possibility of cast iron to form a welded joint is considered. Conditions of solidification and structure formation in the fusion zone are analyzed. Results of studying the influence of the thermal cycle of arc welding on the structure and properties of cast irons in the HAZ metal are analyzed. The concepts of the nature of near-weld cracks are presented, and the principles of prevention of tears and microcracks in the HAZ metal are set forth. The initial postulates for selection of the composition of the deposited metal and respective electrode consumables, and measures for lowering the susceptibility of nickel-based weld metal to pore formation are presented. A set of requirements to the quality of arc welding of cast iron is determined, and metallurgical and technological measures for ensuring the continuity, tightness, strength and treatability of welded joints are generalized.

Keywords: structural cast iron, chemical composition, structure, mechanical properties, weldability, arc welding, welded joint, fusion zone, HAZ, weld metal, near-weld cracks, porosity, joint quality, welding technology

Cast irons belong to the group of difficult-to-weld structural materials, because of the high susceptibility of welded joints to formation of different defects, difficulty of producing dense, equivalent and readily treatable welded joints. On the other hand, the need to apply welding of cast iron castings and parts of machines, continuous improvement of the metal quality and more stringent requirements made of welded joints, promote development of work in this field [1–4].

According to DSTU 3761–98 standard [5], «a material is regarded as weldable to an established degree by the given process and for a specific purpose, if at a certain welding procedure, metal continuity is achieved which guarantees compliance to the requirements made of welded joints both in terms of their own properties, and their influence on the structure, of which they are a component».

In this connection, the purpose of the work is generalization of the existing concepts of physical-metallurgical features of formation of joints on structural cast irons and their properties, definition of initial principles of development and selection of a rational welding technology. Susceptibility of cast iron joints to formation of various defects is manifested to the greatest degree under the conditions of arc welding without preheating or with a low local heating, so that the above issues refer only to such conditions.

Evaluation of the composition, structure and mechanical properties of cast irons from the viewpoint of welding. Cast iron is a polycomponent high-carbon iron alloy, solidifying with formation of an eutectic, highly sensitive to the cooling conditions and susceptible to formation of non-equilibrium structures, which abruptly increase the hardness, impair the treatability of welded joints and lower their technological strength [6–9]. Composition of cast irons of industrial grades in mechanical engineering castings features not only a high content of carbon (2.5–3.8 %), but also a sufficiently high concentration of silicon (1.2–3.8 %), phosphorus (up to 0.3 %) and sulphur (up to 0.15 %). In special-purpose thin-walled castings phosphorus content can be up to 0.5–0.7 % [10]. A characteristic feature of the structure of structural cast irons is presence of graphite inclusions and greater fraction of the eutectic component, including phosphide-cementite eutectic (Figure 1).

A feature of cast iron solidification is related to existence of two high-carbon phases: graphite (stable) and cementite (metastable phase). Direct precipitation of graphite from the liquid solution is probable only at very slow cooling of the melt — up to 0.5 °C / s [6]. It is clear that the conditions of welding do not promote formation of an austenite-graphite eutectic. Eutectoid transformation, similar to eutectic transformation in cast irons, proceeds by a stable system at such low cooling rates in the temperature interval of the lowest stability of austenite, which practically cannot be achieved under the actual conditions of welding.

The characteristic dependence of mechanical properties in the entire range of temperatures of the thermal cycle of welding is associated with the features of the composition and presence of inclusions of graphite and phosphide-cementite eutectic in the structure [11]. In the heating branch (starting from 400 °C) the tensile strength decreases abruptly and already by 700–800 °C it is equal to just 15–20 % of the initial value (Figure 2). The initial low relative elongation at the temperature above 900–950 °C becomes practically zero. Therefore, the lower limit of BTR (950 °C) is significantly lower than the equilibrium solidus of cast iron (1130 °C), and it practically coincides with melting temperature of the phosphide-cementite eutectic (954 °C).

© Yu.Ya. GRETSKY, 2006

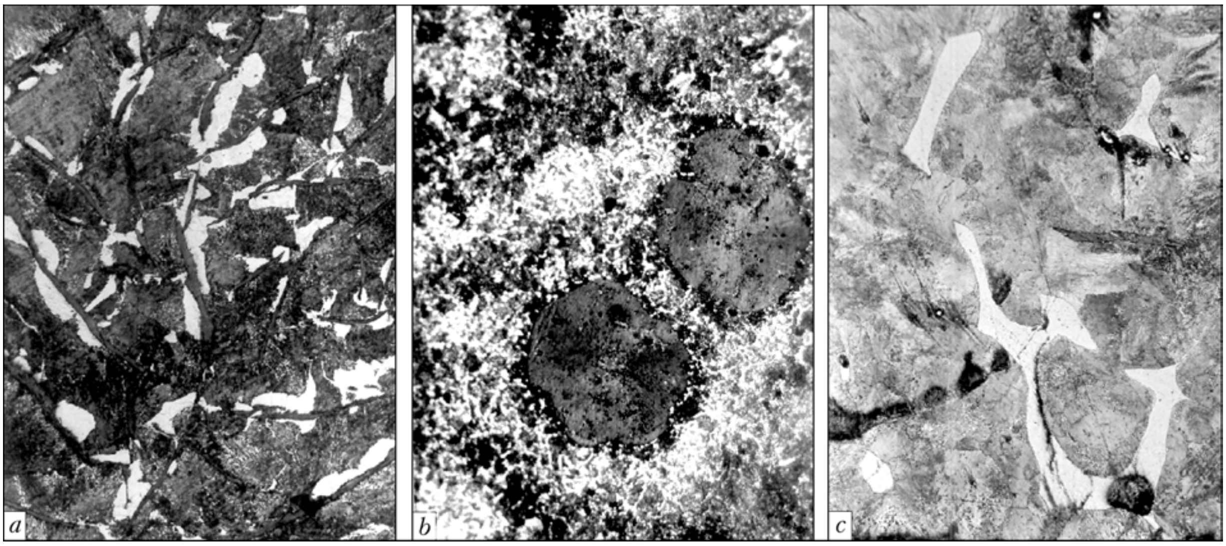

Figure 1. Microstructure of cast irons in castings: *a* — grey pearlite with plate-like graphite; *b* — high-strength pearlite with globular graphite; *c* — grey with phosphide-cementite eutectic (×250)

Considering the features of cast iron as the material being welded, it is necessary to note its high gas saturation. As regards simple gases, cast irons most often contain hydrogen, oxygen and nitrogen, as regards complex gases — their different compounds, such as CO, CO_2, C_mH_n, nitrides [10]. In the composition of the gas phase precipitating from cast iron at its melting, the content of hydrogen is the highest: 32 % H_2, 15 % N_2, 28 % CO, 14 % CO_2 and 11 % CH_4 [12]. In grey cast irons hydrogen is mainly concentrated in graphite inclusions and its content rises with increase of the quantity of graphite [13]. Residual content of low-diffusion forms of hydrogen in blast-furnace cast irons is estimated by the value of 30 cm^3 / 100 g and higher, in cast irons of cupola heat it is 0.7–30 cm^3 / 100 g, in malleable cast irons after annealing 0.6–12 cm^3 / 100 g [10]. Oxygen concentration in regular grey cast iron is not more than 0.01 %, nitrogen concentration is estimated as 0.001–0.015 % (in most of the cases — up to 0.008 %).

Basic capability of cast iron to form a welded joint. From this viewpoint, the influence of graphite inclusions [14, 15] should be primarily noted, which essentially are a non-melting component of base metal structure. In view of very high temperature of complete fracture of the graphite lattice (above 4000 °C) and stability of its complexes in the melt, coarse inclusions hinder base metal penetration by the arc, and then impair wetting of the melted surface by the weld pool metal. In their totality graphite inclusions create a real barrier between the metal base of surface-melted cast iron and liquid metal of the pool. An important condition of sound fusion is intensive cleaning of the molten surface from graphite inclusions through their dissolution by the pool metal. According to the theoretical estimates [16], at the initial stage of the cast iron joint formation dispersity of graphite inclusions is the limiting link in interaction of the weld pool with graphite at the interface. All the thin plate-like graphite inclusions characteristic of pearlite cast irons, coming to the interface, can be dissolved during the actual time of interaction of 1–2 s.

Structural cast irons have the most diverse structure, and differ by their dimensions and nature of

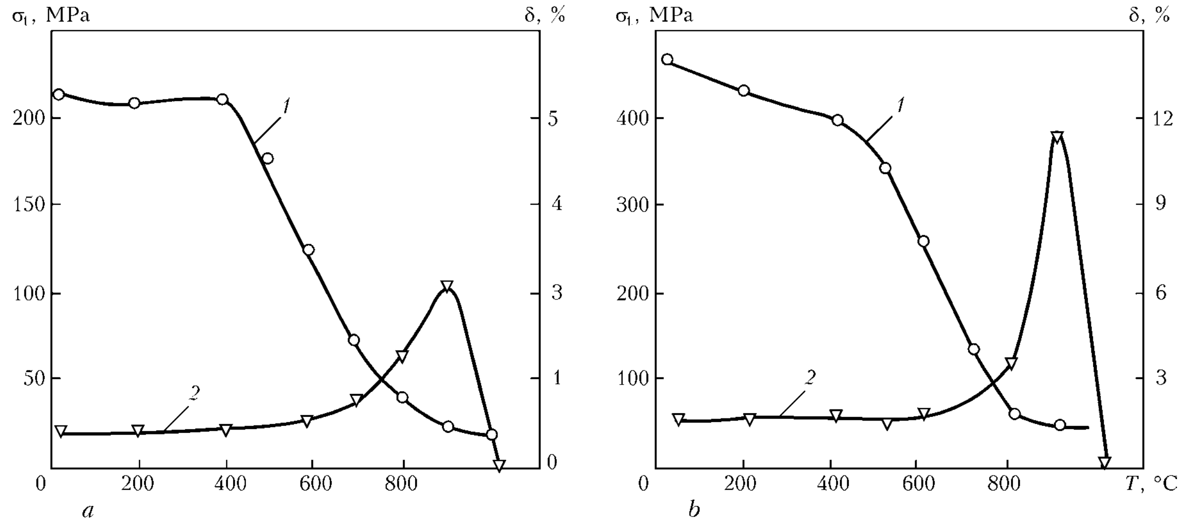

Figure 2. Nature of variation of tensile strength (*1*) and relative elongation (*2*) of cast irons in the temperature range of the process of HAZ metal formation in grey cast iron with plate-like graphite (*a*) and high-strength cast iron with globular graphite (*b*)

graphite distribution. Assessment calculations show [16] that to achieve universality, the developed or recommended ready electrode material should ensure the value of limit solubility of carbon by the weld pool on the level of 3.5–4.5 %. In this respect, electrode materials on iron-nickel and nickel base are preferable [15].

In addition to graphite, products of through-thickness oxidation of cast iron as a result of its long-term operation at high temperatures, particularly with frequent heat cycles and access of water vapours have a negative effect on weldability. Their main component is a complex silicon-containing compound of fayalite $2FeO \cdot SiO_2$, which is not dissolved by the weld pool [17]. Analysis of ternary oxide systems and their fusibility curves [18] provides an explanation of why the presence of slag containing calcium oxide is effective for weldability improvement. As a result of interaction of such a slag with the products of gas corrosion covering the molten surface of cast iron, CaO–FeO–SiO_2 ternary system forms in the presence of iron oxides, having an eutectic with solidification temperature 1030 °C below that of cast iron solidus. Such a measure facilitates the process of the matrix cleaning from refractory inclusions of fayalite. On this basis application of electrode materials with carbide-fluorite slag protection for arc welding of cast iron products after their long-term high-temperature gas corrosion has been recommended and successfully verified in practice [1, 17].

Features of the conditions of solidification and formation of metal structure in the fusion zone. Fusion zone consists of a section of partial melting of base metal and section of a variable composition from the side of weld metal [19]. On this basis we can conditionally assume that at the moment of formation of the joint proper, the fusion zone is located between the solidus isotherms of the base and weld metal. Ratio of solidus temperatures of the metal of weld pool and material being welded can essentially determine the mechanism of joint formation at the initial stages. According to the current concepts, in quasi-stationary arc welding, weld pool solidification starts from the established solid–liquid metal interphase, which is valid, if the temperatures of solidification of the base and pool metal are practically the same. However, in the case of a significant excess of weld pool solidus above the liquidus of the metal being welded, solidification of the first layers of the weld is possible at existence of a two-phase zone of the near-weld zone [20, 21].

Such a situation is highly probable in welding cast irons by steel and iron-nickel welds, because of a significant difference of solidification temperatures (Table). The validity of this assumption for cast irons is proved in [22], using Fe–C constitutional diagram. In cast iron welding by steel, carbon concentration in the variable composition zone abruptly decreases, and the liquidus value just as abruptly increases, respectively. On the other hand, the interval of liquid solidification becomes wider, as the value of the eutectic solidification temperature remains unchanged. Due to that, conditions are in place for concentrational overcooling of the liquid in the variable composition zone at a certain distance from the base metal–pool interphase. Here, formation of the solid phase is probable, with a simultaneous development of fusion zone microregions adjacent to it from the base metal side, in which solidification will be completed with a certain delay. This will have an adverse impact on process strength of the base metal in the partial melting section, primarily, because of its low resistance to the rising stresses in the formed joint.

When high-nickel electrode materials are used, the situation in the fusion zone changes significantly. Nickel is a strong graphitizer, increasing the temperature of a stable eutectic transformation in cast irons and simultaneously lowering the temperature of metastable transformation. In the presence of nickel, carbon concentration in the eutectic decreases right down to 2.2 % in Ni–C system. Coefficient of nickel diffusion in cast irons is quite high and is equal to $8.7 \cdot 10^{-5}$ cm^2 / s [23], in iron-carbon alloys it is almost identical to carbon as to diffusion mobility. Therefore, nickel rather deeply penetrates into the diffusion stirring zone, and the deeper, the higher is its concentration gradient. Providing nickel-based weld metal composition, it is possible to achieve a high degree of metal graphitization in the fusion zone (Figure 3), and avoid formation of regions of delayed solidification in the near-weld zone.

Values of equilibrium solidus and liquidus in structural cast irons and metal of iron and iron-nickel base single-pass weld

Material	Average content, wt.%					Temperature, °C	
	Fe	C	Si	Ni	Other	Solidus	Liquidus
Cast irons:							
SCh 20	Base	3.2	1.7	0.12	0.11 Cr	1125	1185
VCh 45-5	Same	3.1	1.8	0.40	0.07 Mg	1095	1170
Weld metal welded with electrodes:							
UONII-13 / 45	»	1.2	0.7	–	–	1365	1480
TsCh-4	»	1.0	0.6	–	8 V	1345	1435
OZZhN-1	60	0.8	–	35	–	1240	1350
Castolin 2240	20	1.2	0.5	Base	–	1230	1295

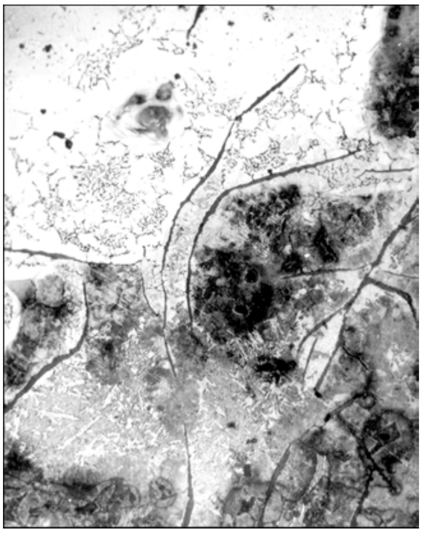

Figure 3. Microstructure of fusion zone metal without ledeburite in a welded joint made with a high-nickel electrode without preheating or subsequent heat treatment (×250)

Structure formation in the HAZ metal. Proceeding from the generally accepted definition, it should be assumed that cast iron HAZ forms as a result of base metal heating up to the temperature of melting of the graphite or austenite-cementite eutectic (1130–1140 °C). In such a case, cast iron in the HAZ metal would stay only in the solid state. However, because of the presence of graphite inclusions and microregions of phosphide-cementite eutectic scattered in the metal, not only the products of anisothermal decomposition of matrix austenite, but also metal microregions around the graphite inclusions solidified with whitening, where contact melting of the matrix occurred, are recorded in the HAZ metal (at a certain distance from the visible fusion line) (Figure 4). Products of the process of melting-solidification of inclusions of phosphide-cementite eutectic and phosphorus segregation on grain boundaries around these inclusions are also detected. The region of partial melting of HAZ metal is actually outlined by 950 °C isotherm, corresponding to the melting temperature of phosphide-cementite eutectic.

PWI studied the features of anisothermal decomposition of matrix austenite in cast irons with plate-like and globular graphite [24–27]. Conditions of sample heating and cooling by the thermal cycle of single-pass welding of thin plates without preheating were simulated using a fast-action dilatometer designed by PWI. Analysis of the plotted thermokinetic diagrams (Figure 5) showed that in the range of the actual cooling rates of 2–50 °C / s at $T < A_{c_3}$, austenite decomposition in cast iron proceeds in the pearlite and martensite regions. For the conditions of welding, the critical cooling rates in the range of the lowest stability of austenite have very small values — 9–10 °C / s for grey cast irons, and 2–3 for high-strength cast irons. Assessing these data for the conditions of welding, it may be stated that martensite formation in the HAZ metal is inevitable. Martensite transformation starts at relatively low temperatures (190–220 °C) and is not over with cooling to room temperature. At increase of heating and cooling rates the completeness of structural changes in the HAZ metal decreases, amount of residual austenite increases and the share of structural components forming as a result of contact melting of the matrix at graphite inclusions, decreases [27]. In this sense, increase of the rigidity of thermal welding cycles should be regarded as a positive factor. The main techniques for fulfillment of this condition is concentration of the heat source energy and lowering of welding heat input due to all its components, namely welding current, arc voltage, efficiency and welding speed. Such a complex of measures also allows achieving high temperature gradient in the HAZ, which is required to produce a narrower HAZ.

Nature and principles of near-weld crack prevention. A distinction should be made between cracks in the metal of the fusion zone and HAZ. The first, as a rule, are longitudinal and lead to tears (Figure 6). The second are microdefects of different orientation. Tears are found immediately after welding during equalizing of temperature in the joint. Their formation proceeds without any sound effect. Metallographic examination of the defective joints indicates that macro- and microcracks in the fusion zone run through sections with an eutectic. From consideration of the features of formation of cast iron joints at a higher temperature of weld pool metal solidification, it follows that under these conditions complete solidifica-

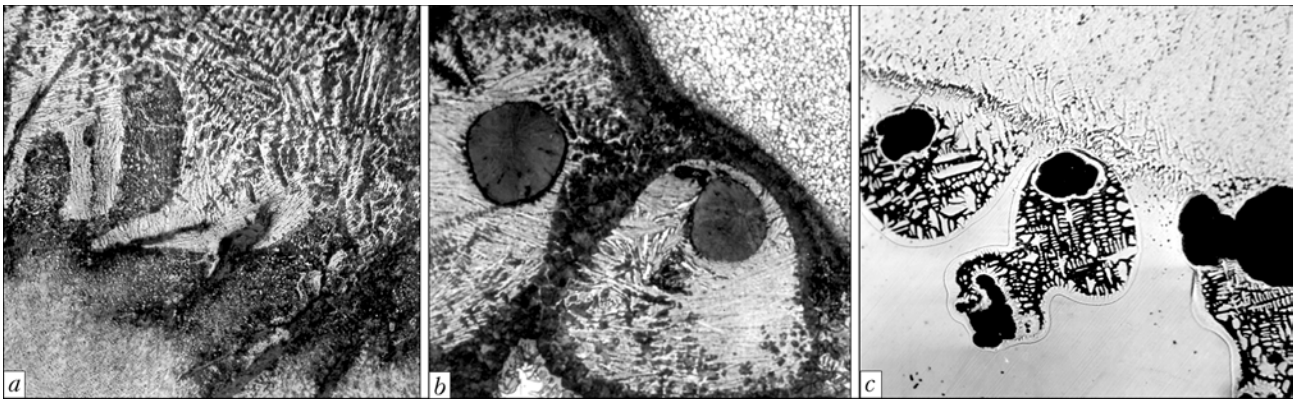

Figure 4. Typical microstructure of cast iron in the HAZ with products of liquid phase solidification after contact melting of the matrix of grey pearlite with plate-like (*a*), high-strength pearlite with globular graphite (*b*) and high-alloyed austenitic cast iron with graphite inclusions of a compact shape (*c*) (×250)

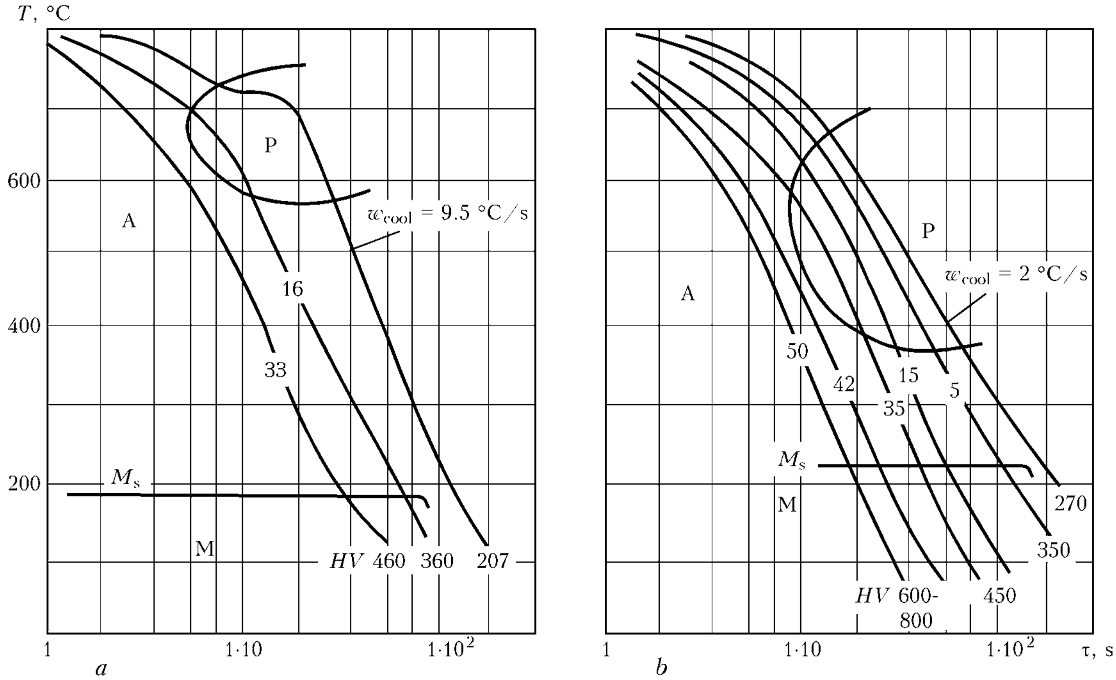

Figure 5. Thermokinetic diagrams of transformation of matrix austenite of pearlitic cast irons with plate-like (*a*) and globular (*b*) graphite after heating up to temperature of 1100 °C

tion of metal in the fusion zone can be over at the very end [22]. Studying the temperature dependence of strength and ductility characteristics of structural cast irons showed that the lower limit of BTR is close to 950 °C [27], being 300–400 °C lower than the solidus of iron- or iron-nickel based weld pool metal.

The above facts allow regarding the cracks in the fusion zone as hot cracks. Experimental data on the structure, properties and mode of fracture allowed defining the concept of the nature of this type of cracks [28]. The fusion zone during welded joint formation turns out to be the region of the lowest strength. Increasing stresses can quickly exceed the weak deformation ability of the fusion zone metal which is in BTR. Crack initiation is facilitated by presence of the last portions of the liquid phase. Because of the relatively small value of BTR lower limit for cast iron, fracture can also develop at subsolidus temperatures. Such a situation is the most probable at high values of heat input, when considerable areas of near-weld metal become involved in the deformation process.

Therefore, in order to prevent tears in the weld, it is necessary to ensure, at least simultaneity of these two processes, namely fusion zone metal going out of the state with very low strength properties in a certain section and completion of weld metal solidification in the same section. A series of experiments with the Lehigh University technological sample gave an idea about the range of optimum values of welding heat input (0.5–0.8 MJ / m) [28, 29]. In welding thick-walled cast iron parts (4–6 mm), which are the most susceptible to tearing, this condition is only satisfied in mechanized narrow-gap welding with small diameter wire (up to 1.2 mm).

Thus, approaches which should be the basis for development of effective technologies, are increase of the temperature of eutectic solidification in the variable composition zone (due to diffusion penetration of nickel and lowering of weld pool metal solidus).

Cast iron susceptibility to cracking in the HAZ metal depends on the initial structure of the matrix, shape of graphite phase and eutectic structure. This eliminates the possibility of describing the nature of cracking in the HAZ metal by one mechanism, referring them, for instance, to hot or cold cracks. Fracture sites are grain boundaries between the tips of closely located graphite plates and in the sites of graphite globule accumulation, eutectic arrays, sections of interdendrite graphite, inclusions of phosphide-cementite eutectics (Figure 7). Because of structural inhomogeneity, the cracking mechanisms are different in different microregions. On the other hand, the main of them, related to compositional and structural features of this cast iron type, predetermines the process of local fracture initiation and propagation.

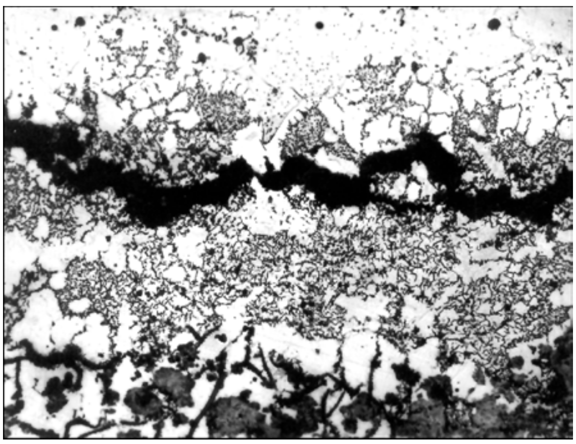

Figure 6. Fragment of microstructure of the fusion zone of grey cast iron welded joint with a longitudinal crack (tear) (×150)

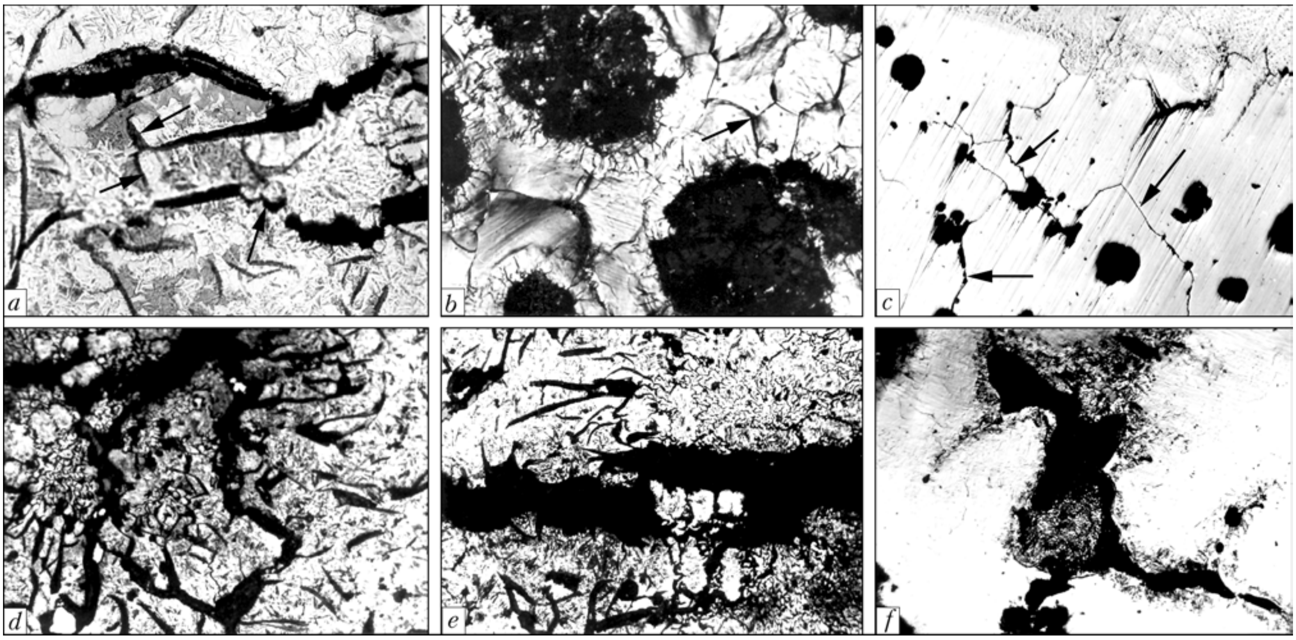

Figure 7. Microstructure of cast iron joints in the HAZ metal with fracture sites: *a*–*c* — boundaries of grains between graphite inclusions in grey, high-strength and austenitic cast irons, respectively (shown by arrows); *d* — eutectic rosettes; *e* — interdendritic grahite; *f* — phosphide-cementite eutectic (×150)

In grey cast irons plate-like inclusions play the role of stress raisers. If the deformation ability of the metal base is exhausted near their tips, cracking starts in the boundary microsections. Globular graphite does not have such a strong weakening action, so that the main mechanism of fracture in high-strength cast irons is different. The established concepts of the process of delayed fracture of hardening steels are, in general, applicable to description of the nature of cracking in the HAZ metal, but in cast irons with globular graphite the fracture process starts much earlier. It may occur already in the period of temperature leveling in the welded joint. Austenitic cast irons are also susceptible to intercyrstalline fracture, the nature of which is related mainly to impurity segregation.

The later does metal deformation in the HAZ start at welded joint cooling, the lower is the probability of formation of fracture sites and cracking. Lowering of weld metal melting temperature is an effective measure of reducing both the tempo of stress rise and their level. In this respect, the advantage of austenitic high-nickel weld metal compared to the ferritic weld metal, is obvious.

Initial principles of selection of the base of weld metal composition. Proceeding from the above principles of controlling the structure and properties of metal of the near-weld zone and measures to prevent cracking in them, a radical solution of the problem of producing high-quality joints in arc welding without the overall high preheating of the items, should be based on development and application of nickel-base electrode materials. Nickel content in single-pass welds on thin-walled items or in multilayer welds in welding of massive castings, should be not lower than 50 % [30]. In this case additional alloying of welding consumables with manganese and copper is rational for lowering of their melting temperature.

Without special modification, the graphite phase in welds on nickel-iron base is concentrated on grain boundaries in the form of thin interlayers, lowering the weld metal ductility. Effective modification is ensured by addition of rare-earth elements. Residual content of REM of 0.05–0.12 % is optimum, as uniform distribution of graphite inclusions is ensured, which in this case have only point or globular shape [31]. Weld metal with such a form of graphite is not prone to hot cracking.

Selection of nickel-base electrode materials depends on the strength level of cast iron being welded. Nickel electrodes and wires (up to 98 % Ni) are more suitable for products from comparatively low-strength grey cast irons, particularly, thin-walled. When they are used, the weld metal has sufficient strength (σ_t = = 250–300 MPa) with good values of ductility (δ = = 25–30 %) and hardness (*HB* 160–180), and is readily peened. Electrode materials on nickel-iron base (50–70 % Ni) are more suitable for cast irons of an increased and high strength ($\sigma_t \leq 500$ MPa) and their combinations with steel. In this case weld metal strength on the level of 350–500 MPa is provided at acceptable levels of relative elongation (15–20 %) and hardness (up to *HB* 210 MPa). Such a metal lends itself easily to peening, required to lower the level of residual stresses.

Prevention of porosity in high-nickel welds and in the fusion zone. High gas saturation of cast irons, jump-like lowering of the solubility of hydrogen and other simple gases at metal solidification, running of metallurgical reactions with profuse evolution of carbon oxides and water vapours, short duration of weld pool existence are the factors, promoting disturbance of tightness of weld metal and fusion zone of cast iron welded joints. Their role is considered in detail in [32].

Known is the high susceptibility of nickel-base welds to pore formation [33, 34]. In order to prevent them, it is necessary to weaken the adverse influence of the reaction of nickel oxide reduction by hydrogen with H_2O formation during weld pool solidification. Beneficial metallurgical impact on the molten metal is provided at addition of strong deoxidizers to the weld pool (Figure 8), namely aluminium, titanium, and, particularly, REM, which have a higher affinity to oxygen than the other melt components in the entire range of welding process temperatures [35, 36]. More over, under these conditions oxides of the above elements are not gaseous compounds. Addition of certain amounts of REM to nickel-base electrode wire, allows even eliminating the use of shielding gas, when making open-arc single-pass welds on thin-walled cast iron parts or narrow-gap multipass welds on massive castings [37].

Complex of measures to ensure the quality of joints in arc welding without preheating or postweld heat treatment. High quality of welded joints of structural cast irons is achievable, when the following conditions are satisfied:

• ultimate strength of joints in tensile testing should not be lower than 80 % of the specified minimum ultimate strength of welded cast iron [38]:

• joints made with rigid fastening of elements or directly on the casing part, should be impermeable when tested by kerosene or hydraulic pressure according to the item purpose;

• joint treatment by a cutting tool should not cause any essential difficulties.

In arc welding without high preheating of the item or PWHT, the above complex of conditions is only achievable by using high-nickel electrode materials, performing welding in maximum low modes and not allowing even local fractures in the fusion zone. Solving mainly metallurgical problems, the method of manual welding with high-nickel stick electrodes has exhausted its capabilities for lowering the heat input and reducing the weld metal volumes. As regards the undesirable high level of welding heat input (3.2–3.8 MJ / m), this disadvantage is partially compen-

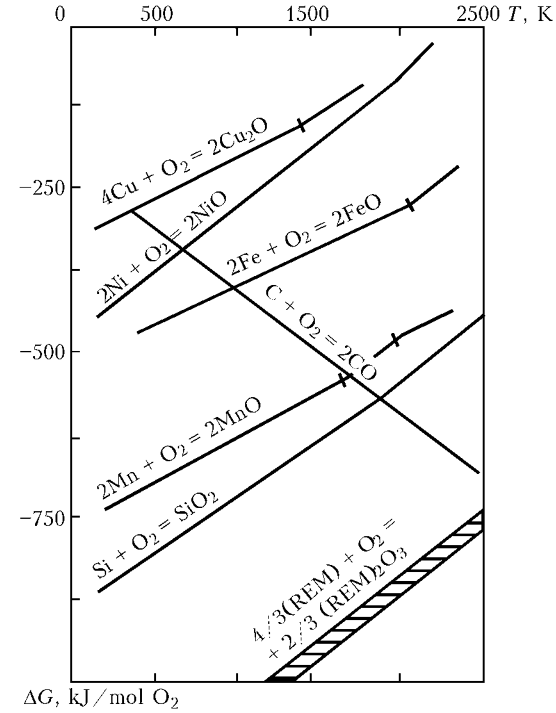

Figure 8. Change of Gibbs energy with temperature for the main elements of weld pool composition in cast iron welding by nickel-based electrode materials

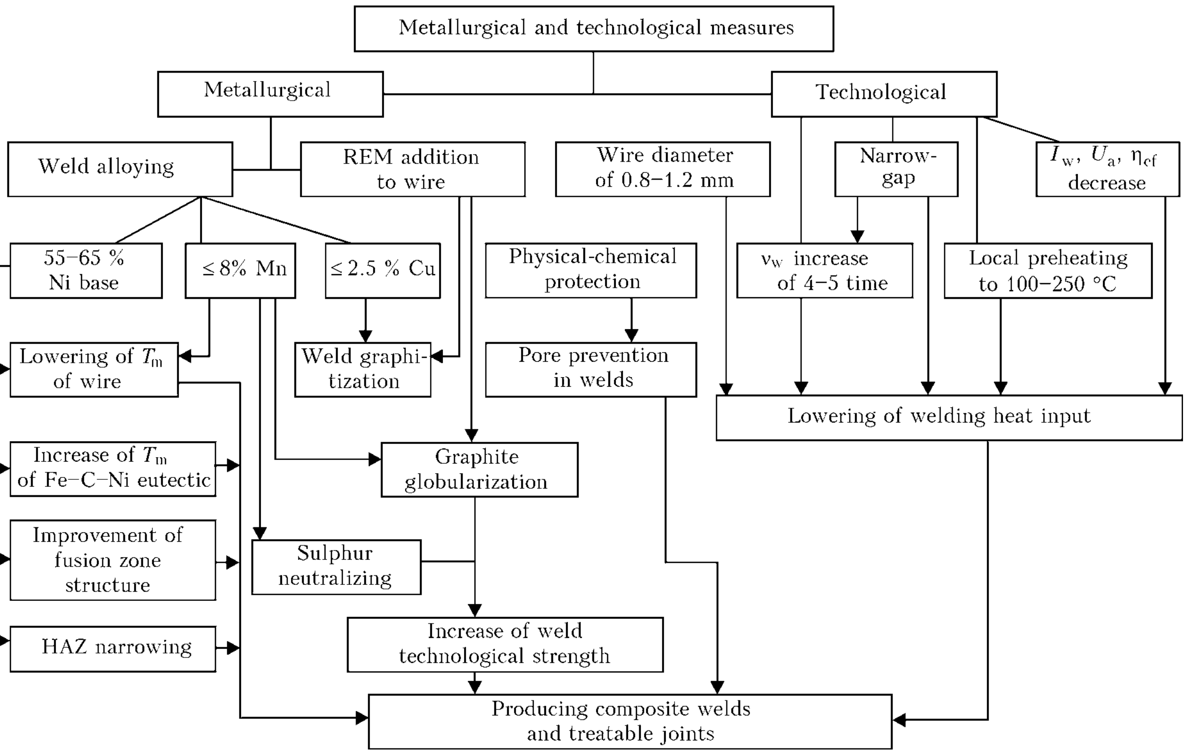

Figure 9. Measures to improve the quality and efficiency of arc welding of cast iron items without high preheating or PWHT, compared to manual welding with coated electrodes based on non-ferrous metals

sated by a special technique of making extended welds, which can be identified with making a multitude of short tack welds with their immediate subsequent peening. As regards a radical lowering (4 to 5 times) of the heat input, advantages of mechanized thin wire welding are obvious.

Generalizing the above main principles, practical recommendations following from them, and gained experience [38–40], a set of measures to satisfy the above complex level of requirements to the joint quality can be presented by a schematic given in Figure 9. Metallurgical measures consist mainly in selection of electrode material composition, technological measures –– in selection of optimum parameters of the welding mode and special preparation of the damaged locations for welding. At present gas-shielded mechanized welding by a high-nickel thin wire or open arc is the arc welding process without preheating or with a low (up to 200 °C) local preheating, largely corresponding to the principles of the above schematic. For this purpose, the E.O. Paton Electric Welding Institute developed a solid wire of PANCh-11 grade, TU 48-21-593–77, from a nickel alloy of a special composition [41, 42]. Proportion of the content of nickel and alloying additives provides lower temperature of electrode wire melting, high weld resistance to hot cracking and sufficient degree of deposited metal graphitization. Addition of an optimum amount of REM to the alloy, guarantees a high arcing stability and allows welding to be performed without using shielding gas. A wide introduction of the process of open-arc mechanized welding of cast iron without preheating or PWHT into industry provided a radical solution of the problem of high-quality repair of casing cast iron parts of machines and mechanisms on a routine scale in all the FSU republics [37, 43–45].

1. Sterenbogen, Yu.A., Khorunov, V.F., Gretsky, Yu.Ya. (1966) *Welding and surfacing of cast iron*. Kiev: Naukova Dumka.
2. Ivanov, B.G., Zhuravitsky, Yu.I., Levchenkov, V.I. (1977) *Welding and cutting of cast iron*. Moscow: Mashinostroenie.
3. Cottrell, C.L.M. (1985) *Welding cast irons*. Cambridge: TWI.
4. (1985) *American Welding Society: welding of cast iron*: Selection of papers. Miami: AWS.
5. *DSTU 3761–98*: Welding and related processes. Pt 1: Weldability. Definitions. Kyiv: Derzhstandart Ukrainy.
6. Bogachev, I.N. (1962) *Metallography of iron*. Sverdlovsk: Metallurgizdat.
7. Girshovich, N.G. (1966) *Crystallization and properties of cast iron in castings*. Moscow-Leningrad: Mashinostroenie.
8. Bunin, K.P., Malinochka, Ya.N., Taran, Yu.N. (1969) *Principles of metallography of cast iron*. Moscow: Metallurgiya.
9. Grabin, V.F., Gretsky, Yu.Ya., Kroshina, G.M. et al. (1987) *Metallography of cast iron welded joints*. Kiev: Naukova Dumka.
10. (1978) *Handbook on cast iron foundry products*. Ed. by N.G. Girshovich. Leningrad: Mashinostroenie.
11. Gretsky, Yu.Ya., Kroshina, G.M., Shekera, V.M. (1980) Mechanical properties of near-weld zone after welding of structural cast irons. *Avtomatich. Svarka*, **1**, 71–72.
12. Elistratov, P.S. (1959) *Welding properties of cast iron*. Moscow: Mashgiz.
13. Levi, L.I., Aleksandrova, A.N. (1970) Susceptibility of cast irons to hydrogen absorption and evolution. In: *Principles of formation of casting alloys:* Proc. of 14th Meet. on Theory of Foundry Processes. Moscow: Nauka.
14. Gretsky, Yu.Ya. (1980) Joint formation in arc welding of structural cast irons. Pt 1: Role of graphite phase of base metal. *Avtomatich. Svarka*, **6**, 1–4.
15. Gretsky, Yu.Ya. (1980) Joint formation in arc welding of structural cast irons. Pt 2: Conditions of sound fusion. *Ibid.*, **8**, 27–29.
16. Gretsky, Yu.Ya., Demchenko, V.F. (1986) Interaction of weld pool metal with graphite near the fusion line in arc welding of cast irons. *Ibid.*, **5**, 30–32.
17. Gretsky, Yu.Ya., Sterenbogen, Yu.A. (1967) Weldability of cast iron after high-temperature gas corrosion. *Ibid.*, **9**, 35–38.
18. Volsky, A.N., Sergievskaya, E.M. (1968) *Theory of metallurgical processes*. Moscow: Metallurgiya.
19. Petrov, G.L. (1972) *Welding consumables*. Leningrad: Mashinostroenie.
20. Nikitin, V.M. (1973) Specifics of metal solidification in fusion welding of dissimilar metals. *Svarochn. Proizvodstvo*, **5**, 53–54.
21. Makarov, E.L. (1981) *Cold cracks in welding of alloy steels*. Moscow: Mashinostroenie.
22. Gretsky, Yu.Ya. (1980) Influence of weld pool composition on conditions of metal solidification near the fusion line in arc welding of cast iron. *Avtomatich. Svarka*, **12**, 18–23.
23. Elliot, D.F., Gleyser, M., Ramakrishna, V. (1969) *Thermochemistry of steelmaking processes*. Moscow: Metallurgiya.
24. Gretsky, Yu.Ya., Vasiliev, V.G., Kroshina, G.M. (1979) Formation of near-weld zone structure in welding of grey pearlite cast iron. *Avtomatich. Svarka*, **12**, 22–25.
25. Gretsky, Yu.Ya., Kroshina, G.M., Vasiliev, V.G. (1981) Effect of arc welding thermal cycle on structure and mechanical properties of high-strength cast irons. *Ibid.*, **6**, 9–12.
26. Gretsky, Yu.Ya., Kroshina, G.M., Vasiliev, V.G. et al. (1988) Effect of welding thermal cycle on structure and mechanical properties of low-alloy high-strength ferritic cast iron. *Ibid.*, **8**, 6–8, 18.
27. Gretsky, Yu.Ya., Novikova, D.P., Kroshina, G.M. (1986) Strength and plasticity of pearlite cast irons at temperatures inherent to HAZ in welding. *Ibid.*, **3**, 15–17, 20.
28. Gretsky, Yu.Ya. (1981) Mechanism of crack formation in fusion zone in welding of cast iron to steel and iron-nickel alloys. *Ibid.*, **4**, 19–22.
29. Gretsky, Yu.Ya., Novikova, D.P., Kroshina, G.M. (1986) Effect of thermal cycle on cracking resistance of cast irons in welding without preheating. *Ibid.*, **4**, 1–4, 13.
30. Gretsky, Yu.Ya., Tikhonovskaya, L.D. (1979) Selection of optimal nickel content in cast iron welds. *Ibid.*, **7**, 35–38.
31. Gretsky, Yu.Ya., Tikhonovskaya, L.D. (1980) Modification of high-carbon iron-nickel weld metal in cast iron welded joints. *Ibid.*, **3**, 16–18.
32. Gretsky, Yu.Ya., Borisov, A.I. (1991) Metallurgical peculiarities of arc welding of structural cast irons. *Ibid.*, **5**, 7–13.
33. Medovar, B.I., Latash, Yu.V. (1974) Effect of hydrogen and oxygen on pore formation in welding of stable-austenite steels and nickel. *Ibid.*, **10**, 5–6.
34. Bagryansky, K.V., Kuzmin, G.S. (1963) *Welding of nickel and its alloys*. Moscow: Mashgiz.
35. Averin, V.V., Lopukhov, G.A. (1981) Directions of investigations in metallurgy. In: *Results in science and engineering*. Theory of Metallurgical Processes Series. Vol. 4. Moscow: VINITI.
36. Darken, L.S., Gurri, R.V. (1960) *Physical chemistry of metals*. Moscow: Metallurgizdat.
37. Gretsky, Yu.Ya. (1976) Mechanised welding of cast iron with self-shielded wire PANCh-11 without preheating. *Svarochn. Proizvodstvo*, **11**, 12–13.
38. (1989) *Guide for welding iron castings*: American National Standard ANSI / AWS D11.2.89. Miami: AWS.
39. Asnis, A.E., Gretsky, Yu.Ya. (1978) State-of-the-art and prospects of welding of cast iron. *Avtomatich. Svarka*, **8**, 39–42.
40. Gretsky, Yu.Ya. (1978) Initial postulates for development of high-efficient arc welding technology of cast iron without preheating. *Ibid.*, **11**, 41–45.
41. Asnis, A.E., Gretsky, Yu.Ya., Kuznetsov, E.P. et al. *Welding wire*. USSR author's cert. 492394. Publ. 1975; Pat. 390253 USA. Publ. 30.09.75; Pat. 742635 France. Publ. 18.12.75; Pat 2434122 FRG. Publ. 12.04.76; Pat. 893724 Japan. Publ. 27.08.77.
42. Asnis, A.E., Gretsky, Yu.Ya., Melnichenko, I.M. (1976) Self-shielded wire PANCh-11 for mechanised welding of cast iron. *Avtomatich. Svarka*, **2**, 69.
43. Gretsky, Yu.Ya., Demchenko, Yu.V. (1998) Recovery of cast iron base parts of motors with wire PANCh-11. *Svarshchik*, **4**, 11.
44. Gretsky, Yu.Ya., Demchenko, Yu.V. (2000) Recovery of cast iron parts of motors by mechanised welding with PANCh-11 wire. *Tyazh. Mashinostroenie*, **2**, 23–24.
45. Gretsky, Yu.Ya. (2005) Current possibilities in high-quality recovery by welding of foundry cast iron and steel parts of railway transport. *Zalizn. Transport Ukrainy*, **3**, 285–288.

EFFECT OF THE DEGREE OF ALLOYING OF HEAT-RESISTANT CHROMIUM STEELS ON HARDNESS OF METAL WITHIN THE WELDED JOINT ZONE

V.Yu. SKULSKY
E.O. Paton Electric Welding Institute, NASU, Kiev, Ukraine

Considered is relationship between the degree of alloying of heat-resistant chromium steels (with 2.25--13 % Cr), martensite transformation temperature M_s and resultant hardness of the hardened metal of welded joints. It is shown that the level of hardness depends upon temperature M_s, and is related to the time of self-tempering of martensite at the stage of metal cooling from the transformation temperature.

Keywords: arc welding, heat-resistant steels, welded joints, alloying, martensite, self-tempering, hardness

One of the main causes of cold cracking is formation of hardened structures in the HAZ metal. Increase in the total content of alloying elements in steel welded causes increase in its sensitivity to cracking. This feature is basic to evaluation of weldability from the value of carbon equivalent C_{eq} or Ito--Bessyo parameter P_{cm} [1, 2]. Hardness of the HAZ metal can also be used as an approximate indicator of sensitivity to cracking (it is thought that the risk of cold cracking is run at hardness over *HV* 350--400 [2, 3]). When comparing performance of modern high-chromium heat-resistant steels, it is sometimes noted that steels with 12 % Cr are more sensitive to cold cracking than steels with 9 % Cr, as martensite transformation of the former occurs at a lower temperature, this resulting in a higher hardness of metal (*HV* 650, compared with *HV* 450 of steels with 9 % Cr) [3, 4]. At a low chromium content, austenite transformation is shifted towards a higher temperature, which is accompanied by development of sensitivity to the intermediate transformation, resulting in a relatively low hardness of metal. These peculiarities are reflected in TTT diagrams plotted for specific steels. Because of scattering of such data, there is no definite opinion of a general character of the effect of alloying on behaviour of steels under conditions of decomposition of overheated austenite.

This study considers the effect of the degree of alloying of heat-resistant chromium steels on temperatures of beginning of austenite decomposition and approximate hardness of metal with a hardened structure. Analysis was conducted using the data on the character of austenite transformation in steels with a chromium content of 2.25 to 13 % [3, 5--9]. Compositions of steels are given in the Table.

Generalised evaluation of the degree of alloying was made by an approach based on methods for approximate determination of phase compositions of steels, using the known Schaeffler or DeLong diagrams, from the calculated values of Cr_{eq} and Ni_{eq}, as these parameters allow for the effect of elements that exert the main impact on structure formation. In this case, the degree of alloying with «reactive» structure-determining elements was expressed in terms of generalising parameter $P_C = Cr_{eq} + Ni_{eq}$, where

Chemical composition of analysed steels

Type, grade of steel	Content of elements, wt.%											
	C	Si	Mn	P	S	Cr	Ni	Mo	V	W	Nb	N	Others
2.25Cr–1Mo [5]	0.10	0.34	0.48	0.017	0.013	2.16		0.96					
7CrMoVTiB10-10 [3]	0.081	0.21	0.53	0.004	0.004	2.44	0.18	0.95	0.26		0.002	0.007	0.04 Al 0.004 B 0.053 Ti
3Cr–1Mo [5]	0.10	0.40	0.40			3.00		1.00					
3Cr–1.5Mo [5]	0.10	0.40	0.40			3.00		1.50					
P91 [6]	0.10	0.34	0.47	0.018	0.003	8.52	0.28	0.93	0.20		0.072	0.060	0.011 Al
E911 [3]	0.115	0.20	0.51	0.017	0.002	8.85	0.24	0.94	0.22	0.95	0.069	0.084	0.007 Al
HCM12A [7]	0.13	0.31	0.50	0.014	0.001	10.65	0.35	0.35	0.22	1.92	0.060	0.061	0.009 Al
X20CrMoV121 [8]	0.18	0.28	0.54	0.020	0.005	12.70	0.63	0.90	0.32			0.030	
20X13 [9]	0.24	0.37	0.27			13.32	0.32	0.06					

© V.Yu. SKULSKY, 2006

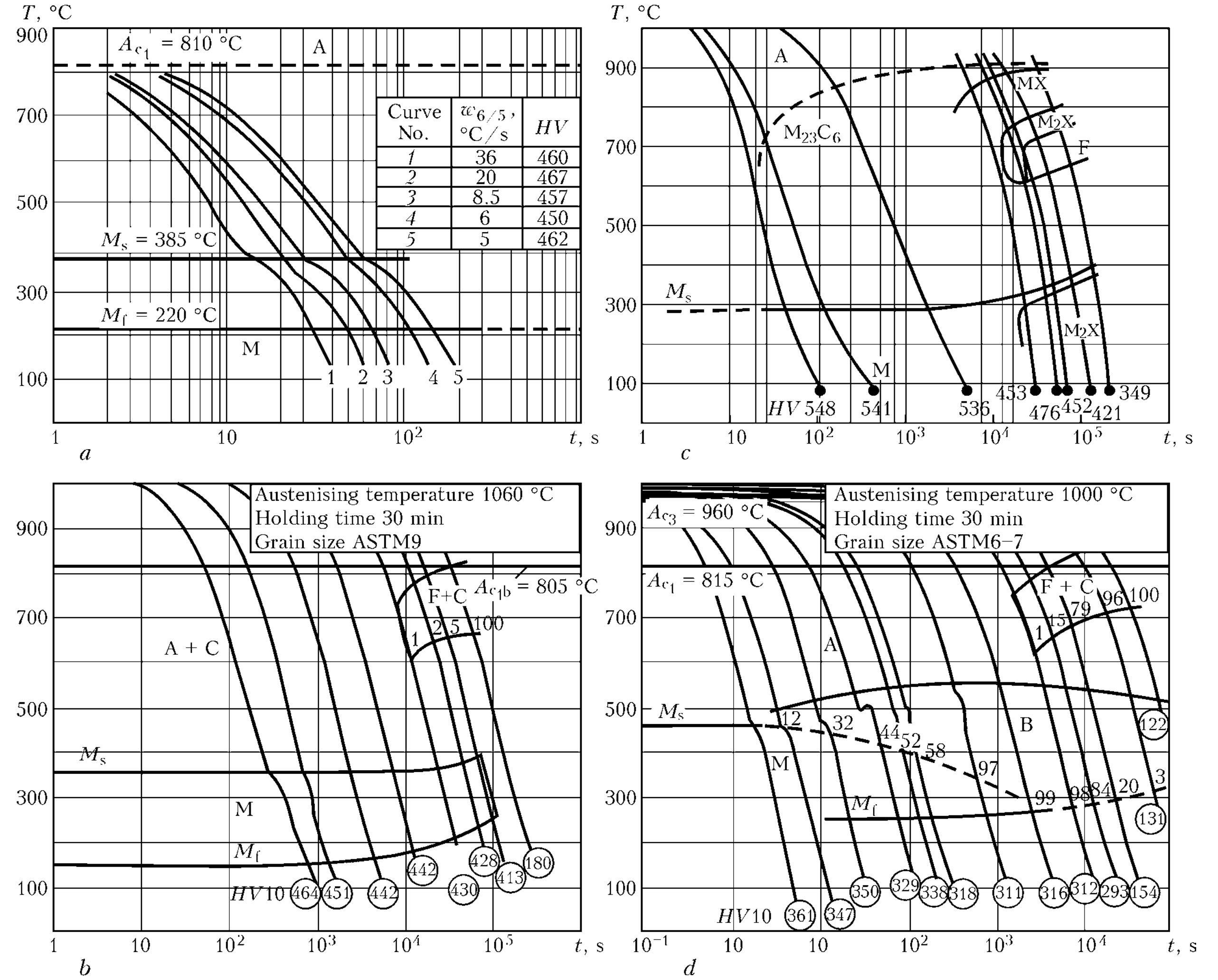

Figure 1. TTT diagrams for heat-resistant steels with different chromium content: *a* — steel P91 [6]; *b* — E911 [3]; *c* — X20CrMoV121 [8]; *d* — steel with 2.25 % Cr (7CrMoVTiB10-10) [3]: A — austenite; F — ferrite; M — martensite; M_s and M_f — beginning and end of martensite transformation

$$(\mathrm{Cr_{eq}} = \%\ \mathrm{Cr} + \%\ \mathrm{Mo} + 1.5\ \%\ \mathrm{Si} + 0.5\%\ \mathrm{Nb} + {}$$
$$+ \{2\cdot(\%\ \mathrm{Ti} + \%\ \mathrm{Al}) + \%\ \mathrm{W}\},$$
$$\mathrm{Ni_{eq}} = \%\ \mathrm{Ni} + 30(\%\ \mathrm{C} + \%\ \mathrm{N}) + 0.5\ \%\ \mathrm{Mn} + \{12\ \%\ \mathrm{B}\}).$$

Elements with coefficients taken from the data of [10] are additionally given in braces.

Heat-resistant steels with increased chromium content (9–12 %) feature a high stability of austenite under overcooling conditions, which leads to formation of martensite at different cooling rates in quiet air. In diagrams, this is shown by the presence of a wide time range of existence of purely martensite transformation (Figure 1). For example, in steel P91 with 9 % Cr [4], the diffusion decomposition of austenite to form pearlite may initiate in dwelling at the stage of cooling within a range of 800--500 °C for 30,000--40,000 s (8.3–11 h), which corresponds to cooling rate $w_{8/5}$ of about 0.01--0.008 °C / s, and is characteristic of air cooling of a pipe with 80 mm wall thickness. In practice, the cooling rates in welding are much higher. Depending upon the method (arc power), heat parameters of welding and metal thickness, the real cooling rates may vary approximately from 10 to 30 °C / s or higher (the latter is more characteristic of making the first root passes in thick-walled butt joints with a decreased temperature of preheating, or without preheating), i.e. formation of a purely martensitic structure in the HAZ metal might be expected under conditions of welding steels with 9 % Cr. As because of the requirement for providing welded joints with homogeneous physical-mechanical properties the welds should have alloying similar to that of the base metal, the entire welded joints experience hardening to form martensite.

In a general case, beginning of martensite transformation depends upon the degree of hardening of the crystalline lattice of austenite with carbon and interstitial alloying elements, which cause increase in resistance of the crystalline system to shear re-arrangement of position of atoms by inducing internal distortions and fields of elastic stresses. As a result, martensite transformation in steels with an increased content of alloying elements occurs under conditions of accumulation of shrinkage stresses at a lower temperature than in steels with a lower degree of alloying. Thus, in steels with 12 % Cr, compared with steels with 9 % Cr (Figure 1, *c*), point M_s is located approximately 100 °C lower, i.e. at a level of 280 °C (553 K)

[8]. In steels with a low chromium content (of the type of 2.25 % Cr--1 Mo) (Figure 1, *d*), martensite transformation occurs at a higher temperature, i.e. approximately at 460 °C (733 K). Diffusion processes develop rather quickly at these temperatures, and the intermediate bainite transformation takes place in slowing down of cooling [3].

Results of analysis of the effect of the degree of alloying of chromium steels on the beginning of martensite transformation, M_s, are shown in Figure 2. Temperatures M_s were determined from the TTT diagrams [3, 5--9] and by the calculations using the following relationship [11]:

$$M_s\ (°C) = 539 - 423\ (\%\ C) - 30.4\ (\%\ Mn) - 12.1\ (\%\ Cr) - 17.7\ (\%\ Ni) - 7.5\ (\%\ Mo).$$

It should be noted that other models are also available for estimation of the values of M_s. An additional allowance can also be made for the upward displacement of point M_s, depending upon the content of carbide-forming elements or carbon, which may amount to several dozens of degrees at its low contents (e.g. using parameter «4.2 / C», as is done in one of the models). The model selected yields good agreement of the results of calculations and practical measurements, although there are marked discrepancies in some cases. Moreover, this study is aimed not at achieving the maximal possible accuracy of estimation of the M_s values only by calculations, but at tracing the tendency of variations in temperatures of beginning of phase transformations in steels with a different alloying degree, as well as relationship between the M_s values and hardness of the hardened metal using a combination of experimental and calculation data.

As a whole, the calculation values and experimental results reflect a general principle of decrease in the martensite transformation point with increase in the degree of alloying of chromium steels. Increase in the chromium content from 2.5–3 to 12 % causes a substantial change in values of M_s. The martensite transformation temperatures for steels with 9 and 12 % Cr also exhibit a marked difference. The M_s temperatures for steels with 9 % Cr take approximately an intermediate position between the M_s temperatures for steels with 2.5 and 12 % Cr. This difference in the martensite transformation temperatures correlates with a resulting hardness of the hardened structure.

The levels of hardness of metal after decomposition of austenite show a pronounced difference, corresponding to the degree of its alloying with chromium (Figure 3). Conditionally, steels can be subdivided into three categories in the level of hardness: ~*HV* 550 (steels with 12 % Cr), ~*HV* 450 (9 % Cr), and ~*HV* 350 (2--3 % Cr). The higher the martensite transformation point, the longer the time of dwelling of metal with the hardened structure at increased temperatures, which creates conditions for achieving a higher degree of self-tempering of martensite. A resulting hardness of martensite tempered in cooling becomes lower, which must have a favourable effect on cold crack resistance.

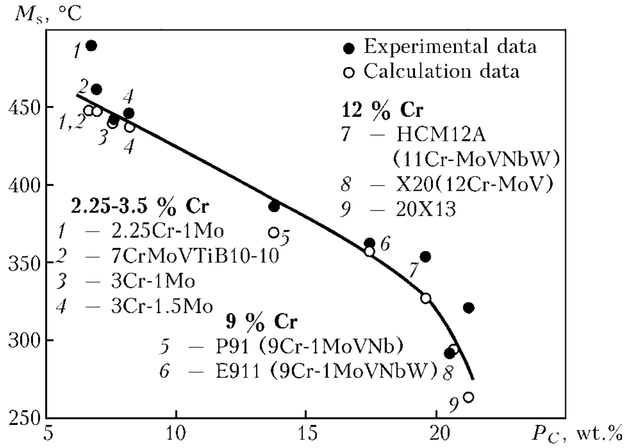

Figure 2. Effect of the degree of alloying of chromium steels, P_C, on temperature of beginning of martensite transformation, M_s

In steels with a purely martensite transformation (9–12 % Cr), a change in the cooling rate hardly changes the metal hardness, which remains high. A more significant decrease in hardness takes place only within a range of very low cooling rates ($w_{6/5}$ < < 0.5--0.2 °C / s), where conditions are created for partial decomposition of austenite by the equilibrium (diffusion) mechanism (Figure 3, *b*). However, such low rates are never achieved in fusion welding. In reality, some decrease in hardness of the HAZ metal

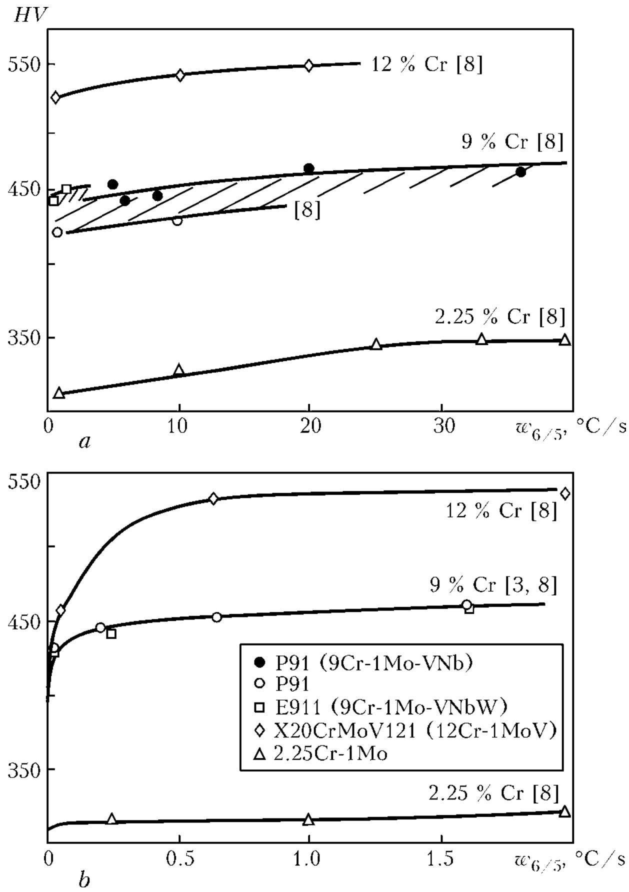

Figure 3. Effect of increased (*a*) and decreased (*b*) cooling rates $w_{6/5}$ on hardness of the HAZ metal in heat-resistant steels of different alloying (dark points — PWI results)

may take place as a result of self-tempering of martensite provided by special measures taken to slow down cooling of the welded joints.

Austenite does not have such stability in overcooling in steels with a low alloying degree (2.5 % Cr) as in high-chromium steels. As a result of decomposition at the highest (for materials under consideration) temperature (about 460 °C), the intensive diffusion of carbon hampers formation of pure martensite, and the bainite transformation develops more intensively. Subsequent self-tempering of the hardened structure provides metal with a resulting low hardness. At $w_{6/5} < 16$ °C / s, the hardness decreases more dramatically because of transition from mostly martensite to bainite transformation.

Therefore, the results obtained show that metal of the welded joints in steels with 9--12 % Cr experiences hardening to form martensite at any cooling rate during the welding process. The higher the content of alloying elements in steel, the higher the hardness of this metal, as increase in the degree of alloying is accompanied by decrease in the temperature of beginning of martensite transformation, and the process of self-tempering of martensite is restrained with further cooling. In welding with slow cooling, providing that the self-tempering process takes place, it is possible to achieve some decrease in hardness of the HAZ and weld metals. However, with conventional heat parameters of welding no substantial decrease in hardness normally takes place. Therefore, to ensure cold crack resistance of the welded joints it is necessary to additionally restrict the effect of other harmful factors, i.e. decrease the level of hydrogen, and avoid formation of stress raisers.

1. Petrov, G.L., Tumarev, A.S. (1977) *Theory of welding processes*. Moscow: Vysshaya Shkola.
2. Hrivnyak, I. (1984) *Weldability of steels*. Moscow: Mashinostroenie.
3. Bendick, W., Haarmann, K., Rigg, M. et al. (1996) Current state of development of advanced pipe and tube materials in Germany and Europe for power plant components. In: *Lectures of VGB Conf*. (Cottbus, Oct. 8–9, 1996). Mannesmann Rohr.
4. Zschau, M., Niederhoff, K. (1994) Construction of piping systems in the new steel P91 including hot induction bends. *VGB Kraftwerkstechnik*, 74(**2**), 142–149.
5. Lundin, C.D., Khan, K.K. (1996) Fundamental studies of the metallurgical causes and mitigation of reheat cracking in 11 / 4 Cr--1 / 2 Mo and 21 / 4 Cr--1 Mo steels. *WRC Bulletin*, **409**, 117.
6. Skulsky, V.Yu., Tsaryuk, A.K., Vakhnin, Yu.N. et al. (2003) Applications and properties of new 9 % Cr heat-resistant steel. In: *Proc. of Int. Conf. on Current Problems in Welding and Life of Structures* (Kiev, Nov. 24–27, 2003). Kiev: PWI.
7. Zeman, M., Brozda, J., Pasternak, J. (1999) Ocena spawalnosci stali HCM12A przeznazcenej na elementy kotlow energetycznych pracujace przy parametrach nadkrytycznych. *Przeglad Spawalnictwa*, LXXI(**6**), 1--7.
8. Gnirb, G. (1994) Present situation of the use of P91 (X10CrMoVNb91) in German power stations. *IIW Doc. XI-617–94*.
9. Popov, A.A., Popova, L.E. (1984) *CCT and TTT diagrams of overcooled austenite decomposition*. Moscow: Metallurgiya.
10. Grabin, V.F. (1982) *Metals science of fusion welding*. Kiev: Naukova Dumka.
11. Akselsen, O.M., Rorvik, G., Kvaale, P.E. et al. (2004) Microstructure-property relationships in HAZ of new 13 % Cr martensitic stainless steels. *Welding J*., 83(**5**), 160--167.

RESIDUAL STRESSES IN BUTT JOINTS OF THIN SHEETS FROM ALLOY AMg6 AFTER ARC AND LASER-ARC WELDING

V.A. SHONIN, V.S. MASHIN, V.Yu. KHASKIN and **T.N. NEDEJ**
E.O. Paton Electric Welding Institute, NASU, Kiev, Ukraine

Results of experimental study of residual strains and stresses in butt joints of thin sheets from alloy AMg6 having thickness 1.9 mm made by MIG and MIG + laser welding are reported. It is established that a six-fold increase of the welding speed (hybrid process) provides a two-fold narrowing of the weld cross-section, one-and-a-half times narrowing of the HAZ with longitudinal residual stresses, and more than four-fold reduction of the transverse residual stresses.

Keywords: aluminium alloys, fusion welding, butt joints, thin-sheet structures, near-weld zone, residual strains, residual stresses

During welding of sheet structures, in the weld metal and near-weld zone takes place an inevitable accumulation of thermoplastic strains which causes formation of longitudinal and transverse residual strains and stresses [1]. It is known that transverse tensile residual stresses in the fields of stress raisers due to the weld convexity reduce fatigue resistance of joints at transverse action of variable stresses from external loading [2]. These residual stresses are balanced over the longitudinal section of the butt joint, and depend on the dimensions of the joined elements, welding speed and length of the weld. Besides, at welding thin-sheet elements residual strains and stresses cause loss of stability at compression of the base metal owing to the influence of shrinkage forces in the weld and HAZ. Arising residual bending strains are the reason of significant non-uniformity of distribution of residual stresses throughout the thickness of metal and the increased residual stress level in surface layers of near-weld zone. In this connection at manufacturing welded sheet structures due attention should be given to the reduction of transverse tensile residual stresses in joints.

© V.A. SHONIN, V.S. MASHIN, V.Yu. KHASKIN and T.N. NEDEJ, 2006

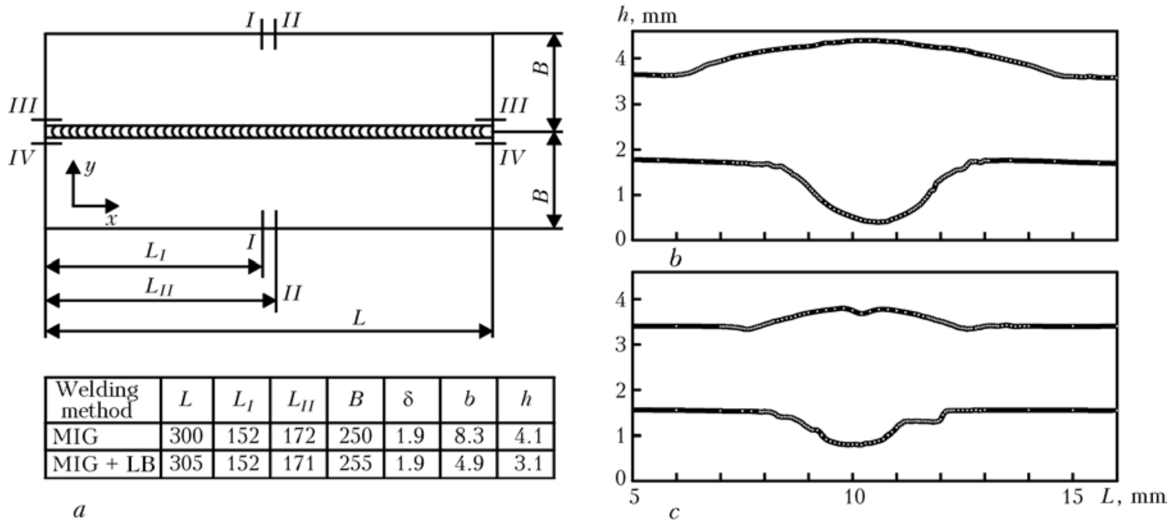

Welding method	L	L_I	L_{II}	B	δ	b	h
MIG	300	152	172	250	1.9	8.3	4.1
MIG + LB	305	152	171	255	1.9	4.9	3.1

Figure 1. Diagram of sample of butt joints of alloy AMg6 (*a*) and contours of welds performed by MIG (*b*) and MIG + LB (*c*) welding: L — length of sample; L_I, L_{II} — distances from beginning of weld up to gauge installation site; B — widths of welded plates; δ — thickness of base metal; b — width of weld at its top side; h — height of weld (all dimensions are in millimeters); *I–IV* — sections

One of the efficient ways of decreasing residual strains and stresses arising in thin-walled structures is application of highly efficient welding processes providing minimal heat input. In this context merit attention hybrid methods of welding which have gained wide acceptance in recent years [3–5]. These are based on localization of thermal energy in the fusion zone that allows considerably increasing the speed of welding and penetration depth while reducing heat input into the base metal. The most perspective for joining thin-sheet aluminum alloys is the way of welding with a consumable electrode (MIG) with application of a laser beam (LB) which can provide higher welding speed at low energy input and, as a consequence, reduction of transverse residual strains and stresses. However data about influence of welding speed on the level of residual stresses and strains for thin-sheet aluminum structures are unavailable as yet.

The purpose of the present work is to establish levels and pattern of distribution of residual strains and stresses in butt joints of thin-sheet aluminum alloy AMg6, obtained by hybrid MIG + LB and traditional MIG methods of welding.

Research procedure. The research was carried out on samples of butt joints of two plates 300 × (125 + + 125) × 1.9 mm from alloy AMg6, butt-welded in one pass. Length and width of plates were chosen with the intention of obtaining the highest possible residual stresses. In doing so the principle of similarity to heavy-thickness large-sized samples, in which maximal residual stresses arise, was accepted. With this in mind, their lengths and widths were reduced in proportion to the reduction of metal thickness.

Specimens were welded in the downhand position on a forming backing from stainless steel, using filler wire AMg6 having diameter 1.2 mm. Specimens in welding were fastened in rigid fixtures. For MIG welding standard unit «Fronius TPS-2700» and commercial CO_2-laser LT-104 were applied. The shielding gas was argon. MIG welding was carried out using the following mode: welding current I_w = 90 À; arc voltage U_a = 17.8 V; welding speed v_w = 50 m / h; wire feed rate v_f = 5.9 m / min. Welding by hybrid technique was carried out at 2.5 kW laser net power with the following MIG welding conditions: I_w = = 185 À; U_a = 23.3 V; v_w = 300 m / h; v_f = = 11.8 m / min. Figure 1 shows overall dimensions of butt joints and weld contours constructed using profilometry data.

For experimental determination of residual strains in the near-weld zone, a destructive method of strain estimation based on measurement of elastic deformations in a specific spot of the investigated welded joint metal at its full relieving [6] was used. The method in question features high accuracy and allows determining residual strains both on the surface of the butt joint, and that averaged throughout the sample thickness. Relieving was effected by mechanical cutting out a section of metal with tensile resistance gauges at its top and bottom surfaces. For this purpose from each lot of the welded specimens one reference sample was taken, on which measurements of residual strains and stresses were carried out.

Magnitudes of residual strains were defined on the top and bottom surfaces of the butt joints in the directions parallel to the weld axis (sections *I–I* and *III–III*) and normal to the weld (*II–II* and *IV–IV*) (see Figure 1). Longitudinal sections *I–I* and *II–II* passed lengthways of HAZ at 5–7 mm from the weld axis, while lateral *III–III*, *IV–IV* at 152 and 172 mm from the weld beginning. Resistance strain gauges (wire types PKB and PKP and foil type KF) were attached using a cyanacrylate adhesive. For sections *I–I* were used PKB gauges with mounting base of 20 mm; for *II–II*, PKP with 10 mm base; for *III–III*, KF with 10 mm base; and for *IV–IV*, PKB and PKP with 5 mm base. The arrangement of gauges corresponded to the assumed directions of the two stress components oriented lengthways $\sigma_{res(x)}$ (sections *I–I*

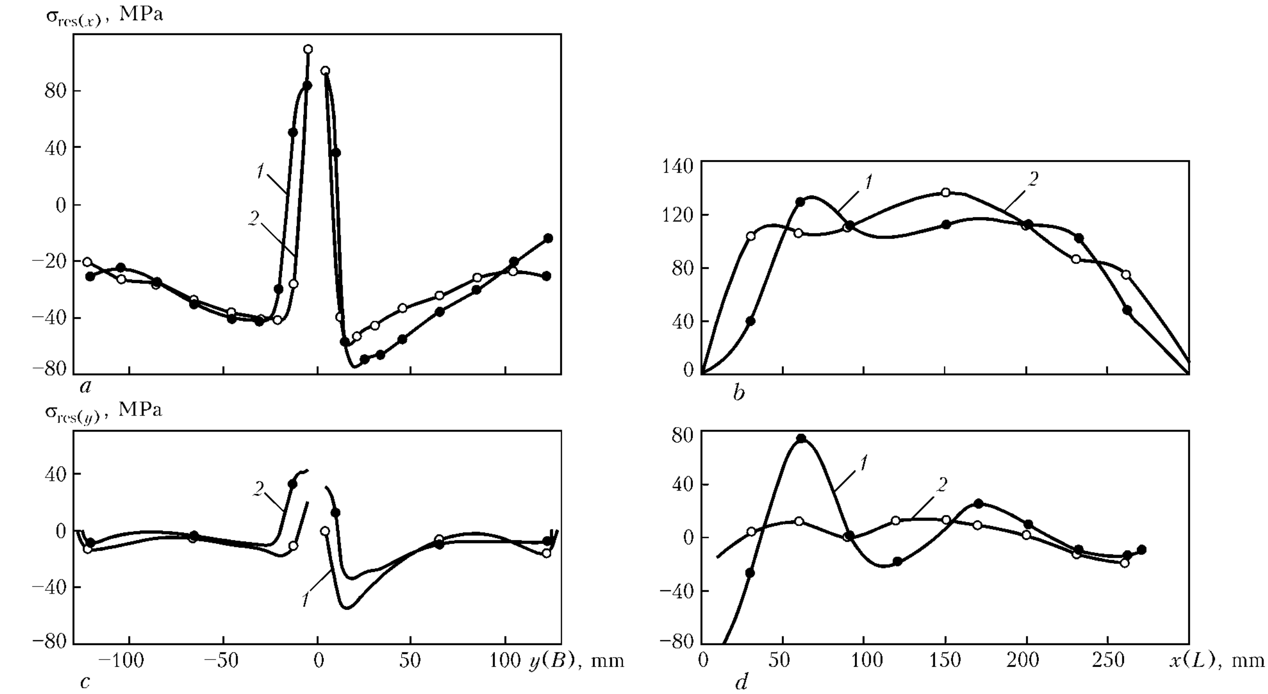

Figure 2. Average values of residual stresses of longitudinal component (*a*, *b*) in transverse *I--I* and longitudinal *III–III* sections, and transverse component (*c*, *d*) in transverse *II--II* and longitudinal *IV--IV* sections, respectively: *1* — MIG welding; *2* — MIG + LB welding

and *III–III*) and across $\sigma_{res(y)}$ (*II--II* and *IV--IV*) the welds. On each sample up to 80 strain gauges were used.

Measurements of strains were conducted using device ISD-3. Temperature compensation was implemented by using same-type gauges bonded to the relieved plates from the mentioned alloy. Strain gauges from each type lot, used for compression and tension monitoring of the surface layers of metal at pure bending, were checked on a calibration device using a $400 \times 30 \times 10$ mm reference bar from alloy AMg6. The measurement error for strains, in comparison with calculated, did not exceed ±4 %.

After measurement of initial gauge resistance, relieving of the metal was begun starting from the field of active tensile residual stresses. With this purpose first were drilled holes 10 mm in diameter in the weld metal all along its length at 30–50 mm intervals, which has enabled to considerably lower the levels of active tensile residual stresses. Then in succession were cut out sections of the plate with gauges. The measured resistances of gauges before and after relieving in the form of $\varepsilon = \Delta_{RSU} \cdot 10^{-5}$ (here RSU are the relative strain units), were represented by the approximating linear graphs plotted for various sections and orientations of residual strains with their readout starting from the middle (sections *I--I* and *II–II*) and the beginning (*III–III* and *IV–IV*) of the weld. Using these graphs were corrected experimental data on longitudinal and transversal strains at conditional overlapping of gauges location coordinates.

Calculations of biaxial surface residual stresses were made using the values of residual strains obtained experimentally, applying the known formulas of the elasticity theory [6]:

$$\sigma_x = \frac{E}{1 - \mu^2} (\varepsilon_x + \mu\varepsilon_y); \quad \sigma_y = \frac{E}{2 - \mu^2} (\varepsilon_y + \mu\varepsilon_x),$$

where σ_x and σ_y are the longitudinal and transverse stresses; $E = 69000$ MPa is the modulus of elasticity; ε_x and ε_y are the longitudinal and transverse relative strains, respectively; $\mu = 0.33$ is the Poisson's ratio.

The averaged across the thickness longitudinal and transverse residual stresses were defined from the expression

$$\sigma_{res} = \frac{\sigma_{res}^{t} + \sigma_{res}^{b}}{2},$$

where σ_{res}^{t} are the stresses on the top (front side) surface of the joint; σ_{res}^{b} is the same on its bottom (backside) surface. The curves describing distribution of longitudinal and transverse residual stresses in considered sections of the joints are shown in Figure 2. Non-uniformity of distribution of residual stresses throughout the thickness of the metal caused by residual bending is represented (Figure 3) by the difference between values of residual stresses on the top and bottom surfaces of the joint:

$$\sigma_{bend} = \frac{\sigma_{res}^{t} - \sigma_{res}^{b}}{2}.$$

Results of measurements using strain gauges are designated by points on the curves demonstrating distribution of residual stresses.

Results of research and discussion. The values of longitudinal residual stresses averaged throughout the thickness, $\sigma_{res(x)}$, in transverse section *I–I* of the central parts of welded samples conform to the known [2] pattern of distribution. They are balanced in re-

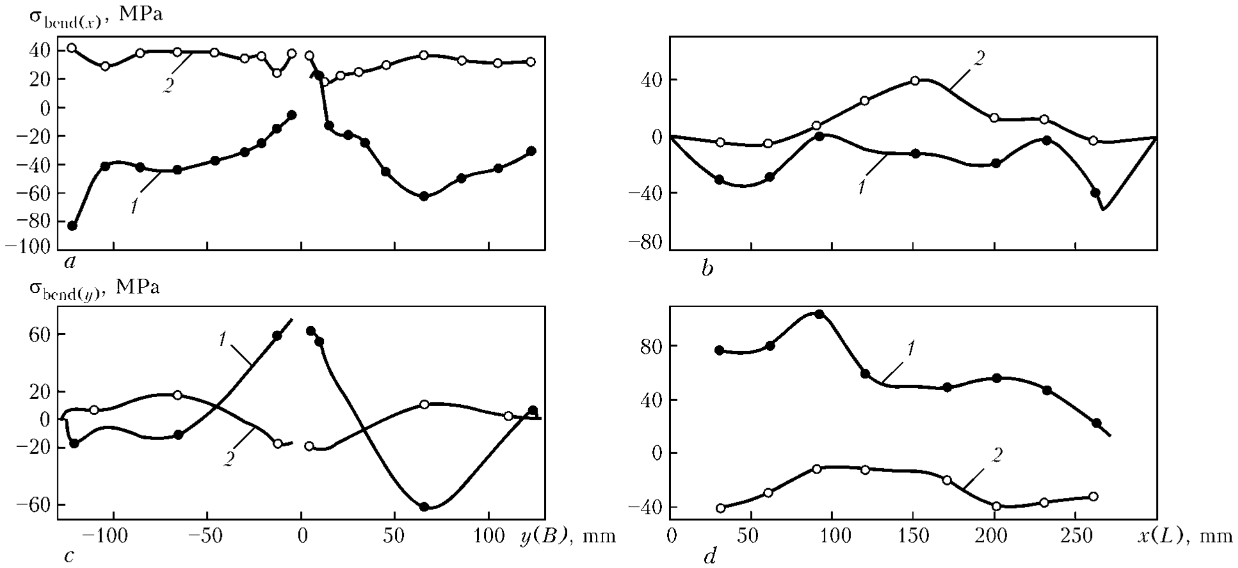

Figure 3. Bending stresses on top surface of samples in longitudinal direction on axis õ (*a, b*) for sections *I--I* and *III--III* respectively, and in transverse direction along axis *y* (*c, d*) for sections *II–II* and *IV--IV*, respectively (for *1, 2* see Figure 2)

spect of the resulting forces and moments in the planes of their action (see Figure 2, *a*). As it follows from Figure 2, *a* and *c*, the width of the near-weld zone with active tensile residual stresses at the hybrid method of welding is 1.5 times smaller than in butt joints performed by MIG welding. In section *III–III* values of longitudinal tensile stresses $\sigma_{res(x)}$ reach their maximum in the central part of the sample and decrease to zero in the beginning and the end of the joints (Figure 2, *b*). In the case of MIG + LB welding the maximal values of longitudinal tensile residual stresses in the middle of the sample slightly exceed $\sigma_{res(x)}$ for MIG welding.

The transverse residual stresses averaged throughout the thickness, $\sigma_{res(y)}$, along the section *IV–IV* show wave distribution pattern (see Figure 2, *d*). In the first wave propagating in the initial section of the weld about 110 mm long, the maximal values of stresses $\sigma_{res(y)}$ reach ±80 MPa in MIG welding but do not exceed ±20 MPa in MIG + LB welding. Pattern of distribution of transverse residual stresses $\sigma_{res(y)}$ along the weld essentially differs from that widely described in the literature, for example in [7], in that residual stresses in welding get balanced already in the initial section of the joint 100–120 mm long. Further formation of transverse residual stresses is distinguished by low peak values. They are locally balanced and reach their maximal values only near the weld (Figure 2, *c*, *d*).

In MIG welding the peak values of $\sigma_{res(y)}$ in the following the first waves of transverse residual stresses subside, to ±30 MPa, which is obviously caused by leveling of temperature gradient along the joint. In hybrid welding method transverse residual stresses $\sigma_{res(y)}$ do not reach their peak values owing to six-fold increase of the welding speed and 1.5 times reduction of the inputted energy of this process in comparison with MIG welding, as modes of hybrid welding control conditions of significant reduction of temperature gradients lengthways of the joints.

Difference in the levels and patterns of distribution of residual strains (distortion) of the joints prepared by MIG and MIG + LB welding, is to a considerable degree connected with the dimensions of the fields of active tensile residual stresses and shapes of the weld (see Figure 1). As it was noted above, in hybrid MIG + LB welding the width of the field of tensile residual stresses is 1.5 times smaller. In doing so a reduction (2 times) of the sectional area of the weld occurs basically due to the appreciable reduction of the sectional area of the topside weld. It essentially reduces the level of additional residual stresses from longitudinal $\sigma_{bend(x)}$ and transverse $\sigma_{bend(y)}$ bends of samples made by hybrid welding (Figure 3).

In MIG welding the residual longitudinal bend of joints causes occurrence on the top surface of the joints of additional compressing residual stresses, and on its reverse side of tensile stresses $\sigma_{bend(x)}$. At cross section *I–I* on the top surface, $\sigma_{bend(x)}$ reach their maximal values at the edges of the sample and minimal near the weld (Figure 3, *a*), while in longitudinal section *III–III*, $\sigma_{bend(x)}$ are characterized by low-level wave distribution (Figure 3, *b*). The joints produced by MIG + LB welding have a longitudinal reverse bend. Thus on the top surface of the sample, low-level longitudinal tensile residual stresses, whilst on its underside compressing residual bending stresses $\sigma_{bend(x)}$, are additionally formed. At cross section *I–I* on the top surface of the joint they are distributed uniformly, while at longitudinal section *III–III* tensile stresses concentrate mainly in the middle of the sample (Figure 3, *a*, *b*).

The joints prepared by MIG welding, have greater transverse and longitudinal bending than those by MIG + LB welding. At transverse section *II–II* on the top surface of the butt joint made by MIG welding, additional transverse tensile residual bending stresses $\sigma_{bend(y)}$ reach a high level mainly in the weld zone (70 MPa); near the edges of the sample they are transformed into the compressing residual stresses reaching values as low as –70 MPa (see Figure 3, *c*, *d*). At longitudinal section *IV–IV* high transverse tensile residual bending stresses $\sigma_{bend(y)}$ act along the whole length of the near-weld zone with some recession in the end of the weld (105 MPa in the beginning and 55 MPa in the end). For the joints made by MIG + LB welding, the transverse residual bending stresses $\sigma_{bend(y)}$ at section *II–II*, on the top surface near the weld, are compressing, while near the edges they are tensile, their values not exceeding ±20 MPa (Figure 3, *c*). In the joints made by hybrid method, transverse residual bending stresses $\sigma_{bend(y)}$ in longitudinal section *IV–IV* are mainly compressing, they act along the whole length of the near-weld zone, their magnitudes not exceeding 40 MPa, with an appreciable recession in the central part of the sample to as low as –10 MPa (Figure 3, *d*).

Thus, in welding of thin-sheet specimens in butt joints there arise averaged in thickness (nominal) biaxial residual stresses balanced in cross sections. These stresses are augmented by stresses from the bend, caused by the loss of stability of plates from the action of compressing (balancing) residual stresses in the near-weld zone and additional moments from shrinkage of the weld owing to non-equilibrium of its top and root protrusions and non-uniformity of plastic strains over the thickness of the HAZ. Therefore, total distribution of residual stresses measured only on the surface of the welded joint, is unbalanced.

Wave distribution of transverse components of residual stresses $\sigma_{res(y)}$ in the near-weld zone of through thickness MIG-welded butt joints, was reported earlier [2]. Obviously, transverse stress component tends to the balanced condition on shorter than the weld length distances, which testifies to independent formation of longitudinal and transverse components of residual stresses. In so doing the nonequilibrium condition of the components of residual stresses in two orthogonally related sections of the welded joint is defined by the law on independence of the longitudinally and transversely oriented elastic balanced forces. It means that both at external (elastic) loading of the sample and at elastic relieving of the residual stresses, two components of elastic longitudinal and transverse stresses conform to the principle of superposition (or independence of action of forces) [8]. Therefore, at cutting the sample along the weld there occurs full relieving of transverse forces and moments and partial relieving of longitudinal forces and moments, caused by cessation of actions of the opposite moments of the cut off part of the joint. At cutting the sample across the weld, transverse residual stresses retain their magnitudes if in the cut out sections of the joints they are locally balanced, whilst longitudinal residual stresses decrease and near the cutting line are equal to zero.

CONCLUSIONS

1. In comparison with traditional MIG welding, the hybrid high-speed welding with a consumable electrode in combination with CO_2-laser in argon, of thin-sheet aluminum alloy AMg6 butt joints, promotes significant reduction of transverse residual strains and stresses due to a six-fold increase in welding speed, 40 % decrease of its inputted energy and two-fold reduction of the weld section.

2. In traditional MIG welding of thin-sheet aluminum alloys, in the near-weld zone of the butt joints are formed transverse residual stresses whose distribution has a wave character. Their averaged extreme values amount to ±80 MPa in the first wave, which extends to the distance of 100–120 mm from the weld beginning. The transverse residual bend initiates additional transverse residual stresses arising on the surface of butt joint, equaling ±105 MPa in its beginning and ±55 MPa in its end.

3. In hybrid MIG + LB welding, values of transverse residual stresses in the near-weld zone are not higher than ±20 MPa, and those of additional transverse residual stresses due to bend of sample are about ±40 MPa. The field of longitudinal tensile residual stresses narrows 1.5 times in comparison with corresponding residual stresses in the joints made by MIG welding.

1. Gatovsky, K.M. (1980) Strains and stresses in welding of structures. In: *Welding of shipbuilding structures*. Leningrad: Sudostroenie.
2. Shonin, V.A., Gushcha, O.I., Mashin, V.S. et al. (2005) Influence of the dimensions of a specimen of aluminium alloy welded joint on the residual stressed state and fatigue resistance. *The Paton Welding J.*, **2**, 18–28.
3. Staufer, H., Hackl, H. (2001) Laser-MIG process for automotive industry. *Ibid.*, **12**, 26–29.
4. Dilthey, U., Lueder, F., Wieschemann, A. (1999) Erweiterte Moeglichkeiten beim Schweissen von Aluminiumlegierungen durch den Laser-MIG-Hybridprozess. *Aluminium*, 75(**1/2**), 64–75.
5. Shida, T., Hirokawa, M., Sato, S. (1997) CO_2-laser welding of aluminium alloys (welding of aluminium alloys using CO_2-laser beam in combination with MIG arc). *Q. J. JWS*, 15(**1**), 18–23.
6. Kasatkin, B.S., Kudrin, A.B., Lobanov, L.M. et al. (1981) *Experimental methods of strain and stress investigations*. Kiev: Naukova Dumka.
7. Vinokurov, V.A. (1968) *Welding strains and stresses*. Moscow: Mashinostroenie.
8. Feodosiev, V.I. (1986) *Strength of materials*. Moscow: Nauka.

CALCULATION TECHNIQUE FOR DEFINING PARAMETERS OF SOLDERED SEAM SOLIDIFICATION

E.A. DENISEVICH
National Technical University of Ukraine «Kiev Polytechnic Institute», Kiev, Ukraine

Described is the technique of defining the condition of stability of flat solidification front of soldered seams on copper Ì 1 with self-fluxing solder on the basis of Sn–Pb--Bi system low-melting alloy and surfactants as fluxing components of the soldering composition. Solidification is the final stage of soldered seam formation and their service characteristics depend on conditions of its proceeding in soldered joints. Studying the process of solidification of soldered seams by calculations opens up opportunities for forecasting technological parameters of soldering processes. The characteristics obtained as a result of calculation enable to adjust technological conditions of soldering in order to improve service characteristics of soldered joints.

Keywords: soldering, copper, solidification, flat front, calculation technique

Specific nature of the soldering process is that solidification of soldered seams proceeds with high rate advancing from the surface of soldered metal contacting the solder melt, and is non-equilibrium. Non-equilibrium conditions of solidification are connected with small volume of solder melt in the gap and specific geometry of the solidifying solder melt layer which has small thickness and is confined between solid surfaces. During solidification of soldered joints takes place controlled heat transfer in the direction of soldered metal, an insignificant superheating of solder melt in the joint zone, as the soldering temperature is close to the point of solder solidification onset.

The calculations of conditions of flat solidification front stability presented in this work for low-temperature Pb–Sn--Bi system used for solder-mounting of electro-technical devices are based on fundamental works [1, 2] quantitatively and qualitatively describing the processes of liquid phase solidification, depending on its composition and solidification conditions.

Setting the problem and theoretical generalizations. Calculation of solidification parameters of a three-component 22 % Pb–25 % Sn–53 % Bi alloy begins with the analysis of the constitutional diagram of Pb--Sn--Bi system; necessary for calculation characteristics were determined from reference materials (Table, Figure 1).

Multicomponent alloys, in the same way as two-component, can form a flat solidification front, if the temperature gradient at the solidification front is high enough, and crystal growth rate is small. To these alloys can be applied both criteria of concentrational supercooling, and the theory of solidification front stability, as it is made in [3] for three-component alloys.

In describing solidification of 22 % Pb--25 % Sn–53 % Bi solder, the condition for flat front solidification stability consists in that the gradient of actual temperature on the interface between solid and liquid phases defined by technological factors, can be equal or greater than gradient of liquidus temperature in a ternary system. The three-component alloy 22 % Pb–25 % Sn–53 % Bi during solidification can have single-, two- and three-phase composition.

Initial data for calculation of parameters of Pb–Sn--Bi alloy system solidification

Parameter	Value
Component concentration in solder C_{sol}, wt.% / at.%:	
lead	22 / 27
tin	35 / 35
bismuth	53 / 38
Component concentration in ternary eutectic C_e, wt.% / at.%:	
lead	32 / 32
tin	16 / 22
bismuth	52 / 46
Component concentration in binary eutectic, wt.% / at.%:	
lead in eutectic Sn–Bi	42 / 57
tin in eutectic Pb–Bi	56 / 56
Melting temperature T_{melt}, °Ñ:	
lead	327.3
tin	231.9
bismuth	271.0
Solder liquidus temperature $T_L^{Pb-Sn-Bi}$	120.0
Eutectic melting temperature T_e^{melt}, °Ñ	
Pb--Sn–Bi	96.0
Pb--Bi	123.0
Sn–Bi	137.0
Pb--Sn	183.3
Solidification heat ΔH, kJ / mol:	
lead	–4.772
tin	–7.07
bismuth	–10.9

© E.A. DENISEVICH, 2006

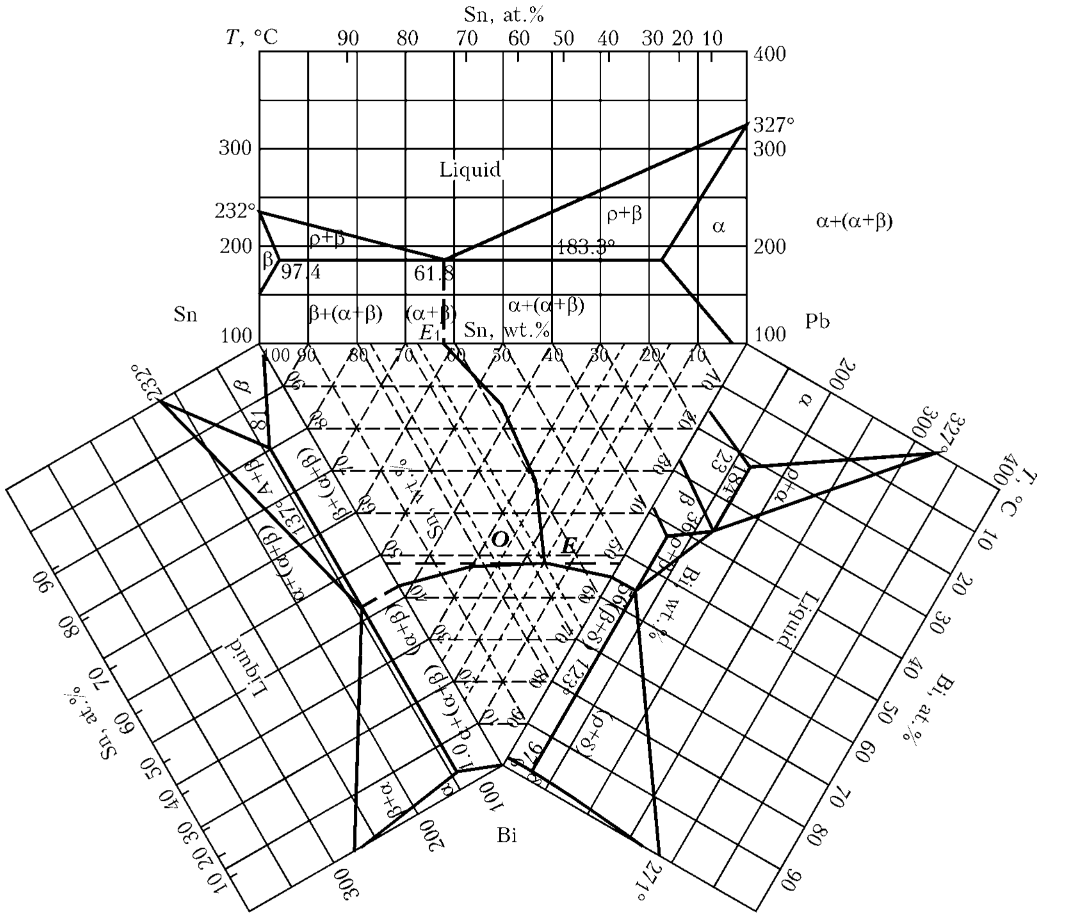

Figure 1. Projection of liquidus surface of ternary Pb–Sn–Bi system: point O corresponds to solder composition: Pb = 22 wt.% (27 at.%); Sn = 25 wt.% (35 at.%); Bi = 53 wt.% (38 at.%); T_L = 120 °Ñ; point E — composition of ternary eutectic in Pb–Sn–Bi system: C_e^{Δ} = = 16 % Sn (22 at.% Sn); C_e^{Δ} = 32 % Pb (32 at.% Pb); C_e^{Δ} = 52 % Bi (46 at.% Bi); T_{melt} = 96 °Ñ

The isothermal section of the constitutional diagram of Pb–Sn–Bi system at T_{melt} = 96 °Ñ is shown in Figure 2.

The 22 % Pb–25 % Sn–53 % Bi alloy (point O) starts to solidify with formation of α-phase, i.e. a tin-based solid solution. Bismuth-enriched intercrystalline liquid moves in the process of solidification approximately radially, in respect of «tin» corner of the diagram, advancing along the solidification line. As it crosses the binary eutectic line, on reaching the point $\hat{I}_1$, on line E_2E starts solidification and growth of binary eutectic Sn–Bi (α + β); composition of a

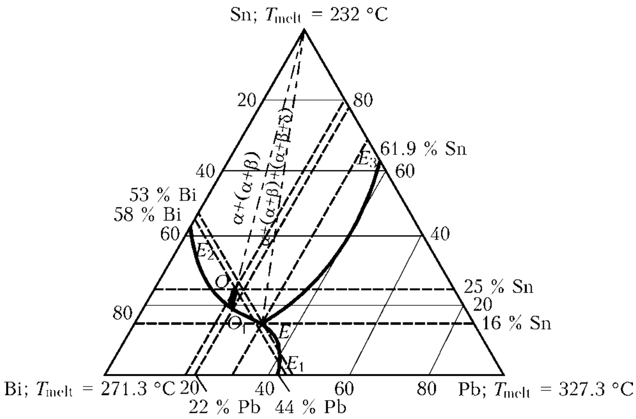

Figure 2. Isothermal section (T_{melt} = 96 °Ñ) of constitutional diagram of Pb–Sn–Bi system

liquid phase changes as shown by the curve E_2E along the line of two-phase equilibrium to E point, i.e. the point of ternary eutectic formation at 96 °Ñ. At this temperature the remainder of the liquid phase solidifies forming a ternary eutectic.

Composition of the liquid phase in the point of ternary eutectic formation, E, is, wt.%: Pb = 32, Sn = = 16, Bi = 52. In that point a constant-temperature solidification comes to an end. The alloy having a eutectic composition is most low-melting, the temperature of this alloy solidification onset and end is T_e = 96 °Ñ. Ternary eutectic α + β + δ consists of three solid solutions; binary eutectic consists of two solid solutions α + β. During solidification intercrystalline liquid is most often enriched with the dissolved substance, until its composition reaches a minimum on the liquidus surface, for example a ternary eutectic composition. In a general case initially one phase is formed, and as it grows, composition of the melt and the temperature change, thus defining the path of solidification on the liquidus surface, i.å. a line of the liquid phase chemical composition change on the constitutional diagram. When this line reaches a binary eutectic line, formation of the second phase begins. The solidification path coincides with the line of binary eutectic up to the point of ternary eutectic.

Results of calculations. Just as with two-component alloys, the condition of flat solidification front stability in Pb–Sn–Bi system consists in that the gradient of actual temperature on the surface of distribution of solid and liquid phases can be equal or greater than the gradient of liquidus temperature in a ternary system.

The criterion of concentrational supercooling, which defines stability of the flat solidification front, is calculated for the beginning of solidification process and for the conditions of eutectic solidification.

In the beginning of solidification the criterion of concentrational supercooling G_l / V is defined on the assumption of equilibrium conditions at the solidification front:

$$\frac{G_l}{V} \geq \frac{m_l^{Pb} C_{0\,Pb}(1 - K_{Pb})}{K_{Pb} D^{Pb-Bi}} - \frac{m_l^{Sn} C_{0\,Sn}(1 - K_{Sn})}{K_{Sn} D^{Sn-Bi}},$$

where G_l is the gradient of temperature in the melt at the solidification front; V is the crystal growth rate; D^{Pb-Bi}, D^{Sn-Bi} are the diffusion coefficients of dissolved in melt elements; K_{Pb}, K_{Sn} are the equilibrium distribution coefficients of the dissolved lead and tin determined as for binary alloys; $C_{0\,Pb}$, $C_{0\,Sn}$ are the initial concentrations of the dissolved lead and tin in solder melt; m_l^{Pb}, m_l^{Sn} are the slopes of liquidus lines, defined from the double constitutional diagram.

At solidification of three-phase alloys the composition of liquid at the front is approximately equal to eutectic (C_e^{Pb} and C_e^{Sn}). Therefore conditions of stability of flat solidification front can be obtained from the previous equation, replacing the composition of a liquid at the solidification front with eutectic composition:

$$\frac{G_l}{V} \geq \frac{m_l^{Pb}(C_{e\,Pb} - C_{0\,Pb})}{D^{Pb-Bi}} - \frac{m_l^{Sn}(C_{e\,Sn} - C_{0\,Sn})}{D^{Sn-Bi}},$$

where $C_{e\,Pb}$, $C_{e\,Sn}$ are the contents of components in the ternary eutectic.

Some difficulties in calculations are due to the presence on the constitutional diagram of the liquidus surface, rather than liquidus lines, and the possibility of diffusion interactions of the dissolved components. Use of the criterion of concentrational supercooling in this case is more involved, as for definition of distribution coefficients using the constitutional diagram, it is necessary to resort to conoids which are known only for a small number of systems. However, if liquidus and solidus surfaces are planes connected with conoids, distribution coefficients K_{Pb} and K_{Sn}, and also slopes of liquidus surfaces m_l^{Pb} and m_l^{Sn} are constant and can be determined from corresponding double constitutional diagrams.

Calculation of solidification parameters should begin with definition of diffusion coefficients of the dissolved components for Pb–Bi, Pb–Sn and Sn–Bi systems by the formula [3, 4]:

$$D_l = D_0 \exp\,(-Q / RT).$$

Let us determine diffusion coefficients in Pb–Bi, Pb–Sn and Sn–Bi systems:

$$D^{Pb-Bi} = 1.83 \cdot 10^{-5} \exp\left(\frac{-18.4}{8.314 \cdot 373}\right) = $$
$$= 1.829 \cdot 10^{-5}\ \text{cm}^2 / \text{s};$$
$$D^{Pb-Sn} = 2.79 \cdot 10^{-5} \exp\left(\frac{-8}{8.314 \cdot 373}\right) = $$
$$= 2.962 \cdot 10^{-5}\ \text{cm}^2 / \text{s};$$
$$D^{Sn-Bi} = 2.61 \cdot 10^{-5} \exp\left(\frac{-10.3}{8.314 \cdot 373}\right) = $$
$$= 2.601 \cdot 10^{-5}\ \text{cm}^2 / \text{s}.$$

The experimental data reported in [3], testify to some interaction of the components: important can be cross diffusion coefficients D^{Pb-Sn} and D^{Sn-Pb}; probably also that distribution coefficients resulting from conoids directions depend on the melt composition.

The slope of liquidus surface is determined by the formula

$$m_l = \Delta T / C_{l\,max};$$

$$m_l^{Pb} = \frac{T_e^{Pb-Bi} - T_{melt}^{Pb}}{C_e^{Pb}} = \frac{123 - 327}{44} = -4.63\ ^{\circ}\text{C / at.\%};$$

$$m_l^{Sn} = \frac{T_e^{Bi-Sn} - T_{melt}^{Sn}}{C_e^{Sn}} = \frac{137 - 231.9}{57} = -1.66\ ^{\circ}\text{C / at.\%};$$

$$m_l^{Bi} = \frac{T_e^{Pb-Bi} - T_{melt}^{Bi}}{C_e^{Bi}} = \frac{123 - 271}{44} = -3.36\ ^{\circ}\text{C / at.\%}.$$

Crystal growth rate in the solidifying phase at equilibrium solidification can be determined using the formula of [3]:

$$-V = \frac{\Delta H^{Bi}}{4 T_{melt}^{Bi}}\ (\text{cm / s}), \quad -V = \frac{10.9}{4 \cdot 271.3} = 1 \cdot 10^{-2}\ \text{cm / s}.$$

Equilibrium distribution coefficient of a dissolved component at the solidification front is

$$K_{Pb} = 1 - \frac{m_l \Delta H^{Pb}}{V T_{melt}^{Pb^2}} = 1 - \frac{(-4.53)(-4.772)}{(327^2) \cdot 1 \cdot 10^{-2}} = $$
$$= 1 - 0.02 = 0.98,$$
$$K_{Sn} = 1 - \frac{m_l^{Sn} \Delta H^{Sn}}{V T_{melt}^{Sn^2}} = 1 - \frac{(-1.66)(-7.07)}{(232^2) \cdot 1 \cdot 10^{-2}} = $$
$$= 1 - 0.02 = 0.98.$$

Criterion of concentrational supercooling at the initial stage of solidification is

$$\frac{C_l}{V} \geq \frac{m_l^{Pb} C_{0\,Pb}(1 - K_{Pb})}{K_{Pb} D^{Pb-Bi}} - \frac{m_l^{Sn} C_{0\,Sn}(1 - K_{Sn})}{K_{Sn} D^{Sn-Bi}} = $$
$$= \frac{-4.63 \cdot 27 \cdot (1 - 0.98)}{0.98 \cdot 1.83 \cdot 10^{-5}} - \frac{-1.66 \cdot 35 \cdot (1 - 0.98)}{0.98 \cdot 2.6^5} = $$
$$= 1.84 \cdot 10^5\ ^{\hat{\imath}}\text{Ñ / cm}^2.$$

Alloys whose compositions are close to ternary eutectic, can readily form flat solidification front if re-

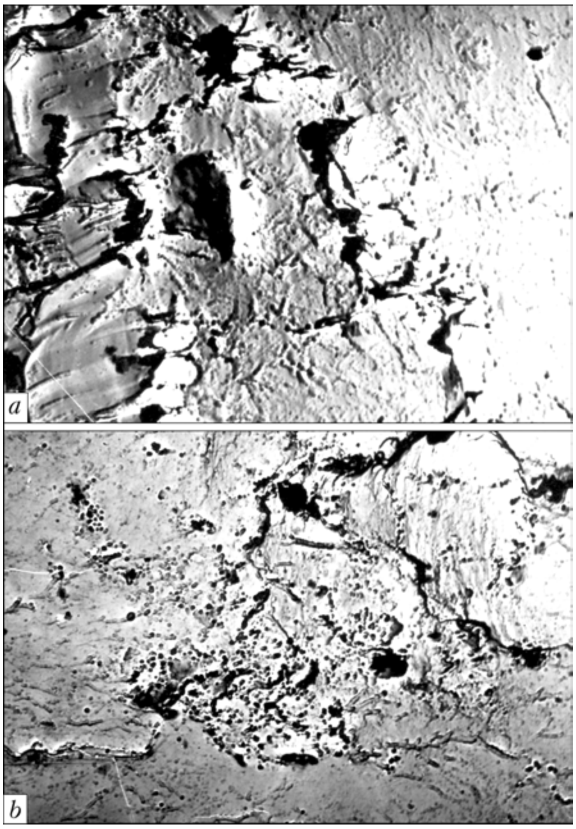

Figure 3. Microstructure of soldered seam (carbon replica): *a* — initial area; *b* — middle area (×8400)

strictions which are placed by the front kinetics, are small:

$$\frac{G_l}{V} \geq \frac{m_e^{Pb}(C_e^{Pb} - C_{0\ Pb})}{D^{Pb-Bi}} - \frac{m_l^{Sn}(C_e^{Sn} - C_{0\ Sn})}{D^{Sn-Bi}} =$$

$$= \frac{(-4.63)(32 - 27)}{1.829 \cdot 10^{-5}} - \frac{(1.66)(22 - 35)}{2.601 \cdot 10^{-5}} =$$

$$= 4.39 \cdot 10^5\ {}^{\hat{\imath}}\tilde{N} / \text{cm}^2.$$

Composition of the liquid phase in equilibrium conditions on solid–liquid interphase is controlled by position of the liquidus surface on the constitutional diagram. Concentration of a solvent component in the melt is assessed at the onset of solidification, i.e. at cooling from T = 120 °Ñ:

$$C_l^{120} = \frac{1}{m_l^{Bi}} (T_{melt}^{120} - T_{melt}^{Bi}) =$$

$$= \frac{1}{-3.36}(120 - 271) = 44.94 \text{ at.\% Bi}.$$

Concentration of a solvent component in eutectic reaction grows:

$$C_l^{96} = \frac{1}{m_l^{Bi}} (T_e^{96} - T_{melt}^{Bi}) =$$

$$= \frac{1}{-3.36}(96 - 271) = 52.08 \text{ at.\% Bi}.$$

The average composition of the solid phase depends on relation G_l / V, respectively concentration of components in the solid phase is

$$C_m^{Sn} = C_e + \frac{D^{Sn-Bi}C_l}{m_l^{Sn}V} = 22 + \frac{2.6 \cdot 10^{-5} \cdot 1.84 \cdot 10^5}{(-1.66)} =$$

$$= 22 - 2.88 = 19.12 \text{ at.\% Sn},$$

$$C_m^{Sn} = C_e + \frac{D^{Sn-Bi}C_l}{m_l^{Sn}V} = 22 + \frac{2.6 \cdot 10^{-5} \cdot 4.35 \cdot 10^5}{(-1.66)} =$$

$$= 22 - 6.80 = 15.2 \text{ at.\% Sn},$$

$$C_m^{Pb} = C_e + \frac{D^{Pb-Bi}C_l}{m_l^{Pb}V} = 32 + \frac{1.83 \cdot 10^{-5} \cdot 4.35 \cdot 10^5}{(-4.36)} =$$

$$= 32 - 1.72 = 30.28 \text{ at.\% Pb}.$$

In the course of solidification the content of the dissolved component in the solid phase gradually increases reaching $(C_s / C_0) = 1$, which conforms to equilibrium distribution of the dissolved component.

The considered solidification type leads to formation of crystals of almost homogeneous composition across the entire joint (based on experimental data of the present author), except for the initial and final transition areas. The initial transition area is formed during the period when the content of the dissolved component in the boundary layer has not yet reached its maximum, which conforms to stationary condition (Figure 3, *a*).

The final solidification area of the soldered seam, i.e. its middle (Figure 3, *b*) is much smaller than the initial, as it results from fast solidification of the last portion melt abundantly enriched with the dissolved component. Thus, the width of this area is governed by a typical distance (size) of the boundary layer or the relation of the diffusion coefficient to crystal growth rate D_l / V. The content of the dissolved component in the final area gradually increases from C to C_e at solidifying, and at concentration exceeding C_{max}, the soldered the seam is two-phase.

The final microstructure of the alloy consists of three phases: α, β, δ. α-phase represents the bulk of the microstructure, wherein about 20 % are primary crystals; the other part solidifies in eutectics (Figure 4).

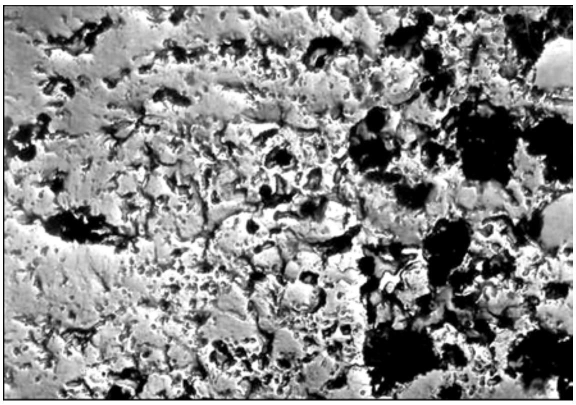

Figure 4. Microstructure of soldered seam (carbon replica) (×6400)

At G_l / V ratio which is not high enough for maintaining stability of the flat front, cells or dendrites of one or two phases sprout from the front into the liquid.

Metallographic investigations of microstructure of Pb–Sn–Bi alloy system conducted by the present author, have shown that at quite high values of G_l / V, also for the alloys significantly differing from eutectic, the structures similar to eutectic have been obtained. Such a phenomenon was revealed for all alloys, except for close to eutectic; for such alloys already small values of G_l / V provide stability of flat solidification front.

CONCLUSIONS

1. Conditions of stability of flat solidification front of soldered seams by calculation methods were defined. The characteristics obtained as a result of calculation, allow adjusting technological conditions of soldering for increasing operational properties of soldered joints.

2. Metallographic analysis of soldered seams confirms conformity of the results of calculation to character of distribution of structures formed in soldered seams.

1. Gulyaev, A.P. (1963) *Metals science*. Moscow: Oborongiz.
2. Flemings, M. (1977) *Processes of solidification*. Moscow: Mir.
3. Hansen, M., Anderko, K. (1962) *Structures of binary alloys*. Moscow: Metallurgizdat.
4. Larikov, L.N., Isajchev, V.I. (1987) *Diffusion in metals and alloys*: Refer. Book. Kiev: Naukova Dumka.

DYNAMICS OF MOVEMENT AND HEATING OF POWDER IN DETONATION SPRAYING OF COATINGS

V.A. ULSHIN[1], **M.Yu. KHARLAMOV**[1], **Yu.S. BORISOV**[2] and **E.A. ASTAKHOV**[2]
[1]V. Dal East-Ukraine National State University, Lugansk, Ukraine
[2]E.O. Paton Electric Welding Institute, NASU, Kiev, Ukraine

Mathematical model is suggested, describing interaction of powder particles with detonation products inside the channel of a detonation unit and in the space between an exit section of the channel and a workpiece. Calculation and experimental results are compared. Peculiarities of behaviour of powder particles in detonation spraying are numerically studied.

Keywords: detonation spraying, coating, process parameters, optimisation, mathematical model, parameters of flow of particles

Velocity and temperature of spray particles are the key parameters determining formation of structure and properties of thermal spray coatings, including the detonation ones. Experimental studies of interaction of powder particles with detonation products are labour-consuming and expensive. Moreover, these studies are hampered by certain peculiarities of detonation spraying of (DS) coatings, such as high velocities of the gas and dispersed phases, small sizes of particles of a powder used, pulsed character of the DS process, etc. In this connection, development of mathematical models and software packages on their base is a topical area in investigation and optimisation of DS processes.

Known studies dedicated to DS usually cover only a one-dimensional acceleration of a dispersed mixture in channel of the detonation unit (DU) [1–4]. Effect of the zone outside the channel on flow parameters is considered in study [5]. However, this study is based on a number of assumptions, which substantially decrease the accuracy of calculations: effect of the dispersed phase on gas is ignored, and automodel solution for the case of a plane detonation wave (DW) is selected to describe initial distribution of the gas flow in the channel, etc.

To optimise the DS process parameters, it is necessary to study peculiarities of heating and acceleration of spray powder particles both inside the DU channel and in the space between the channel and a workpiece, including in application of channels with a section varying along the length.

Mathematical statement of the problem looks as follows. The DU channel with length L, having a cylindrical shape with inside diameter d, or channel with a variable section and outside diameter d, is partially or fully filled with a detonation-capable mixture of gases, having initial pressure p_0, density r_0 and temperature T_0. Gas suspension of solid spherical particles with diameter d_p is inside the channel in region z_1, z_2 ($0 \le z_1 \le z_2 \le L$). DW propagating through the

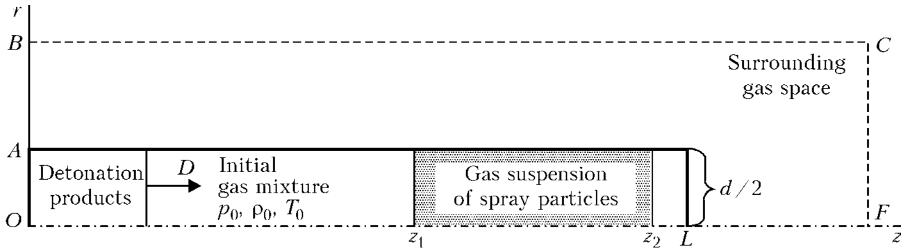

Figure 1. Schematic of the detonation unit channel and calculation region (see designations in the text)

© V.A. ULSHIN, M.Yu. KHARLAMOV, Yu.S. BORISOV and E.A. ASTAKHOV, 2006

mixture at velocity D (Figure 1) is formed in initiation at the left-hand closed end of the channel. After DW reaches the right-hand open end of the channel, the detonation products (DP) and dispersed particles start flowing into the surrounding gas space.

The following assumptions are made in this case: pressure is produced only by gas, effect of powder particles is ignored; viscosity and thermal conductivity of phases are taken into account only in the processes of interaction between the phases; distance at which the flow parameters substantially change is much bigger than size of particles and distance between them; particles are spherical and monodisperse, and do they not enter into chemical reactions with DP; no crushing and collision of particles take place; DP before the beginning of the flow are regarded as a reaction medium having an equilibrium chemical composition at each point, and after the beginning of the flow — as an inert gas with a constant adiabatic exponent; and effect of particles on the DW characteristics is ignored.

The system of equations for the two-dimensional axisymmetric non-stationary movement of gas suspension has the following form [6]:

$$\frac{\partial\rho_i}{\partial t} + \frac{1}{r}\frac{\partial(r\rho_i\nu_i)}{\partial r} + \frac{\partial(\rho_i u_i)}{\partial z} = 0,$$

$$\frac{\partial(\rho_i\nu_i)}{\partial t} + \frac{1}{r}\frac{\partial(r\rho_i\nu_i^2)}{\partial r} + \frac{\partial(\rho_i\nu_i u_i)}{\partial z} + \varepsilon_i\frac{\partial p}{\partial r} = (-1)^i f_r n;$$

$$\frac{\partial(\rho_i u_i)}{\partial t} + \frac{1}{r}\frac{\partial(r\rho_i\nu_i u_i)}{\partial r} + \frac{\partial(\rho_i u_i^2)}{\partial z} + \varepsilon_i\frac{\partial p}{\partial z} = (-1)^i f_z n;$$

$$\frac{\partial(\rho_2 e_2)}{\partial t} + \frac{1}{r}\frac{\partial(r\rho_2 e_2\nu_2)}{\partial r} + \frac{\partial(\rho_2 e_2 u_2)}{\partial z} = qn; \qquad (1)$$

$$\sum_{i=1}^{2}\left[\frac{\partial(\rho_i E_i)}{\partial t} + \frac{1}{r}\frac{\partial(r\rho_i\nu_i E_i)}{\partial r} + \frac{1}{r}\frac{\partial(r\varepsilon_i p\nu_i)}{\partial r} + \frac{\partial(\rho_i u_i E_i)}{\partial z} + \frac{\partial(\varepsilon_i p u_i)}{\partial z}\right] = 0,$$

$$\rho_i = \varepsilon_i\rho_i^0, \quad E_i = e_i + (\nu_i^2 + u_i^2)/2,$$

$$n = 6\varepsilon_2/(\pi d_p^3), \quad \varepsilon_1 + \varepsilon_2 = 1, \quad \rho_2^0 = \mathrm{const}, \quad i = 1, 2,$$

where ν_i and u_i are the components of the velocity in radial, r, and axial, z, directions, respectively; e_i and E_i are the specific internal and total energies of the i-th phase, respectively; f_z and f_r are the components of force interaction of gas with a dispersed particle on cylindrical co-ordinates; q is the intensity of heat input to the surface of an individual particle; and n is the quantity of dispersed particles in unit volume of a mixture. The share of volume of the mixture occupied by the i-th phase is characterised by its volume content ε_i. Each point of volume of the mixture is related to the mean density of phases, ρ_i, characterising mass of a phase in unit volume, as well as to the real density of phases, ρ_i^0, characterising density of their component materials. Indices $i = 1$ belong to the gas phase, and $i = 2$ — to the dispersed phase.

The use is made of the equation of state for an ideal gas:

$$p = \rho_1^0 R T_1/\mu_1, \qquad (2)$$

where R is the universal gas constant; μ_1 is the molecular mass of DP; and T_1 is the temperature of the gas phase.

Before the beginning of the flow of DP the equations derived for the internal gas energy, $e_1(T_1\mu_1)$, and chemical equilibrium $\mu_1(\rho_1, T_1)$ [7, 8] are used for the reacting gas flow in the DU channel. And after the beginning of the DP flow, the following equation is used for the internal gas energy:

$$e_1 = \int_{T_0}^{T_i} c_1(T)dT, \qquad (3)$$

where $c_1(T)$ is the specific heat of gas at its constant volume, and T_0 = 273.15 K.

The equation for the internal energy of the dispersed phase allows for a probable phase transition (melting of particles):

$$e_2 = \begin{cases} \int_{T_0}^{T_2} c_2(T)dT, & \text{if } T_2 < T_{2\mathrm{melt}}, \\ \int_{T_0}^{T_2} c_2(T)dT + (1 - m/m_2)\Delta h, & \text{if } T_2 = T_{2\mathrm{melt}}, \\ \int_{T_0}^{T_2} c_2(T)dT + \Delta h, & \text{if } T_2 > T_{2\mathrm{melt}}, \end{cases} \qquad (4)$$

where $c_2(T)$ is the specific heat of particles; T_2 is the temperature of the dispersed phase; $T_{2\mathrm{melt}}$ is the melting temperature of the dispersed phase; m / m_2 is the relative content of the molten layer with mass m in mass of a particle m_2; $m_2 = (\pi d_p^3\rho_2^0) / 6$; and Δh is the specific melting heat.

The system of equations (1) to (4) is closed by specifying the laws of force and heat interaction between the gas and dispersed phases [9]:

$$f_z = \frac{1}{2}C_d\rho_1^0\Delta\nu(u_1 - u_2)\frac{\pi d_p^2}{4};$$

$$f_r = \frac{1}{2}C_d\rho_1^0\Delta\nu(\nu_1 - \nu_2)\frac{\pi d_p^2}{4}; \qquad (5)$$

$$q = \pi d_p\lambda_1\mathrm{Nu}(T_1 - T_2);$$

$$\Delta\nu = \sqrt{(\nu_1 - \nu_2)^2 + (u_1 - u_2)^2},$$

where C_d(Re, M) is the coefficient of resistance of spherical particles with diameter d_p; Re and M are the Reynolds and Mach numbers, respectively; λ_1 is the coefficient of thermal conductivity of gas; Nu is the Nusselt number; $\Delta\nu$ is the modulus of vector of a relative velocity of the gas and dispersed phases.

The expressions for C_d and Nu are set in the form of the following dependencies [9]:

$$C_d = C_d^0[1 + \exp(-0.427\mathrm{M}^{-4.63})]\,\varepsilon_1^{-k} \quad (k = \mathrm{const});$$

$$C_d^0 = \frac{24}{\mathrm{Re}} + \frac{4}{\sqrt{\mathrm{Re}}} + 0.4 \le \mathrm{Re} \le 2\cdot10^5, \tag{6}$$

$$\mathrm{Re} = \frac{\rho_1^0 \Delta d_p}{\eta}, \quad \mathrm{M} = \frac{\Delta\nu}{a_1}, \quad a_1^2 = \gamma\,\frac{p}{\rho_1^0};$$

$$\mathrm{Nu} = 2\exp(-\mathrm{M}) + 0.45\mathrm{Re}^{0.55}\mathrm{Pr}^{0.33}, \quad \mathrm{Pr} = \gamma\,\frac{c_1\eta}{\lambda_1}.$$

Here C_d^0 is the coefficient of aerodynamic drag of an individual solid spherical particle for conditions of the infinite stationary flow of an incompressible liquid around it; k is the coefficient allowing for restriction of the flow; Pr is the Prandtl number; a_1 and η are the velocity of sound and dynamic viscosity of the gas phase, respectively; and γ is the adiabatic exponent of gas.

The following boundary conditions are assigned. Conditions of no-flow of gas and dispersed particles are set for the symmetry axis and walls of the DU channel. As long as DW does not reach the open end of the channel, its parameters can be found from the relationships for the DW front [10] (the right-hand boundary condition) using Chapman–Jouguet condition $D = u_1 + a_1$. In gradually converging or diverging DU channels, the propagation of DW can be described by the following equation:

$$\frac{dD}{dt} = \left((D - u_1)\,\frac{\partial \ln \rho_1}{\partial z} - \frac{\partial u_1}{\partial z} - u_1\,\frac{d \ln S}{dz}\right) \Big/ \frac{d \ln \rho_s}{dD}, \tag{7}$$

where S is the cross section area of the channel; and ρ_s is the density at the DW front.

After DW reaches the open end of the DU channel, conditions of a free flow of phases are set for open boundaries AB and BC of the calculation region (see Figure 1), and conditions of no-flow for the gas phase and free flow for the dispersed phase are set for right-hand boundary CF, according to [11], i.e. the powder that reaches a barrier is sprayed on it. Depending upon the problem considered, the condition of a free flow of phases can also be set for right-hand boundary CF of the calculation region, like for the rest of the open boundaries.

When studying dynamics of behaviour of individual powder particles, it is assumed that $\varepsilon_2 = 0$, and behaviour of a particle in the non-stationary flow of DP is described by the following equations:

$$m_2\left(\frac{\partial u_2}{\partial t} + \frac{1}{r}\,\frac{\partial(r u_2 v_2)}{\partial r} + \frac{\partial(u_2^2)}{\partial z}\right) = f_z;$$

$$m_2\left(\frac{\partial v_2}{\partial t} + \frac{1}{r}\,\frac{\partial(r v_2^2)}{\partial r} + \frac{\partial(u_2 v_2)}{\partial z}\right) = f_r; \tag{8}$$

$$m_2\left(\frac{\partial e_2}{\partial t} + \frac{1}{r}\,\frac{\partial(r e_2 v_2)}{\partial r} + \frac{\partial(e_2 u_2)}{\partial z}\right) = q.$$

The temperature field in a spherical particle moving in the detonation-gas jet is calculated using the non-stationary equation of heat conduction:

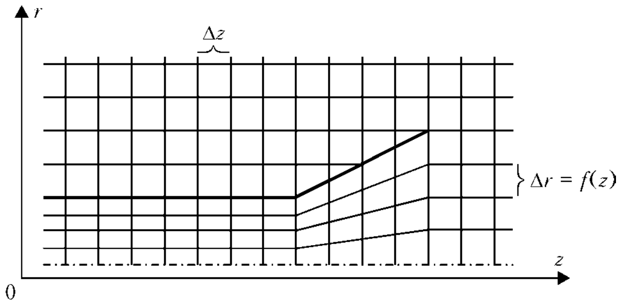

Figure 2. Calculation grid for the channel with a variable section

$$\rho_2 c_2(T)\,\frac{\partial T_p}{\partial t} = \frac{1}{r_p^2}\,\frac{\partial}{\partial r_p}\left(r_p^2 \lambda_2(T)\,\frac{\partial T_p}{\partial r_p}\right), \tag{9}$$

where $T_p(r_p, t)$ is the space-time distribution of temperature; r_p is the space co-ordinate in a symmetric spherical particle; and $\lambda_2(T)$ is the coefficient of thermal conductivity of a particle.

The initial and boundary conditions for equation (9) are set in the following form:

$$T_p(r_p, 0) = T_p^0; \quad \frac{\partial T_p}{\partial r_p}\bigg|_{r_p = 0} = 0;$$

$$-\left(\lambda_2\,\frac{\partial T_p}{\partial r_p}\right)\bigg|_{r_p = d_p/2} = \alpha(T_s - T_g), \tag{10}$$

where T_p^0 is the initial temperature of a particle; T_s is the surface temperature of the particle; T_g is the temperature of DP at a point where the particle is located; and $\alpha = \lambda_2 \mathrm{Nu}/d_p^2$ is the heat transfer coefficient.

The degree of melting of a particle can be determined by solving equation (9) together with the following equation:

$$\rho_2 \Delta h\,\frac{df}{dt} = \lambda_2\,\frac{\partial T_p}{\partial r_p}\bigg|_{r_p = f - 0} - \lambda_2\,\frac{\partial T_p}{\partial r_p}\bigg|_{r_p = f + 0}, \tag{11}$$

where f is the co-ordinate of the melting front. $T_p(f, t) = T_{2\mathrm{melt}}$ at the phase transition boundary.

The problem of the dynamics of a two-phase flow was numerically solved by the method of «coarse particles» [11], and problem of the calculation of temperature field in a spray particle was solved by the method of finite differences. Calculations for the DU channel with a section varying along the length were made using a calculation grid, non-uniform in Δr (see Figure 2).

The software package for computer modelling of the detonation spraying process was developed on the basis of the suggested mathematical model. The package consists of a set of application programs intended for calculation of DW parameters for gas mixtures used in DS of coatings, as well as for modelling of the processes of acceleration and heating of spray powders.

The developed model describing behaviour of the two-phase flow in detonation spraying was experimentally verified using DU with a channel 1.2 m long and 20 mm in diameter. Photosensors were used for evaluation of the velocity of particles [12], and resis-

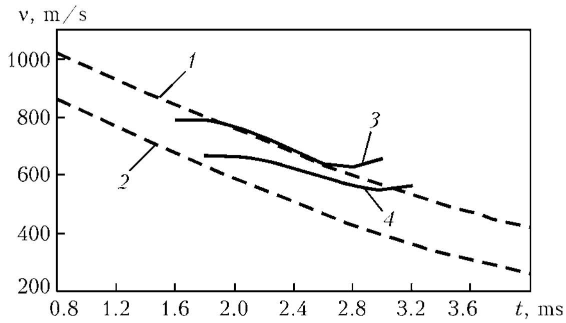

Figure 3. Dependence of the velocity of nickel particles with 20–40 (*1, 2*) and 30 (*3, 4*) μm diameter upon the time of the DP flow: *1, 2* — experimental data; *3, 4* — calculation data; *1, 3* — gas mixture C_3H_2 + 3.5 % O_2; *2, 4* — $C_2H_2 + O_2$; DU channel 1.2 m long with 20 mm diameter; charge 150 mg; loading depth 600 mm; spraying distance 0.2 m

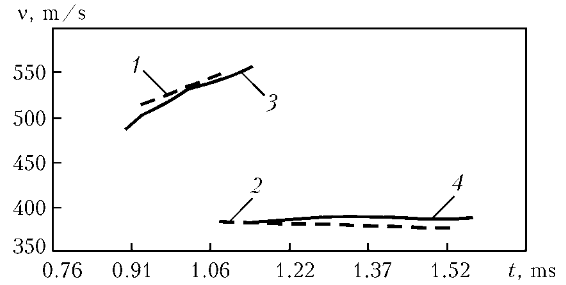

Figure 4. Results of experiments (*1, 2*) [16] and modelling (*3, 4*) obtained at acceleration of aluminium oxide particles in a tube with the diverging nozzle (*1, 3*) and straight-lined tube (*2, 4*): *1, 3* — DU channel 0.75 m long with a nozzle 0.2 m long and 2.9° generating line angle; *2, 4* — DU channel 0.95 m long; gas mixture C_2H_2 + 2.5 % O_2; particle diameter 87 μm; loading depth 300 mm; measurements were made at 35 mm from the exit section of the channel; time from the beginning of the DP flow

tance thermometers in the form of plates of foils were used for temperature measurements [13, 14]. Consider some results of computer modelling and experimental study of behaviour of powder particles in detonation spraying.

Figure 3 shows experimental and calculation curves of variations in the velocity of nickel particles with time of the flow of DP from the DU channel. It was assumed in the calculations that the length of the initial powder cloud in the channel was 0.2 m, and

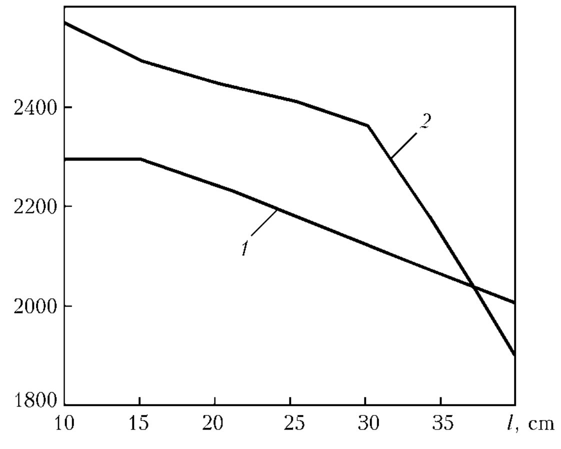

Figure 5. Dependence of temperature of aluminium oxide particles upon the spraying distance: *1* — experimental data; *2* — calculation data; DU channel 1.2 m long with 20 mm diameter; gas mixture C_2H_2 + 1.5 % O_2; particle diameter 10 μm; loading depth 250 mm

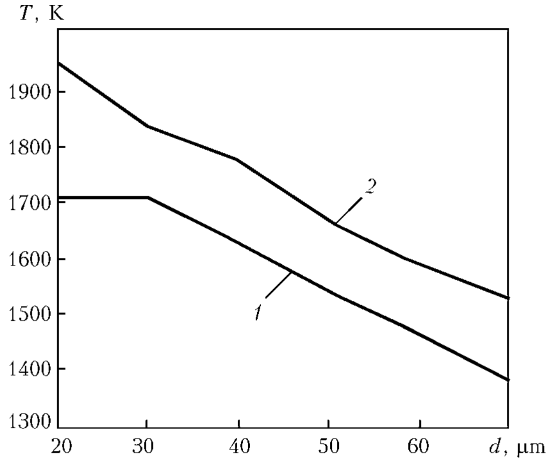

Figure 6. Dependence of temperature of nickel particles upon the particle diameter: *1, 2* — see Figure 5; DU channel 1.2 m long with diameter 20 mm; gas mixture $C_2H_2 + O_2$ + 35 % Ni_2; loading depth 200 mm; spraying distance 120 mm

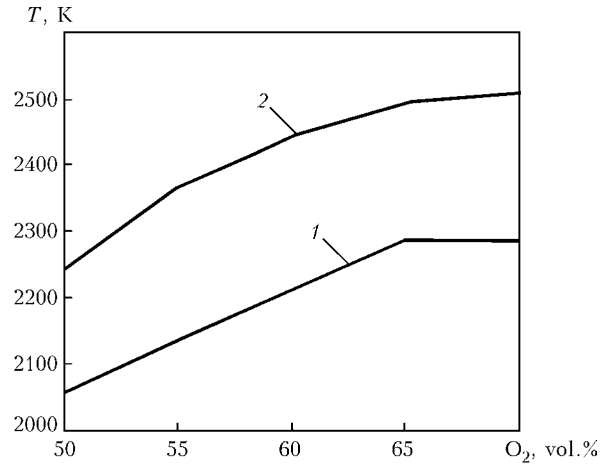

Figure 7. Dependence of temperature of aluminium oxide particles upon the volume content of oxygen in mixture $C_2H_2 + O_2$: *1, 2* — see Figure 5; DU channel 1.2 m long with 20 mm diameter; particle diameter 10 μm; loading depth 250 mm; spraying distance 120 mm

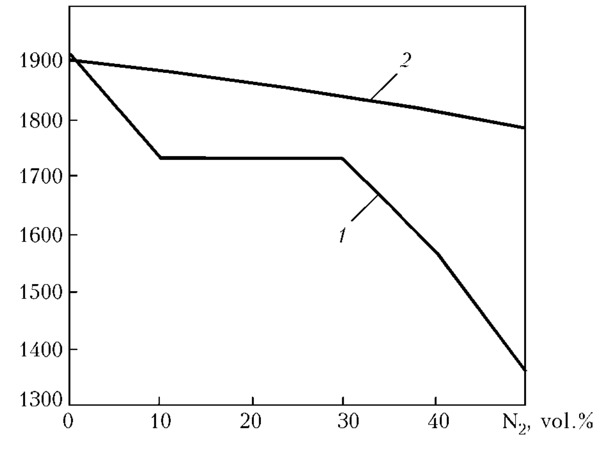

Figure 8. Dependence of temperature of nickel particles upon the volume content of nitrogen in mixture $C_2H_2 + O_2 + N_2$: *1, 2* — see Figure 5; DU channel 1.2 m long with 20 mm diameter; particle diameter 30 μm; loading depth 200 mm; spraying distance 120 mm

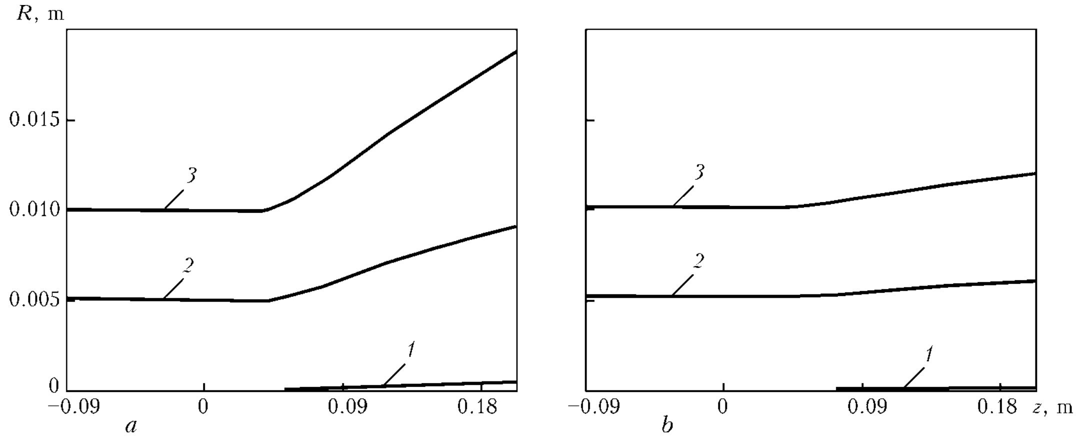

Figure 9. Dependence of path of particles with 40 (*a*) and 85 (*b*) μm diameter upon their initial radial position *R* with respect to the axis of the DU channel: *1* — *R* = 0; *2* — *R* = 5; *3* — *R* = 10 mm; gas mixture C_2H_2 + 2.5 % O_2; DU channel 1.3 m long with 20 mm diameter; loading depth 170 mm; spraying distance 0.2 m; axial co-ordinate is counted from the exit section of the channel

the loading depth was counted from the centre of the gas suspension cloud. Some disagreement of the calculation and experimental data is related to the measurement errors when using photosensors. The main cause of the errors in evaluation of the mean velocity of powder particles is complexity of registration of glow of the two-phase flow. In addition, differences in experimental and calculated values of the velocity of particles are caused by such factors as the use under real conditions of polydisperse powders, which have a non-spherical shape (in this case, finer particles moving at higher velocities radiate more intensively than coarse particles, which also leads to errors), difficulty of exact localisation of the powder cloud in the DU channel, assumptions of a uniform distribution of particles in the initial powder cloud made in modelling, etc.

There are a number of experimental studies [15, 16, etc.] where the dynamics of acceleration of both individual particles and a powder cloud was investigated by the laser visualisation methods. Results of the experiments on acceleration of gas suspension of aluminium oxide particles in a tube with the diverging nozzle [16] and corresponding calculated curves are shown in Figure 4. It follows from the Figure that the DU nozzle employed in study [16] increases the velocity of the Al_2O_3 particles, compared with the straight-lined tube, approximately by 30 % in the case of using the C_2H_2 + 2.5 % O_2 mixture.

The data on temperature of spray particles generated experimentally and by modelling are shown in Figures 5–8. These data are in good agreement, the maximal difference in the absolute value being not more than 15 %. The experimentally measured values of temperature of spray particles are 200 °C lower on the average than the calculations, one of the causes being that the studies did not allow for the processes of heat exchange between the plate with a sprayed coating and environment.

It can be seen from the data shown that the developed model provides a good description of behaviour of powder particles in detonation spraying. An error of about 5 % for the velocity of particles (compared with the data generated by the laser visualisation method) and 15 % for the temperature of the particles can be considered acceptable for investigation and optimisation of parameters of heating and movement of powder particles in the detonation-gas jet.

The developed mathematical model was used to investigate the effect of the initial radial location of powder particles in the DU channel on their subsequent behaviour. The path of the aluminium oxide particles loaded to a depth of 170 mm from the exit section of the channel, located near the wall of the channel, on its axis, and in the intermediate position between the axis and wall of the channel was modelled. The modelling results are shown in Figure 9.

The finely dispersed powder initially located near the channel wall, when it is ejected into the surrounding gas space, is carried away with a diverging gas flow, acquiring a radial velocity (Figure 9, *a*). The angle between the channel axis and movement path is approximately 3°, which is in good agreement with the experimental data [17] generated by the method of super-high-speed photorecording. Particles located on the channel axis insignificantly deviate from the straight-lined path, like coarse particles (Figure 9, *b*) and increased-density particles, independently of their initial radial position. The movement of the particles in the channel is of a straight-lined character.

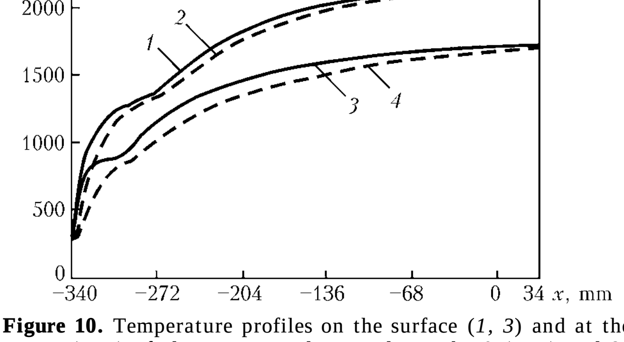

Figure 10. Temperature profiles on the surface (*1, 3*) and at the centre (*2, 4*) of aluminium oxide particles with 50 (*1, 2*) and 85 (*3, 4*) μm diameter along the axis of the detonation-gas jet; gas mixture C_2H_2 + 1.5 % O_2; DU channel 1.2 m long with 21 mm diameter; loading depth 340 mm; axial co-ordinate is counted from the exit section of the channel

The space-time distribution of temperature in a spray particle was determined by calculations using the non-stationary equation of heat conduction (Figure 10). The non-monotonous character of temperature distribution is caused by variations in the velocity of DP in the DU channel and lowering of the temperature of gas surrounding the powder. Rapid drop of the velocity of the gas flow behind the DW front leads to decrease in the Reynolds number for a particle and, accordingly, the Nusselt number characterising heat exchange between the particles and gas (plateau of temperature in Figure 10). Outflow of DW to the exit section and subsequent ingress of DP inside the DU channel are followed by propagation of the rarefaction wave, which causes growth of the velocity of DP and particles and leads to intensification of heat exchange between the phases. Further growth of temperature of the spray particles decreases with decrease in the DP temperature during their outflow from the channel.

CONCLUSIONS

1. The developed mathematical model allows evaluation of space-time parameters of the flow of spray particles both inside the DU channel and in the space between the exit section of the channel and a workpiece (unlike other existing models), including in the case of using variable-section channels. This makes it possible to predict parameters of spray particles immediately before their interaction with a workpiece, allowing for the effect of the spraying distance. The error in experimental and calculation data is not in excess of 5 % for the velocity and 15 % for the temperature of particles. Therefore, the developed model can be applied for numerical investigations and optimisation of the modes of heating and movement of powder particles in detonation spraying.

2. Decrease in density of the material of particles and their diameter leads to increase in the degree of their radial deviation from the initial position. The degree of the radial deviation of particles during their movement depends also upon their initial position with respect to the axis of the DU channel. The radial deviation of the powder particles located on the channel axis is insignificant, but it substantially grows if particles are located near the channel walls.

3. Acceleration and heating in detonation spraying take place in two stages, i.e. behind the detonation wave and in the rarefaction wave. Decrease in the velocity of the gas flow behind the DW front leads actually to the termination of acceleration of particles and decrease in the heat flow between gas and particles. After DW reaches the exit section inside the DU channel, the rarefaction wave starts propagating, leading to increase in the velocity of DP and powder particles, as well as to intensification of heat exchange.

4. The model covers the case of partial filling of the channel with a detonation mixture, where the rest of the channel is occupied by a non-reacting gas. In this case, after DW reaches the gas mixture–non-reacting gas contact boundary, it disintegrates into the shock wave propagating through the non-reacting gas, and rarefaction wave propagating into the opposite direction through DP.

5. The model of movement and heating of powder particles can be applied with expert systems and expert support systems for design of technological processes of detonation spraying of coatings.

1. Gladilin, A.M., Karpilovsky, E.I., Kornev, A.D. (1978) Calculation of parameters of two-phase medium in channel of the detonation unit used for spraying of coatings. *Fizika Goreniya i Vzryva*, **1**, 123–128.
2. Bojko, V.M., Grigoriev, V.V., Zhdan, S.A. et al. (1983) Study of the dynamics of acceleration and heating of metal particles behind the detonation wave. *Ibid*., **4**, 133–136.
3. Gavrilenko, T.R., Nikolaev, Yu.A., Ulianitsky, V.Yu. et al. (1998) Computational code for detonation spraying process. In: *Proc. of 15th Int. Thermal Spray Conf.* (Nice, France, May 25–29, 1998). Ohio: Materials Park.
4. Dolmatov, A.I., Zhemanyuk, P.D. (2001) Numerical modelling of dynamics of two-phase flow in channel of the detonation unit. *Tekhnol. Systemy*, **4**, 12–16.
5. Kantor, L.A., Kantor, S.A., Strongin, M.P. (1987) Calculation of the process of detonation-gas spraying of protective coatings. *Fizika Goreniya i Vzryva*, **4**, 131–135.
6. Nigmatulin, P.I. (1978) *Principles of mechanics of heterogeneous media*. Moscow: Nauka.
7. Zhdan, S.A., Fedenyuk, V.I. (1982) Parameters of equilibrium gas flow in channel of the detonation unit. *Fizika Goreniya i Vzryva*, **6**, 103–107.
8. Nikolaev, Yu.A. (1978) Model of kinetics of chemical reactions at high temperatures. *Ibid*., **4**, 73--76.
9. Ivandaev, A.I., Kutushev, A.G., Nigmatulin, R.I. (1981) *Gas dynamics of multiphase media. Shock and detonation waves in gas suspensions*. Vol. 16. Moscow: VINITI.
10. Baum, F.A., Orlenko, L.P., Stanyukovich, K.P. et al. (1975) *Physics of explosion*. Moscow: Nauka.
11. Belotserkovsky, O.M., Davydov, Yu.M. (1982) *Method of coarse particles in gas dynamics*. Moscow: Nauka.
12. Klimenko, V.S., Skadin, V.G., Sharivker, S.Yu. et al. (1978) Experimental evaluation of dynamic characteristics of two-phase flow in detonation spraying. *Fizika i Khimiya Obrab. Materialov*, **3**, 53–57.
13. Klimenko, V.S., Skadin, V.G., Sharivker, S.Yu. et al. (1978) Determination of temperature of non-electroconductive powder in detonation spraying. *Poroshk. Metallurgiya*, **6**, 78–81.
14. Klimenko, V.S., Skadin, V.G., Sharivker, S.Yu. et al. (1978) Determination of temperature of electroconductive powder in detonation spraying. *Ibid*., **7**, 74--77.
15. Bojko, V.M., Gavrilenko, T.P., Grigoriev, V.V. et al. (1983) Rapid laser visualization of particles accelerated by the detonation wave. *Fizika Goreniya i Vzryva*, **3**, 126–133.
16. Grigoriev, V.V. (1996) Application of nozzle in acceleration of particles by a flow of gas detonation products in tubes. *Ibid*., **5**, 21--29.
17. Zverev, A.I., Sharivker, S.Yu., Astakhov, E.A. (1979) *Detonation spraying of coatings*. Leningrad: Sudostroenie.

ELECTROSLAG WELDING OF BLAST FURNACE HOUSING

Yu.N. LANKIN[1], **A.A. MOSKALENKO**[1], **V.G. TYUKALOV**[1], **R.I. KURAN**[2] and **S.V. POPOV**[2]
[1]E.O. Paton Electric Welding Institute, NASU, Kiev, Ukraine
[2]Company «Yuzhteploenergomontazh», Kiev, Ukraine

Selection of the electroslag welding process for making vertical butt joints of the shells of DP-5 blast furnace housing in Enakievo Metallurgical Works is substantiated. Mechanical properties of the joint metal of 09G2S steel 40–50 mm thick made by electroslag welding with concurrent cooling are given. Technological sequence of assembly and welding with application of site welding equipment AD-381 is described.

Keywords: electroslag welding, blast furnace housing, 09G2S steel, thermal cycle regulation, assembly and welding technology, automatic welding machine

In 2005, the main works on component assembling and welding of the housing of blast furnace # 5 with the capacity of 1513 m^3 and annual production of 1.05 mln t per year were performed at the Enakievo Metallurgical Works. Structural low-alloyed steel 09G2S of 40–50 mm thickness not susceptible to temper brittleness was used for fabrication of welded furnace housing structures.

Typical fabrication design specifies the horizontal position of the furnace housing shells with relative displacement of vertical butts in each tier. With such arrangement of metal sheets 40–50 mm thick, the vertical butt joints of the tiers, the volume of which is 20 % of total length of blast furnace housing welds, can be performed by electroslag welding.

Electroslag welding of 09G2S steel without subsequent high-temperature treatment is possible only under the condition of thermal cycles regulation by means of concurrent forced cooling of the weld and HAZ metal at corresponding welding speed [1] for prevention of negative influence of strength loss on structural strength of welded joints.

Optimizing the modes, industrial certification of electroslag welding technology and verification of its compliance to the requirements of standard technical documentation were done on reference welded joints, made on the materials used in construction of the blast furnace.

The data of mechanical testing of reference welds are given in the Table. The impact toughness of welded joint metal was determined on samples with a round notch by Mesnager at the temperature of 20 °C. Its value should not be lower than 60 J / cm^2 in accordance with SNiP III-18–75 requirements. The value of impact toughness at the distance of 2.5 mm from the fusion line is 158–236, and at the distance of 5 mm — 193–324 J / cm^2.

Investigations of macro- and microstructure showed the absence of non-metallic inclusions, pores, cracks, lacks-of-penetration in the weld cross-section. Structures of base, weld and HAZ metal are a ferrite-pearlite mixture with a certain amount of bainite in the weld metal and near-weld zone.

As the results of studies showed, the properties of welded joints made by electroslag welding by the suggested technology, correspond to the requirements of SniP III-18–75.

Development of the technology of assembly and welding was performed by the E.O. Paton Electric Welding Institute together with specialists from «Yuzhteploenergomontazh». The works on electroslag welding of blast furnace metal structures were done by West-Ukrainian Mounting Administration of «Yuzhteploenergomontazh».

Shells for furnace housing tiers were manufactured directly at the construction site. High requirements were made of the accuracy of geometrical dimensions of the welded joints, as the diameter of the furnace housing was set exactly when welding the longitudinal welds of the shells. The required results were achieved with the help of dozed counteraction method that provided the leveling of the influence of the moment due to the own mass of the product. Assembling of blast

Results of tensile testing of welded joint metal

Joint section	σ_y, MPa	σ_t, MPa	δ, %	ψ, %	*KCU*, J / cm^2
Weld metal	$\frac{423.1–447.8}{433.6}$	$\frac{568.7–603.7}{584.1}$	–	$\frac{70.4–71.6}{71.2}$	$\frac{140–160}{147}$
Base metal	$\frac{306.5–384.0}{335.9}$	$\frac{495.3–579.5}{523.4}$	$\frac{25.3–34.3}{31.1}$	$\frac{68.2–72.1}{70.6}$	$\frac{279–325}{303}$
Welded joint	–	479.6	–	–	–

© Yu.N. LANKIN, A.A. MOSKALENKO, V.G. TYUKALOV, R.I. KURAN and S.V. POPOV, 2006

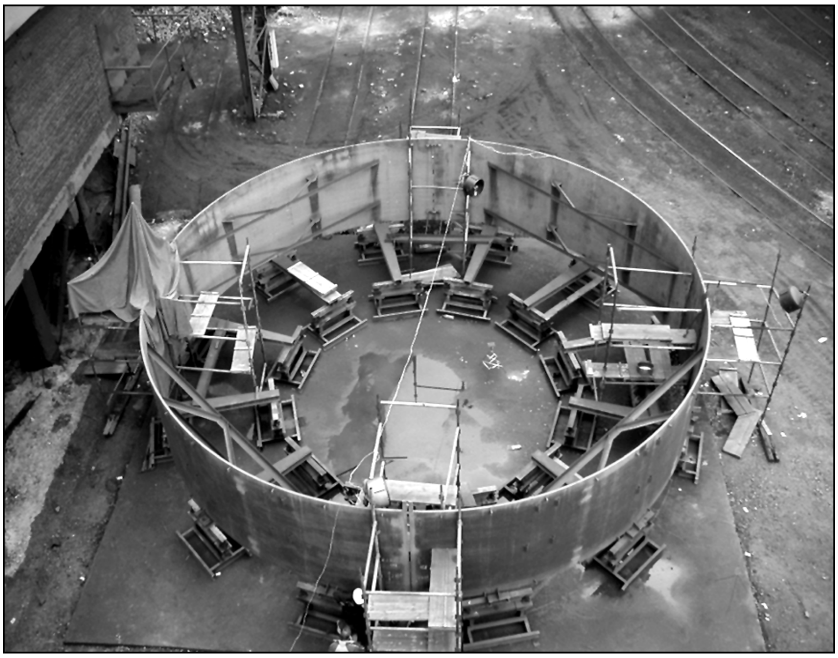

Stand for assembling and welding of blast furnace housing shells

furnace housing sheets into mounting shells and electroslag welding were performed on a special horizontal stand located at the construction site next to the blast furnace housing (Figure).

Vertical butt joints of the shells were assembled with a non-uniform gap, the size of which was greater in the upper part, for compensation of deformations developing in electroslag welding. The butt gap was equal to 25 mm in the lower part. The gap in the upper part depended on the height of the assembled elements (for example, for the shell of the height of 2614 mm it was 48 mm). Fixing cramps with the spacing of 500–600 mm were placed along the entire height of the assembled joint from the external side of the shell.

Furnace housing shell was assembled from four sectors with mounting allowance of 200 mm made from one side of one of the sectors. Butt joint # 2 was made diametrically opposite to # 1, and # 4 — diametrically opposite to butt joint # 3. After welding butt joint # 1 with adjustment of the non-uniform gap for welding depending on the shell height, butt joints # 2 and 3 were assembled with a constant gap of 25 mm along the entire height and were fixed by placing the technological tabs. Butt joint # 4 (with assembling allowance) was assembled and fixed with an overlap, providing parallel edges.

After electroslag welding of butt joint # 1, the required size of the assembly gap in butt joint # 2 was achieved by increasing its width in the upper part of the shell. Cramps that fix the gap were mounted from the external side of the butt joint similar to the first butt joint. Then assembly and welding of butt joint # 3 was performed in a similar fashion after welding the butt joint # 2. Measurement of the shell circumference length in upper and lower parts was performed before assembly of butt joint # 4 for electroslag welding. They were compared with the design values, which was followed by determination of the allowance to be cut off.

Electroslag welding was performed by widely used automatic site welding machine of type AD-381 [2]. Special device — sprayer [3] — was used for concurrent water cooling of the weld and near-weld zone. Welding was performed by two electrode wires of 3 mm diameter and grade Sv-10G2 with AN-8M flux in the following modes: welding speed of 4 m / h; electrode wire feed rate of 280–350 m / h; welding voltage of 40 V.

Optical-visual and ultrasonic methods of control conducted for 100 %, showed that the quality satisfied the requirements of SNiP III-18–75.

The length of welds made by electroslag welding for joining blast furnace housing was equal to 120 m (total — 600 m). Increase of the volumes of electroslag welding application up to 45–50 % is possible when using industrial methods of construction and appropriate design.

Alongside the high technological properties of welded joints, electroslag welding permits a considerable shortening of the terms of construction of blast furnace type structures from low-carbon and low-alloy steels of more than 40 mm thickness.

1. Khakimov, A.N. (1984) *Electroslag welding with adjustment of thermal cycles*. Moscow: Mashinostroenie.
2. Kovalyov, V.D. (2003) Automatic machine AD-381 for electroslag welding with forced formation of vertical joints. *Svarshchik*, **4**, 3.
3. Sushchuk-Slyusarenko, I.I., Khrundzhe, V.M., Volkov, V.V. et al. (1977) Electroslag welding of hydroelectric power station pressure pipelines in thermally-strengthened steel 14Kh2GMR. *Avtomatich. Svarka*, **6**, 68.

STRUCTURE AND COLD RESISTANCE OF WELDED JOINTS IN STEEL 09G2S AFTER REPAIR WELDING

V.D. POZNYAKOV, S.B. KASATKIN and **V.A. DOVZHENKO**
E.O. Paton Electric Welding Institute, NASU, Kiev, Ukraine

Structure and impact toughness of weld and HAZ metal in steel 09G2S under conditions of primary (manufacturing) and repair arc welding are compared. Recommendations are given for selection of welding consumables, taking into account service conditions of repaired items.

Keywords: low-alloy structural steel, manual arc welding, repair welding, microstructure of weld metal, microstructure of heat-affected zone, impact toughness, cold resistance, welding consumables

A great amount of engineering structures and machines which have already exhausted their design service life or are close to it are in operation now both in Ukraine and abroad. Most of them have fatigue and brittle damages. Further operation of such items is no longer safe, based on their technical state. This makes it necessary to recover integrity of structures. In the majority of cases such problems are addressed through repair by arc welding or strengthening treatment of damaged elements [1].

Normally, reconditioning of metal structures is performed using standard welding technologies developed for manufacture of new items. However, they ignore a number of peculiarities characteristic of repair joints, such as a high level of residual stresses and a limited choice of methods for removal of defects, as well as the fact that the use welding and edge preparation may have a substantial effect on properties of welded joints [2--5]. This leads to the need to conduct studies aimed at improvement of repair technologies.

There is much evidence in literature that repair welding affects cyclic strength of repaired joints [6, 7]. A number of measures are proposed to increase their fatigue strength [8–14]. The data on how and to what extent the repair welding process influences a structure of metal and cold resistance of repaired parts are much less abundant. Thus, as reported in [15], repair causes extension of the zone with refined grain, which, however, has no effect on mechanical properties of welded joints. As follows from the data of study [16], multiple repairs lead to a 15–20 % decrease in impact toughness of the HAZ metal of welded joints.

The purpose of this study was to evaluate the effect of repair welding on structure and cold resistance of welded joints in structural steels.

Steel of the 09G2S grade, 30 mm thick, of the following chemical composition, wt.%: 0.096 C, 0.57 Si, 0.71 Mn, was chosen as an object for investigations. In the initial state, the steel has the following mechanical properties: σ_y = 367 MPa, σ_t = 553 MPa, δ_5 = 28 %, KCV_{-40} = 64 J / cm^2. Steel structure in the as-received state was ferritic-pearlitic (FP) (Figure 1).

Specimens of T-joints (type T2, according to GOST 147–71), 120 mm wide and 480 mm long, made by mechanised CO_2 welding using 1.2 mm diameter wire of the Sv-08G2S grade, were used for investigations. The CO_2 welding method was chosen as the most common one for fabrication of general-application structures.

After welding, the specimens were subjected to cyclic loading, brought to complete fracture, and then repaired by fulfilling all technological operations used to perform repair welding (edge preparation and dressing, assembly and welding of joints). Edge preparation (total groove angle of a repair joint was about 60°) was performed by oxy-gas cutting, and after that the edges were dressed with an emery stone to metallic lustre. The joints were assembled using electrodes UONI-13 / 55 and tabs.

Repair welding (the joints were butt welded) was performed by two technologies: traditional one with electrodes UONI-13 / 55 (technology 1), and technology involving combined welds (technology 2). The major portion of a weld was made using electrodes UONI-13 / 55 (ferritic-bainitic (FB) welds), and the final weld layers were deposited using austenitic-martensitic consumables of the Kh10N10 alloying system (austenitic-martensitic (AM) welds). An advan-

Figure 1. Microstructure of steel 09G2S in the as-received state (×200)

© V.D. POZNYAKOV, S.B. KASATKIN and V.A. DOVZHENKO, 2006

Chemical composition (wt.%) of deposited metal produced by using ferritic-pearlitic and austenitic-martensitic consumables

Welding consumable	Ñ	Mn	Si	Cr	Ni	Mo	S	P
FP	0.09	0.90	0.43	--	–	--	0.022	0.026
AM	0.04	0.78	0.32	10.0	10.1	0.58	0.009	0.012

tage of technology 2 was that the AM welds induced compressive stresses in the welded joints, thus increasing their resistance to fatigue fracture [9, 17]. This is very important, as most structures experience cyclic loads during operation. Unfortunately, no data on whether this provides cold resistance of the resulting joints is available in the literature. This issue is still to be studied. Chemical composition of metal deposited by using the above consumables is given in the Table.

Sections for metallographic examinations were made from the repair joints, and standard sharp-notched specimens with a cross section of 10 × 10 mm (type IX, according to GOST 9454–78) were made for evaluation of cold resistance of the weld and HAZ metal. Examination results were compared with those obtained by analysing structure and properties of metal of the butt joints in steel 09G2S made by primary welding using both each of the above consumables and their combinations.

Microstructure of metal of the welded joints was revealed by chemical etching of microsections in 4 % solution of nitric acid in ethyl alcohol, as well as by electrolytic etching in chromic acid. Structure of metal of the welded joints was examined using optical microscope «Neophot-21», and hardness was measured using the «Rockwell» system hardness meter under a load of 600 N, followed by conversion into the Vickers system. Structural components were identified by the results of the microhardness measurements using the PMT-3 instrument under a load of 0.5 Pa.

As evidenced by the results of metallographic analysis, structure of both weld metal and HAZ of the welded joints produced by primary welding using the FP consumables can be identified as FB (Figure 2). Morphologically, bainite consists of globules or, as termed by the authors of study [18], dispersed islands of the second phase distributed in the alloyed ferrite matrix (globular bainite [19]). Bainite globules are chaotically distributed. However, there are some regions where they form rows. Structurally free polyhedral ferrite precipitated along the boundaries of prior austenite grains in the overheated HAZ region, and along the boundaries of crystalline grains in the weld metal (see Figure 2). Microhardness of structure of the overheated region is *HV* 2107--2460 MPa, and that of the weld metal is *HV* 1930--2210 MPa.

Higher values of microhardness of structure of the overheated HAZ region metal are attributable both to a higher degree of dispersion of bainite globules, and to a narrower interlayer of polyhedral ferrite around the prior austenite grains. Average hardness of the HAZ metal is *HV* 2200 MPa, and that of the weld metal is about *HV* 1550 MPa.

More complex composition of structure was fixed in the welded joints produced by primary welding using the AM consumables (Figure 3). Structure of the weld metal in such joints consists of islands of martensite chaotically distributed in austenite. Microhardness of the martensitic component in the austenitic matrix is 1750–2600 MPa, and it depends upon the density of distribution and size of the martensite islands in austenite. Structure of the weld metal is finely dispersed and cellular (see Figure 3, *c*).

There is a transition zone 0.06--0.09 mm wide in the overheated HAZ region near the fusion line. Structure of this zone consists of globular bainite and structurally free polyhedral ferrite, as well as local regions of Widmanstaetten ferrite (see Figure 3, *b*). Microhardness of metal with such a structure is *HV* 2100–2200 MPa. Structure of the overheated region behind the transition zone consists of hypoeutectoid and acicular ferrite, globular bainite (*HV* 2600–2800 MPa), and self-tempered martensite (*HV* 3000 MPa) (see Figure 3, *a*, *b*).

This difference in microhardness values is caused by diffusion of carbon through the overheated HAZ region--weld metal interface [20], which resulted in decarburisation of metal of the overheated region to

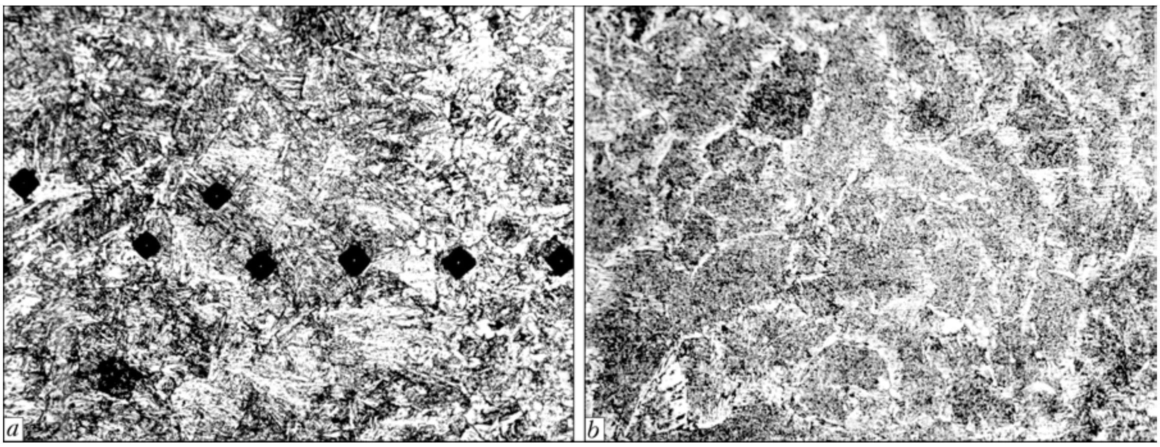

Figure 2. Microstructure of welded joint in steel 09G2S produced by primary welding using FP consumables: *a* — region of overheated HAZ with traces of microhardness (×320); *b* — weld metal (×200)

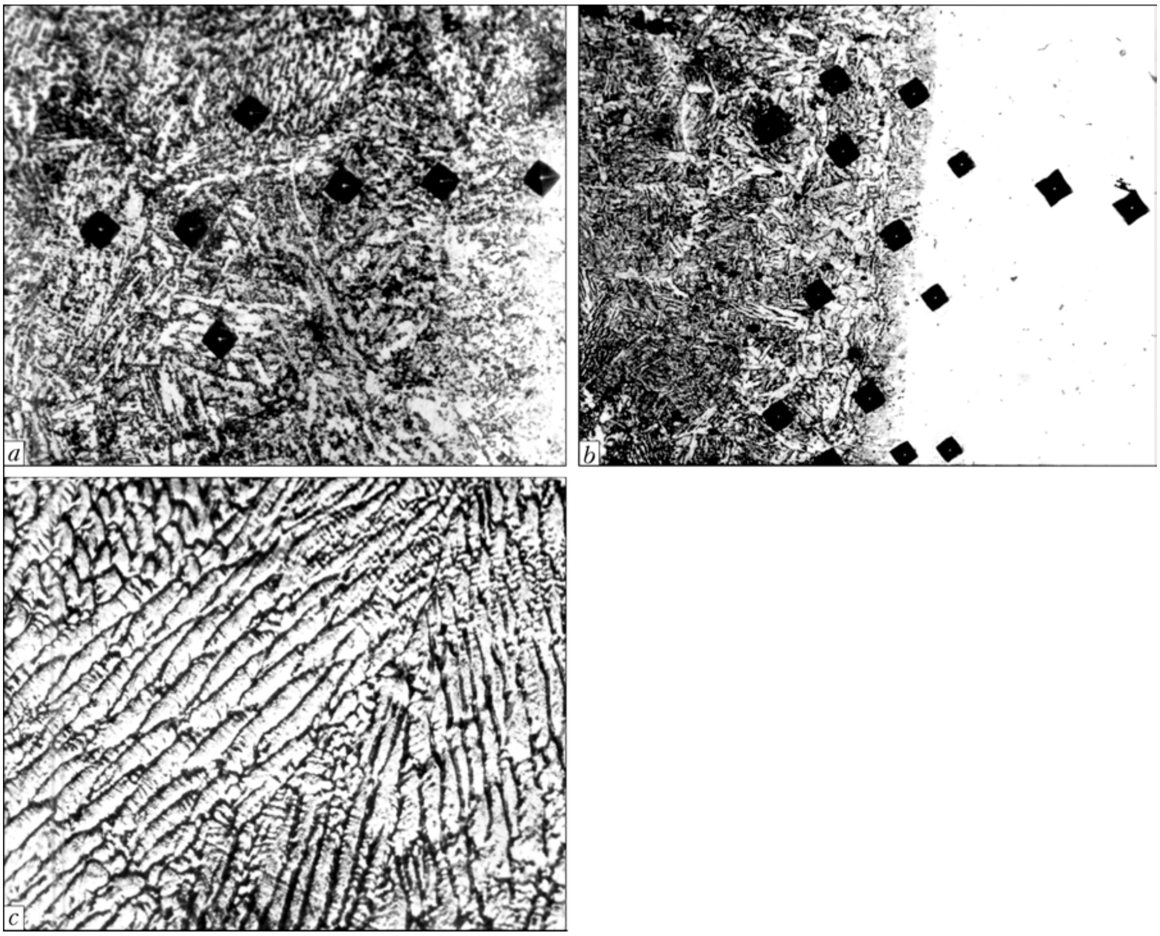

Figure 3. Microstructure of welded joint in steel 09G2S produced by primary welding using AM consumable: *a* — region of overheated HAZ (×500); *b* — region of overheated HAZ and weld metal (×200); *c* — weld metal (×200)

form the transition zone, as well as carburisation of the weld metal. That led to increase in the austenite transformation temperature and formation of softer decomposition products in the transition zone on the side of HAZ, as well as decrease in the austenite transformation temperature in the weld metal region adjoining the fusion line. Diffusion of carbon into the weld metal is evidenced by the fact that in the said region of the weld metal the values of microhardness amount to *HV* 3560–3730 MPa (*HV* 2680–3320 MPa in its central part), and the martensite component content grows, which substantiates variations in size of indentations in measurements of microhardness (see Figure 3, *b*).

The average value of hardness of the weld metal structure is *HV* 1900 MPa, and that of the overheated region is *HV* 2230 MPa.

Metallography of a welded joint produced by primary welding using combined consumables (FP + AM) shows that microstructure of the weld metal and overheated HAZ region, corresponding both to FB and AM deposited metals (Figure 4), is identical to that formed in joints with the homogeneous welds, which were considered above (see Figures 2, *a*; 3, *b*; 4, *a* and *c*).

A peculiar feature of structure of the welded joint with the combined weld (FB + AM) is the presence of a transition zone 0.03–0.13 mm wide not only between the AM weld and HAZ, but also between the lower (FB) and upper (AM) welds (see Figure 4, *b*). This zone is characterised by decarburisation of metal on the side of the FB weld, and carburisation on the side of the AM weld for the above given reasons. As a result, microhardness of metal on the side of the FB region of the weld decreased to *HV* 1800–1850 MPa (the average value of microhardness is *HV* 1650–1970 MPa), whereas that on the side of the AM region of the weld increased to *HV* 3450–3560 MPa (the average value is *HV* 2680–3320 MPa (see Figure 4, *b*)).

Hardness of structure of the AM region of the weld is *HV* 2810–3210 MPa, and that of the adjoining overheated region of HAZ is *HV* 1900–2060 MPa. Metal of the FB weld has hardness *HV* 1520–1570 MPa, and metal of the corresponding overheated region of HAZ has hardness *HV* 1850–2000 MPa.

Results of metallographic analysis of welded joints produced by using a combination of consumables (FM + AM) under the repair welding conditions show that structural changes took place only in the overheated region of HAZ, compared with similar variants of primary welding. No changes in structure of the weld metal occurred.

Microstructure of metal of the overheated region adjoining the AM weld consists of globular bainite (*HV* 2660–2810), hypoeutectoid ferrite in the form of very thin interlayers along the grain boundaries,

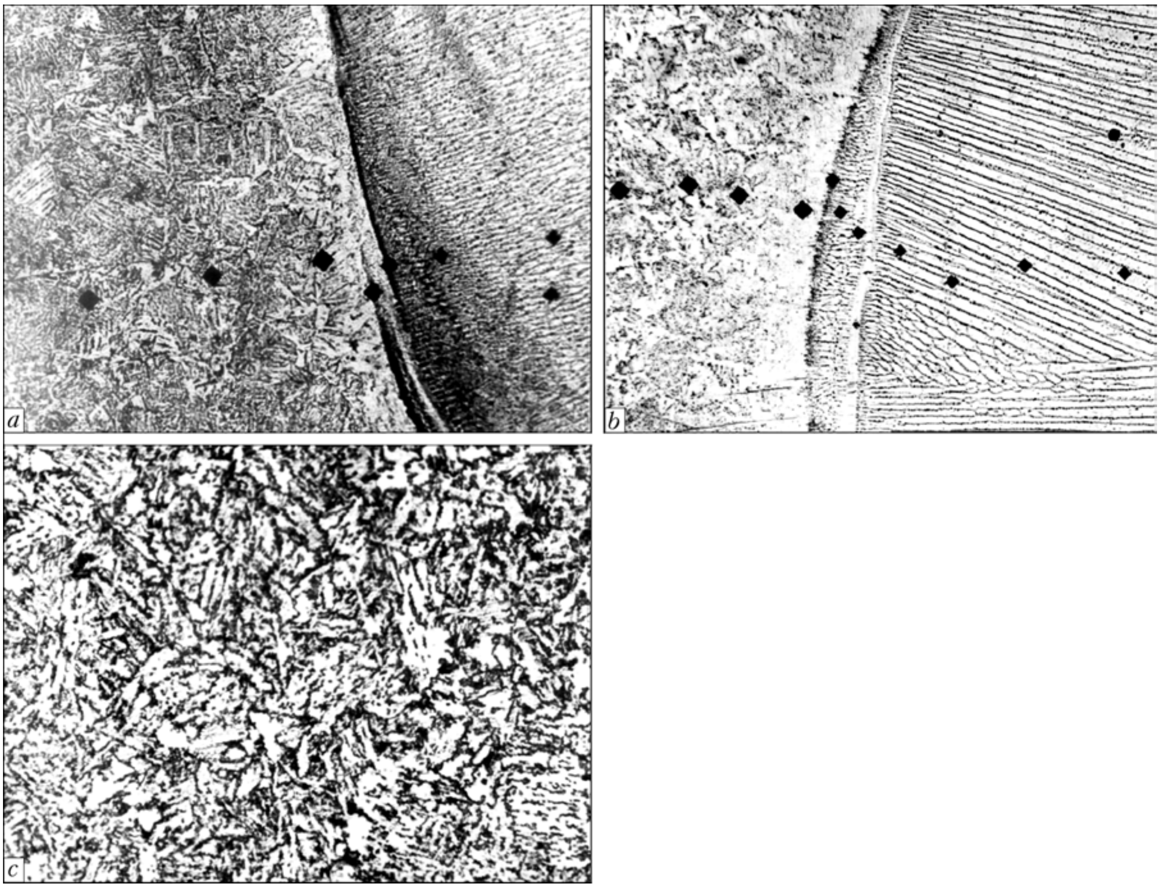

Figure 4. Microstructure of welded joint in steel 09G2S produced by primary welding using combined (FP + AM) consumable: *a* — region of overheated HAZ on the side of AM weld (×200); *b* — transition zone between AM and FB welds (×200); *c* — region of overheated HAZ on the side of FB weld (×500)

local acicular ferrite, and self-tempered martensite with microhardness *HV* 3000–3200 MPa (Figure 5, *a*). In the overheated HAZ region adjoining the FB weld, the metal structure consists of globular bainite (*HV* 2140–2360 MPa) and structurally free polyhedral ferrite that precipitated along the grain boundaries (Figure 5, *c*). Hardness of the HAZ metal is *HV* 1950–2150 MPa.

Comparison of Figures 4 and 5 shows that structural changes consist in that the globular bainite in the overheated HAZ region (Figure 5, *a*, *c*) through the entire thickness of a welded joint has a higher degree of dispersion of secondary phases distributed in bainitic ferrite, and boundary interlayers of hypoeutectoid ferrite have smaller width than similar structural components in the overheated HAZ region in primary welding using combined consumables.

The difference in metal structures of welded joints produced by primary and repair welding is likely to be caused by different conditions of structure formation in the HAZ.

Structure of the overheated region in HAZ of the initial joints was formed under the effect of the welding thermal cycle on the FP structure of steel 09G2S in the as-received state, which resulted in formation of globular bainite. During the repair welding process, the HAZ metal additionally experienced double heating and cooling: firstly, in edge preparation on fractured specimens, which was performed by oxy-gas cutting, and, secondly, directly in welding. In this case, the overheated HAZ region with a globular bainite structure additionally underwent the $F_\alpha \rightleftarrows F_\gamma$ phase transition. Therefore, according to the data of [21], parameters of all stages of austenising in the overheated HAZ region of repair joints should differ from those observed in primary welding of joints in steel 09G2S.

In particular, with the comparable welding cycles, the degree of homogenisation of austenite in such joints was higher, which is evidenced by a decreased scatter of values of microhardness of structural components. This is attributable to two factors: firstly, three-fold heating (austenising), and, secondly, reduction in time of the austenising process, as it is a known fact [21] that increase in the degree of dispersion of the initial structure leads to reduction in time of all stages of austenising. It is apparent that the globular bainite structure formed in the HAZ metal after primary welding is more dispersed than the FP structure of steel in the initial state (see Figures 1 and 2, *a*). Therefore, completeness of the austenising process in repair welding was higher, and the level of homogeneity of austenite was also accordingly higher. As a result, the overheated region of HAZ of the joints produced by repair welding should also have a lower differentiation of austenite in carbon. Hence, structure

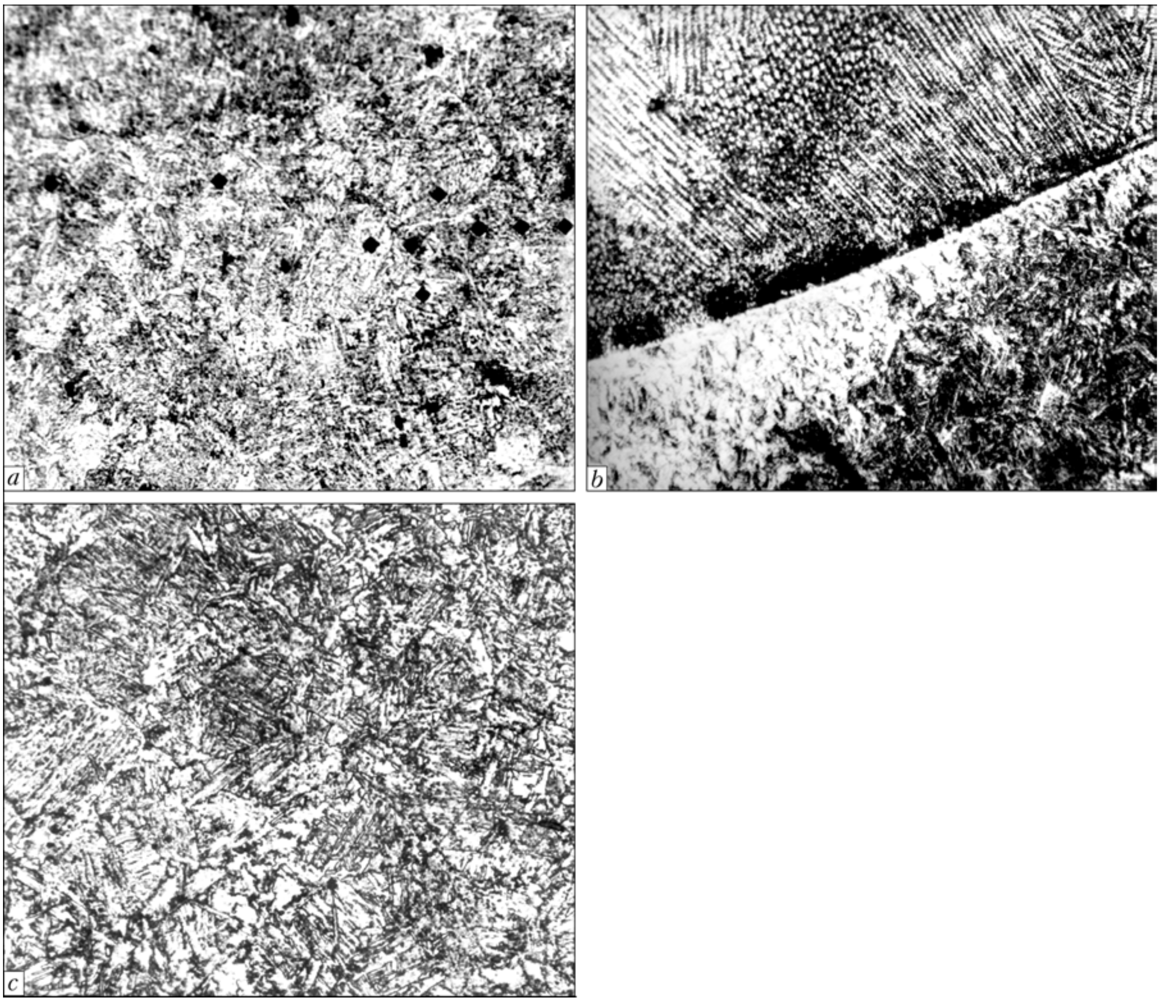

Figure 5. Microstructure of welded joint in steel 09G2S produced by repair welding using combined consumables: *a* — region of overheated HAZ on the side of AM weld (×200); *b* — transition zone between AM and FB welds (×200); *c* — region of overheated HAZ on the side of FB weld (×250)

of this metal should be more homogeneous, dispersed and, therefore, more equilibrium than that of the initial welded joints.

Results of metallographic analysis of structure of the HAZ, FB, AM and combined weld metals of welded joints in steel 09G2S, produced by primary welding and under conditions of repair welding, show that morphology of structural components and, therefore, kinetics of austenite transformation both in the weld metal and in the overheated region are not essentially different. Because structural transformations in arc welding, including repair welding, always occur under conditions of temperature and deformation gradients [22], the welded joints are characterised by this or other degree of concentration and, hence, structural heterogeneity, which we took into account in analysis of the examination results.

The revealed increased degree of dispersion of the transformation products in the overheated region of HAZ seems to be caused by different parameters of austenising in primary and repair welding, which resulted in a decreased degree of differentiation of austenite in carbon, as well as in a reduced temperature range of austenite transformation due to decrease in maximum temperatures. This determined the higher degree of dispersion of the transformation products and led to a decreased scatter of values of microhardness of structural components. The results obtained suggest that, as repair welding causes no substantial changes in structure of the weld and HAZ metal, cold resistance of such joints should be comparable with that of the initial welded joints.

Standard specimens with a sharp notch were made from the above welded joints to evaluate the effect of repair welding on cold resistance of the weld and HAZ metal. Impact toughness of the weld and HAZ metal (in the fusion line and at a distance of 2.5 mm from the fusion line) was determined.

The investigation results show that among the initial welded joints the welds made with the AM consumables had the lowest value of impact toughness at a test temperature of –40 °C (KCV_{-40} = 18–31 J / cm^2). Cold resistance of the FB and combined (FB + AM) welds was a bit higher: 24–40 and 26–43 J / cm^2, respectively.

As proved by investigations into cold resistance of the HAZ metal, among the initial welded joints the highest and most consistent values of impact toughness with a notch made along the fusion line were exhibited by the joints with the AM welds (KCV_{-40} = 51–

53 J / cm^2), and the lowest and inconsistent values of cold resistance were exhibited by the joints with the FB (KCV_{-40} = 18–43 J / cm^2) and combined (FB + AM) (KCV_{-40} = 27–37 J / cm^2) welds. It is likely that this is associated with peculiarities of structure formation in the HAZ metal of such joints.

Values of impact toughness of the HAZ metal in the initial welded joints with a notch located at a distance of 2.5 mm from the fusion line, independently of the type of the weld metal, were close to each other and ranged from 25 to 34 J / cm^2. It should be noted that not only structure of metal in this region of HAZ of all the investigated joints is similar in composition (globular bainite and polyhedral ferrite), but also austenite grains are similar in size.

The investigations conducted show that the weld and HAZ metal of primary welded joints with the FB, AM and combined welds has the first critical brittle temperature ranging from –20 to –40 °C.

As evidenced by comparative analysis of impact toughness of the weld and HAZ metal in primary and repair welding, the insignificant changes in metal structure caused by repeated heating and cooling cycles did not lead to any significant increase or decrease in cold resistance of the said regions of the joints. Only some decrease in scatter between minimum and maximum values of impact toughness took place. Thus, the KCV_{-40} values of metal of repair joints with the FB welds varied from 28 to 36 J / cm^2 (from 24 to 40 J / cm^2 in the initial specimen), while in joints with the combined welds they varied from 30 to 40 J / cm^2 (from 26 to 43 J / cm^2 in the initial specimen). Similar relationship held for the HAZ metal with a notch made along the fusion line. Impact toughness of metal in this region of a repair joint with the FB weld was 28–40 J / cm^2, and that with the combined weld was 30–40 J / cm^2.

Therefore, the investigations conducted indicate to the fact that structure and impact toughness of primary and once repaired joints in steel 09G2S are close in values, provided that the joints were made using identical process parameters.

Repair welding of the joints experiencing cyclic and impact loads during operation should be performed mostly using a combined consumable. Root and filler layers of the weld should be made using consumables that provide its high cold resistance. Compressive stresses should be induced on the surface of welded joints to increase their cyclic strength. This can be achieved by deposition of the final weld layer using the AM consumable. The values of cold resistance of such joints are not lower than those of the welded joints made with the consumables traditionally used for welding steel 09G2S.

1. Branco, S.M., Infanted, V., Maddox, S.J. (1999) A study on the rehabilitation of welded joints. *IIW Doc. XIII-769–99*.
2. Maccocaire, C. (1991) Repair welding: how to set up a shop. *Welding J.*, **8**, 54--56.
3. Donglin Ye, Yongfu He, Rangez Zhang et al. (1982) A study of cracks on the oxygas cut surfaces of weld grooves of 14MnMoVN steel plates during cold forming. *Transact. of China Welding Inst.*, **4**, 159–164.
4. Larionov, V.P. (1986) *Electric arc welding of structures for application in the North*. Novosibirsk: Nauka.
5. Volkov, A.S. (1974) Causes of defect initiation near repaired weld zones. *Svarochn. Proizvodstvo*, **8**, 33--34.
6. van den Brink, S.H. (1989) Reparatielassen. *Lastechniek*, **2**, 40--41, 43, 45, 47.
7. (1996) Recommendation on the repair of fatigue-loaded welded structures. *IIW Doc. XIII-1632--96*.
8. Sergienko, Yu.V., Nosovsky, B.I., Chigarev, V.V. (1998) Improvement of technology for repair of railway wheels using arc welding. *Avtomatich. Svarka*, **3**, 46–48.
9. Ohta, A., Suzuki, N., Maeda, Y. (2001) Extension of fatigue life by additional welds using low transformation temperature welding material. *IIW Doc. XIII-1881--01*.
10. Miki, C. (1997) Repairing and reinforcing of fatigue damaged steel bridges. In: *Proc. of Int. Conf. on Performance of Dynamically Loaded Welded Structures and 5-th Annual Assembly Conf*. (San-Francisco, July 14–15, 1997). New York: Welding Res. Council Inc.
11. Dixter, R.J., Kelly, B.A. (1997) Research on welding repair and improvement methods. *Ibid*.
12. Miki, C., Anami, K., Kaji, H. (1997) Repair of fatigue cracks in bridge structures. *IIW Doc. XIII WG-5-12–97*.
13. Konishi, T., Miki, C. (1998) Fatigue assessment of repaired structural components. *IIW Doc. XIII-1732--98*.
14. Chapeau, W. (1988) Choix d'un mode de reparation des fissures de fatigue dans des constructions soudees. *Rev. Soudure*, **3/4**, 31–35.
15. Lai, M.O., Fong, H.S. (1988) Fatigue performance of repaired pipelines steel weld. *J. Mater. Sci. Let.*, **12**, 1353–1354.
16. Blagojevic, A. (1975) Utjecai popravljana gresaka na kvalitet zavarenog spoja celika povisene cvrtoce. *Zavarivanije*, **4**, 111–122.
17. Ohta, A., Maeda, Y., Suzuki, N. (2001) Fatigue life extension by repairing fatigue cracks initiated around box welds with low transformation temperature welding wire. *IIW Doc. XIII-1835–2000*.
18. Bush, M.E., Kelly, P.M. (1971) Strengthening mechanism in bainitic steels. *Acta Met.*, 19(**12**), 1363--1371.
19. (1972) *Metallography of iron*. Vol. 1. Moscow: Metallurgiya.
20. Shorshorov, M.Kh., Belov, V.V. (1972) *Phase transformations and change in properties of steel in welding*. Moscow: Nauka.
21. Novikov, I.I. (1978) *Theory of heat treatment of metals*. Moscow: Metallurgiya.
22. Hrivnyak, I. (1984) *Weldability of steels*. Moscow: Mashinostroenie.

HIGH POWER DIODE LASER WELDING OF ALUMINUM ALLOY EN AW-1050 A*

A. KLIMPEL, A. LISIECKI, D. JANICKI and **S. STANO**
Silesian University Welding Department of Institute of Technology and Welding, Gliwice, Poland

In this work, results of study on the process of high-power diode laser (HPDL) welding of aluminum alloy AW-1050A are presented. Butt joints of thin aluminum sheets were produced using HPDL ROFIN SINAR DL 020. The influence of welding procedure on mechanical properties and microstructure of welded joints were determined. It was proved that it is possible to produce high quality joints in a wide range of laser welding parameters.

Keywords: laser welding, aluminum alloy, high-power diode laser, black adsorbent, penetration, microstructure

Thanks to high mechanical properties and low density, high corrosion resistance and good plasticity, aluminum alloys are widely used as structural material in industries such as automotive, aircraft, chemical, power construction ones [1, 2]. In the last five years, the consumption of aluminum alloys in automotive industry has increased over 80 %. It is predicted that the mass of aluminum alloys used for a single car manufacture can be increased from approximately 110 kg in 1996 to 250–340 kg in 2015 if used for auto-body panels (Figure 1).

High quality joints of aluminum alloy sheets can be produced by GTA, GMA, PTA welding but welding of thin sheets 3–5 mm thick is very difficult, and impossible by GMA method. Fast development of high-power molecular and solid-state lasers makes that automated and robotized laser welding of aluminum alloy joints are competitive to GTA, GMA and PTA technologies in wide range of thickness because of quality and economical reasons [1, 3, 4].

Laser welding consists in rapid melting of the contact area of sheets being welded by the heat of focused, concentrated and high intensity laser beam [1, 3, 5]. Laser as a flexible heat source of high (over 10^9 W / cm^2) power density (intensity) enables keyhole welding of one-sided joints of aluminum alloys in the thickness range from a few hundreds millimeters up to 20 mm. Mechanical properties of laser-welded joints are not lower than those of base metal, the joints are distortions-free, the weld is very narrow and the HAZ is almost undetectable [1, 4–6].

Main difficulties in laser welding of aluminum alloys are the results of high chemical activity, intensive oxidation, high thermal conductivity and expansion, susceptibility to porosity, loss of alloying elements such as magnesium and zinc during welding, and very low absorption of laser beam energy. For low intensity laser beam, only 1 % of the laser beam energy is absorbed by polished surface of aluminum [3, 5].

Nd:YAG and molecular CO_2 lasers, emitting at 1.06 and 10.6 μm respectively, have found the most extensive application for welding of aluminum alloys [3–5]. Laser welding of aluminum alloys without any absorbents used for increasing the absorption of joint surface, is possible only by technique with keyhole formation.

Slight deviations of spot size of CO_2 and Nd:YAG laser beams lead to significant changes of penetration depth and weld shape defects, and also increase in porosity even when potential sources of hydrogen as a main reason of aluminum alloy weld porosity are eliminated [4, 5].

HPDL, emitting in a range 800–960 nm, are of interest for material processing in many branches of industry. HPDL have many beneficial features compared with molecular CO_2 and solid-state Nd:YAG lasers, especially significantly lower investment and running costs [3, 6, 7].

Conventional HPDL with power density (intensity) of laser beam spot in a range of 10^4–10^5 W / cm^2 and size of beam spot about several square millimeters, can be used only for conduction mode welding. Application of special optics for focusing and forming the laser beam enables to produce circular beam spot of 1 mm in diameter. Circular beam spot of HPDL was successfully used for keyhole welding of the Al–3Mg alloy butt joints 1.5 mm thick at laser power 1400 W and welding speed 0.32 m / min, and also of the Al–1Mg alloy joints 2 mm thick at laser power 2300 W and welding speed 0.35 m / min [6]. Other solution is application of special absorbents for increasing the absorption of laser beam energy on the surface of sheets being welded [8]. In this work, the

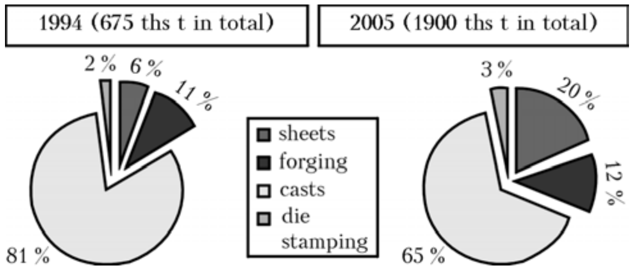

Figure 1. Increase in consumption of aluminium alloys in automotive industry [2]

*This paper was presented at Second International Conference on Laser Technologies in Welding and Materials Processing (Katsiveli, Crimea, Ukraine, May 23–27, 2005) and was published in Proceedings of Conference (Kiev: PWI, pp. 39–42).

© A. KLIMPEL, A. LISIECKI, D. JANICKI and S. STANO, 2005

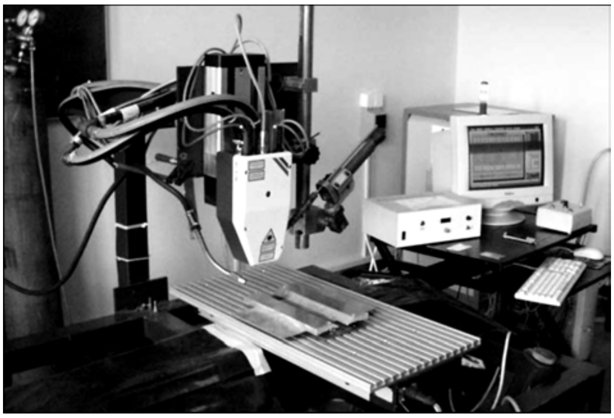

Figure 2. View of experimental setup for HPDL welding of the aluminum alloy butt joints

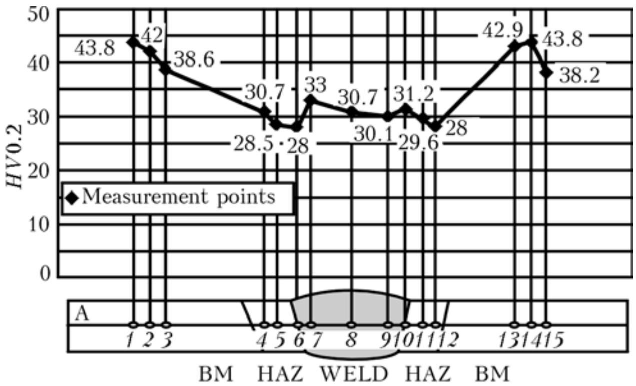

Figure 3. Distribution of microhardness in cross-section of the EN AW-1050A aluminum alloy butt joints 1.0 mm thick at P = = 2.5 kW and v_w = 1.9 m / min

process of HPDL welding of butt joints of aluminum alloy EN AW-1050A (wt.%: min 99.5Al, 0.4Fe, 0.25Si, 0.05Cu, 0.05Mn, 0.05Mg, 0.07Zn, 0.05Ti) 0.8, 1.0 and 1.5 mm thick was investigated. This alloy is used mainly in chemical and food industry for containers and cans.

Results. The investigations were carried out to determine the influence of HPDL welding procedure and parameters on quality and properties of the aluminum alloy EN AW-1050A butt joints 0.8, 1.0 and 1.5 mm thick (Table 1).

Appearance of experimental setup for HPDL welding is shown in Figure 2, technical characteristics of laser ROFIN DL 020, used in the investigations, are presented below:

Wavelength of laser radiation, nm .... 808 ± 5
Maximum output power of laser beam
(continuous wave), W 2300
Laser power range, W .... 100÷2300
Focal length, mm .... 82 / 32
Laser spot size, mm .... 1.8×6.8 / 1.8×3.8
Laser intensity range, kW / cm^2 .... 0.8÷36.5

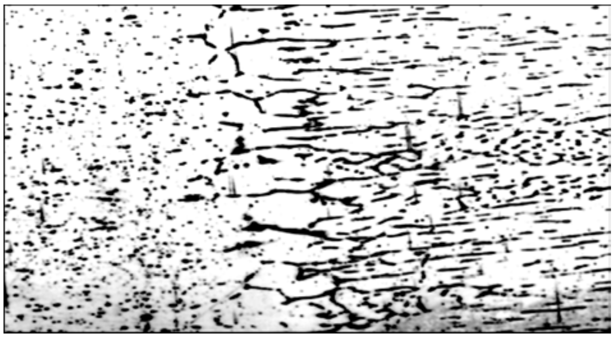

Figure 4. Microstructure of HAZ in the EN AW-1050A aluminum alloy butt joints 0.8 mm thick at P = 2.5 kW and v_w = 0.4 m / min (base metal from the left; etched by the Keller reagent) (×200)

The laser beam spot of 3.8 × 6.8 mm was focused on the top surface of the joints to be welded at focal length of 82 mm. CNC ISEL automation positioning system was used for positioning and moving the joints and laser head. The positioning system consists of three linear stages x, y, z, and one rotary positioner powered by 4-axis servo-controller connected with PC via PC-card. The laser head was fixed to a vertical stage on the z-axis to ensure precision control of the beam spot position. Directly under the laser head a cross-table with two linear stages was placed. The linear stages were moving in two direction along x- and y-axis. Positioning aluminum plate was fixed on the cross-table with special clamping system and graphite backing bar, forming and protecting the weld root (see Figure 2).

Initial laser welding tests have shown that, even at maximum laser power, full penetration in butt joint of the aluminum alloy sheet 0.8 mm thick with cleaned surface can not be achieved. To increase the absorption of the laser beam energy, top surface of the joints were covered by alcoholic solutions of black dye manufactured by Pentel. The tests of laser welding with the absorbent have proven that the absorption of laser beam energy on the joint surface is significantly increased, and it is possible to produce high quality joints in wide range of laser welding parameters. Prior to laser welding edges of the samples to be welded were mechanically cleaned to remove oxides and also degreased, and then the black absorbent was supplied on the joint area surface. The tested joints of the aluminum alloy sheets 200 mm long were laser welded with different heat input by means of various welding speed and laser power. The whole of weld pool and welding zone were protected by argon flow via cylindrical nozzle 12 mm in diameter at constant flow rate of 10 l / min. The results of mechanical, metallographic and microhardness tests are given in Tables 2 and 3 and Figures 3–6.

Table 1. Mechanical properties of the aluminum alloy EN AW-1050A sheets

Thickness, mm	State of strengthening	σ_t, MPa	$\sigma_{0.2}$, MPa	δ, %
0.8	H24 – semi-hard partially recrystallized	105	75	4
1.0		105	75	4
1.5	H14 – semi-hard	105	85	4

Table 2. Influence of the HPDL welding parameters on tensile strength of the EN AW-1050A aluminum alloy butt joints

Laser power P, kW	Welding speed v, m / min	σ_t, MPa
Butt joint 0.8 mm thick		
1.5	1.10	73
1.7	1.65	78
2.5	1.85	74
2.5	2.63	73
Butt joint 1.0 mm thick		
1.5	0.80	80
1.8	1.35	83
2.5	1.30	72
2.5	1.90	75
Butt joint 1.5 mm thick		
2.0	0.7	85
2.3	1.0	82
2.5	0.85	84
2.5	1.25	85

Note. Mean values of three samples are given; joint top surface was covered by black absorbent; zone of sample breaking — HAZ, angle of bending from weld face and from weld root — 180°.

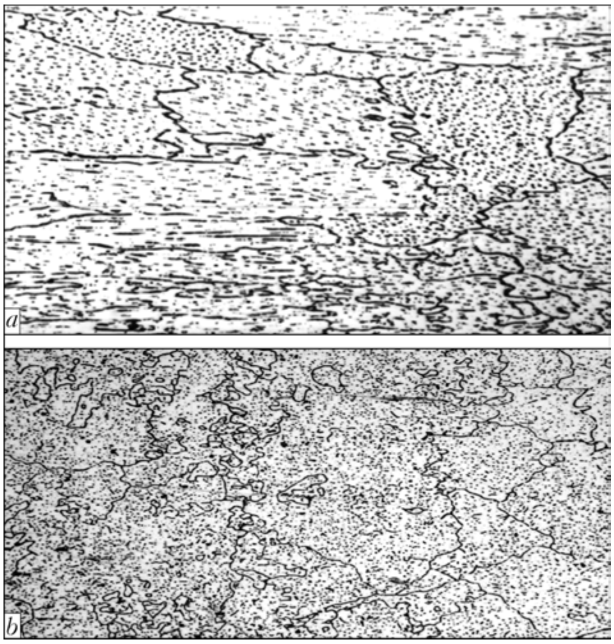

Figure 5. Microstructure of HAZ (a) and weld (b) metal in the EN AW-1050A aluminum alloy butt joints 1.5 mm thick at P = = 2.5 kW and v_w = 0.85 m / min (×200)

Table 3. Microhardness HV0.2 of the EN AW-1050A aluminum alloy joints

Thickness, mm	Ð, kW	v_w, m / min	Base metal			HAZ		
			Points acc. to Figure 3					
			1	*2*	*3*	*4*	*5*	*6*
0.8	1.5	1.10	33.6	36.4	37.1	27.1	25.8	26.6
	1.7	1.65	35.6	34.5	20.2	22.3	18.4	20.4
	2.5	1.85	37.1	36.4	33.6	23.0	24.9	24.5
	2.5	2.63	39.4	37.1	35.6	21.9	21.0	20.4
1.0	1.5	0.80	38.6	37.1	40.2	29.6	28.0	30.7
	1.8	1.35	42.0	39.4	38.6	27.1	26.6	24.9
	2.5	1.30	42.9	42.0	37.1	26.6	28.5	27.1
	2.5	1.90	43.8	42.0	38.6	30.7	28.5	28.0
1.5	2.0	0.70	39.4	36.4	23.0	24.9	22.6	25.3
	2.3	1.00	37.1	38.6	36.4	27.1	25.8	27.1
	2.5	0.85	40.2	40.2	27.1	29.6	29.0	28.0
	2.5	1.25	45.8	41.1	37.8	28.5	28.5	28.0

Table 3 (cont.)

Thickness, mm	Weld			HAZ			Base metal		
	Points acc. to Figure 3								
	7	*8*	*9*	*10*	*11*	*12*	*13*	*14*	*15*
0.8	25.3	28.5	28.5	25.8	26.6	26.2	22.6	24.5	35.6
	21.9	21.3	23.0	23.4	23.4	25.3	26.2	35.6	38.6
	28.5	28.0	25.8	26.2	22.3	22.6	28.5	37.1	37.1
	29.6	27.1	26.6	24.5	29.6	22.3	33.6	37.1	37.1
1.0	29.0	31.2	29.0	28.5	29.0	26.6	24.9	35.6	37.1
	26.6	23.7	24.1	27.1	25.3	24.5	22.3	38.6	42.0
	29.6	29.0	29.0	27.1	27.1	27.1	24.9	40.2	37.1
	33.0	30.7	30.1	31.2	29.6	28.0	42.9	43.8	38.2
1.5	25.3	26.6	26.6	27.1	25.8	25.3	39.4	42.0	42.9
	27.6	26.6	26.6	29.6	26.2	25.8	23.4	42.0	40.2
	28.0	24.9	27.6	27.6	27.6	27.6	26.2	37.1	42.0
	28.0	27.1	26.2	29.6	26.6	28.0	24.9	39.4	42.0

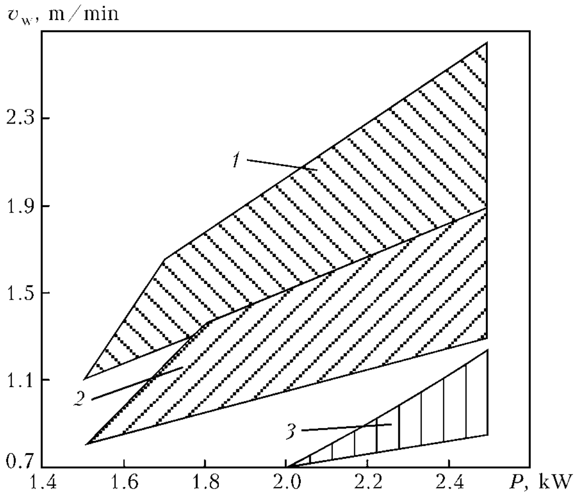

Figure 6. Range of optimal parameters for laser welding of the EN AW-1050A aluminum alloy butt joints 0.8 (*1*), 1.0 (*2*) and 1.5 (*3*) mm thick at the HPDL focal length of 82 mm and shielding gas flow rate of 10 l / min

Summary. Study of the HPDL welding of butt joints of aluminum alloy sheets EN AW-1050A 0.8, 1.0 and 1.5 mm thick showed that the black absorbent applied on the top surface of joint increases significantly the absorption of laser beam energy. Thanks to higher absorption of laser beam energy high quality joints can be produced in a wide range of laser parameters (see Table 2 and Figure 6). As a result of grains re-crystallization of the strengthened base metal, microhardness of HAZ metal is significantly lower than that of base metal, and also plasticity of HAZ and weld metal was increased (see Figures 3--5 and Table 3). During tensile tests the samples were breaking in the HAZ, and the tensile strength was at level of about 70 % of the of base metal strength (see Table 2). High plasticity of the joints was proven by bending tests carried out for bending from weld face side and also from weld root side. To ensure mechanical properties of the joints at the level not lower than those of base metal, heat treatment of the joints after laser welding is required [1]. To produce high quality butt joints of aluminum alloy sheets, prior to HPDL welding the edges of joints must be precisely prepared, and the top surface must be covered by black absorbent to increase the absorption of laser beam energy. Initial tests of HPDL-welded aluminum alloy sheets with activating flux ActivaTec 500, originally designed for GTA welding, showed that the welding speed can be additionally increase (up to 30 %) but the quality of joints was unacceptable because of oxide inclusions inside the weld metal. Further investigations of HPDL welding process will be concentrated on applications of activating flux ActivaTec 1000, originally designed for GTA welding of aluminum alloys.

1. (1996) *Materials and applications*: Welding Handbook. Part 1. Ed. 8. AWS, 257–306.
2. Miller, W.S. et al. (2000) Recent development in aluminum alloys for the automotive industry. *Mater. Sci. and Eng.*, A**280**, 37--49.
3. Klimpel, A. (1999) *Spawanie, zgrzewanie i ciecie metali*. Warszawa: WNT.
4. Pastor, M., Zhao, H., Martukanitz, R.P. et al. (1999) Porosity, underfill and magnesium loss during continuous wave Nd:YAG laser welding of thin plates of aluminum alloys 5182 and 5754. *Welding J.*, 78(**6**), 207--216.
5. Venkat, S.E., Albight, C., Rammasamy, S. et al. (1997) CO_2 laser beam welding of aluminum 574-O and 6111-T4 alloys. *Ibid.*, **7**, 275–282.
6. Bleidtner, J. et al. (2000) Experiments relating to deep welding using a fibre-contact high-power diode laser. *Schweissen und Schneiden*, 52(**4**), 78--83.
7. Klimpel, A. (1999) Lasery diodowe duzej mocy w spawalnictwie. *Przeglad Spawalnictwa*, **8**, 1--8.
8. Kuo, M., Sun, Z., Pan, D. (2001) Laser welding with activating flux. *Sci. and Techn. of Welding and Joining*, 6(**1**), 17--22.

UNIVERSAL ELECTRODES FOR WELDING HIGH-ALLOY STEELS IN ALL SPATIAL POSITIONS

Coated metallic electrodes of ANV-17U grade for manual arc welding of metal structures of austenitic class steels of 02Kh19N18G5AM3 type allows, unlike the known analogues, for example electrodes of ANV-17 grade, welding performance in all spatial positions, that is especially important in repair-restoration works. The new electrodes provide high technological strength and resistance of welded joints to intercrystalline corrosion, a good weld formation and easy removal of slag crust, stable burning and easy repeated ignition of the arc, small losses of electrode material for spattering.

Purpose and application. Electrodes ANV-17U are designed for welding of corrosion-resistant high-alloy steels of 03Kh16N15M3, 09Kh16N15M3B, 03Kh21N21M4GB types, used in production of caprolactam, carbide, etc.

Status and level of development. Technology of production has been mastered and electrodes are subjected to testing at the Customer enterprise.

Proposals for co-operation. Signing of contract for delivery of electrodes is possible.

Main developers and performers: Prof. Yushchenko K.A., Dr. Kakhovsky Yu.N., Dr. Bulat A.V., Group Head Samojlenko V.I.

Prof. Yushchenko K.A.
Tel./fax: (38044) 289 90 87, 287 10 88

INFLUENCE OF ESC PARAMETERS ON THE QUALITY OF RECONDITIONED GEAR TEETH

S.M. KOZULIN, **I.I. SUSHCHUK-SLYUSARENKO** and **I.I. LYCHKO**
E.O. Paton Electric Welding Institute, NASU, Kiev, Ukraine

Influence of the parameters of electroslag cladding on the penetration depth and thickness of skull crust was studied at reconditioning of the teeth of large-pitch gears by electroslag cladding. The obtained regression dependencies were used to plot the nomograms for establishing a quantitative relationship between the individual parameters of the mode.

Keywords: large-pitch gears, reconditioning, electroslag cladding, parameters, skull crust, penetration depth

Quality and performance of the teeth of large-pitch gears reconditioned by electroslag cladding (ESC), depend on a number of factors connected with the technology and technique of cladding.

The main indices of the teeth reconditioning quality are reliability of filler and base metal fusion, obtaining of the preset geometrical sizes of the reconditioned tooth profile, high mechanical properties of deposited metal and HAZ, as well as the quality of the reconditioned tooth working surface formation. The most important factor that provides the above mentioned requirements is the optimum mode that can be selected if qualitative and quantitative correlation of its parameters is known.

In view of the complicated configuration and geometrical sizes of involute profiles of the teeth being reconditioned, as well as their specific operating conditions, in order to select the optimum cladding parameters it is necessary to know the correlation of ESC mode parameters and their influence on the reconditioned teeth quality rather precisely. Ensuring of guaranteed fusion in transition fillets of the clad teeth, as well as producing a skull crust of a uniform and forecast thickness along the tooth profile perimeter and by its length become particularly important.

Experimental studies were done on full-scale specimens for derivation of the above dependences. Before that, the influence of mode parameters and kind of current, as well as the cladding technique on the stability of the electroslag process, was studied by experimental methods [1]. It is established that sufficient stability of the process and satisfactory formation of the deposited metal were achieved in DCRP cladding.

In this work, the influence of mode parameters on the penetration depth and thickness of skull crust was studied when reconditioning worn teeth by ESC with a consumable nozzle. The studies were carried out by the technique of experiment planning [2].

Analysis of the obtained experimental results showed that the most important parameters in ESC of the teeth by a consumable nozzle are cladding speed v_{cl} as a summarized index, slag pool voltage U, slag pool depth h_{sl}, distance from the electrode wire to the clad edge l, flux grade F and kind of current K. Indicated parameters were chosen as the factors for carrying out the experiments and determination of the regression dependences:

$$\delta_s = f(v_{cl}, U, h_{sl}, l, \mathrm{F}, \mathrm{K})\ [\mathrm{mm}];$$
$$h_p = f(v_{cl}, U, h_{sl}, l, \mathrm{F}, \mathrm{K})\ [\mathrm{mm}],$$

where δ_s is the thickness of skull crust; h_p is the penetration depth.

Unused mode parameters are taken to be constant by the optimum values or taken into account through the selected factors, for example, electric wire feed rate, v_f, and welding current are taken into account through the speed of cladding v_{cl}.

The method of construction of a fractional factor experiment, applying 1 / 8 replica of the type 2^{6-3} from the complete factor of the experiment of 26, was used for reducing the number of tests [2].

The levels of the factors were set in the real reproducible cladding modes. Parameters were varied in the following ranges: v_{cl} = 0.6–1.0 m / h; U = 46–52 V; h_{sl} = 45–55 mm; l = 20–30 mm. The experiments were conducted at alternating and direct currents of reverse polarity using fused fluxes AN-8 and AN-9U.

Laboratory installation (Figure 1) was designed and fabricated for performing experimental investigations. It includes a working table for fixing the gear to be reconditioned, suspension and mould moving unit, device for fastening the inlet recess on the workpiece, etc. ESC was done by batch-produced unit A-535. Transformer TShS-3000-3 and rectifier VSZh-1602 were used for power supply to the unit.

Tests were carried out on full-scale specimens of worn crown gears of cement mill (teeth modulus — 27, teeth quantity — 22, gear diameter — 420 mm, material — steel 40X). Worn teeth were cut out by anode-mechanical method before cladding, leaving part of tooth flank of the height of 0.25 of tooth modulus.

Consumable nozzle plates (Figure 2) were manufactured of steel St3, and tightly wound springs from 3 mm welding wire of grade Sv-08GA served as the guides for filler wire feeding.

Water-cooled mould manufactured from a solid copper blank, was used as the forming tooling. Longitudinal channels were drilled out in the blank for cooling it with water. Cooling mode of the mould was

© S.M. KOZULIN, I.I. SUSHCHUK-SLYUSARENKO and I.I. LYCHKO, 2006

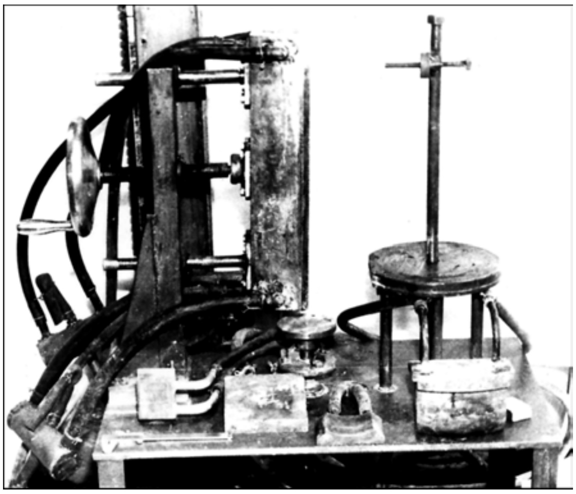

Figure 1. Appearance of laboratory installation for ESC of the teeth by consumable nozzle

controlled by the method of measuring capacity [3]. Water temperature at the mould inlet and outlet was checked by mercury thermometer (measurement accuracy of ± 0.5 °C). The following cooling mode was continuously maintained during all the experiments: water flow rate of 14–16 l / min; temperatures difference at inlet and outlet of 10–12 °C.

Experimental ESC was carried out on alternating current and direct current of reverse polarity. Welding wire Sv-18KhMA and fused fluxes AN-8 and AN-9U that are widely used for electroslag welding of carbon and alloyed steels, were applied. Flux AN-9U has reduced content of SiO_2 that is favorable for increasing the temperature of the flux boiling start [4] and improving the ESC stability.

The latter becomes especially important, when the process is carried out in a water-cooled mould, as well as when manufacturing small cross-section profiles by ESC. Good metallurgical properties of AN-9U flux provide high quality of the metal of a weld made on alloyed steels of higher strength [4] that is very important at reconditioning the teeth of large-pitch gears. Lower viscosity compared to AN-8 flux, achieved due to increased content of CaF_2 in it, permits obtaining a thinner skull crust on water-cooled working surfaces of the mould that is required for providing a high accuracy reconditioning of teeth profile.

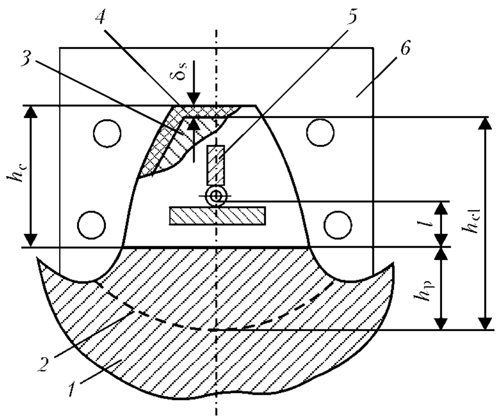

Figure 2. Diagram for measurement of skull crust δ_s, distance from electrode to clad edge l and penetration depth h_p: *1* — reconditioning gear; *2* — fusion zone; *3* — deposited metal; *4* — skull crust; *5* — consumable nozzle; *6* — mould (for other indications see the text)

Electric parameters of the mode were recorded on the chart strip by automatic recording instruments N-392 and N-390.

Mean values of skull crust thickness, δ_s, were found as a simple average of six measurements of skull bits thickness, taken from different sections of the teeth reconditioned surface (see Figure 2). Measurements were done by micrometer caliper (error of ± 0.01 mm).

The mean values of base metal penetration depth, h_p, were determined in the following way. The measurements of height of cut out teeth parts, h_c, were taken after cutting out worn teeth (see Figure 2). After teeth cladding, transverse templates were cut out every 70 mm along the teeth length from the gear body. Transverse macrosections (Figure 3) were cut out of the templates and the height of deposited metal h_{cl} (see Figure 2) was measured by the configuration of fusion line (zone). Values of penetration depth h_p, were calculated from the expression

$$h_p = h_{cl} + \delta_s - h_c \text{ [mm]}.$$

The following regression equations were derived after experimental data processing and evaluation of statistical value of regression coefficients by Student criterion [2] for confidence level of 0.95 and number of degrees of freedom equal to 16:

$$\delta_s = 0.275 v_{cl} - 0.0275 U - 0.26 F + 2.0755; \quad (1)$$

$$h_p = 0.813 U - 7.815 v_{cl} - 0.1126 l + 0.5625 K - 3.817. \quad (2)$$

Absence of parameter h_{sl} in expressions (1) and (2) can be explained by that the influence of slag pool depth on skull crust thickness δ_s and penetration depth h_p turned out to be statistically insignificant in the accepted interval of variation.

Testing by Fisher criterion showed that model parameters do not contradict the hypothesis of adequacy for confidence level of 0.95. When calculating regres-

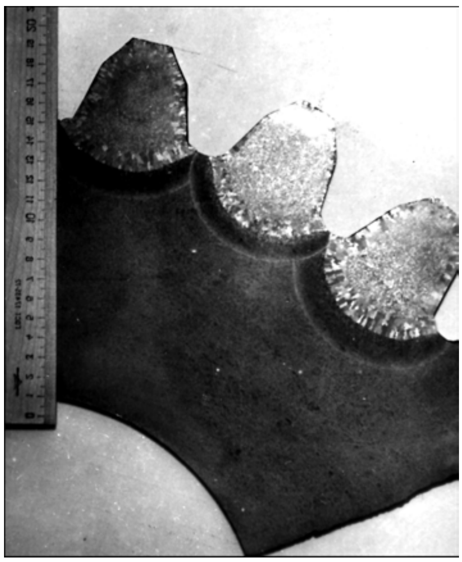

Figure 3. Transverse macrosection of the clad teeth

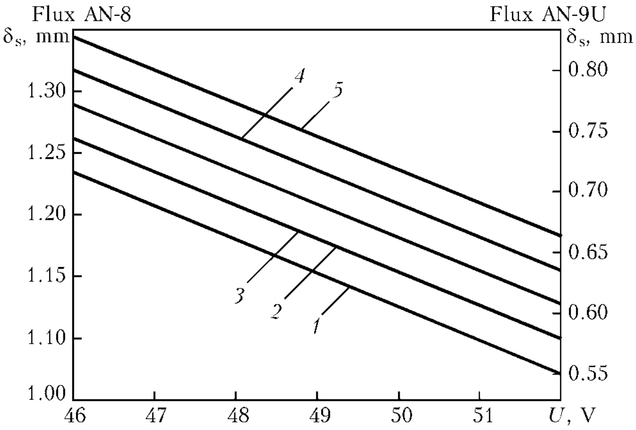

Figure 4. Nomograms for estimation of skull crust thickness δ_s depending on slag pool voltage U, cladding speed v_{cl} and flux grade: *1* — v_{cl} = 0.6; *2* — 0.7; *3* — 0.8; *4* — 0.9; *5* — 1.0 m / h

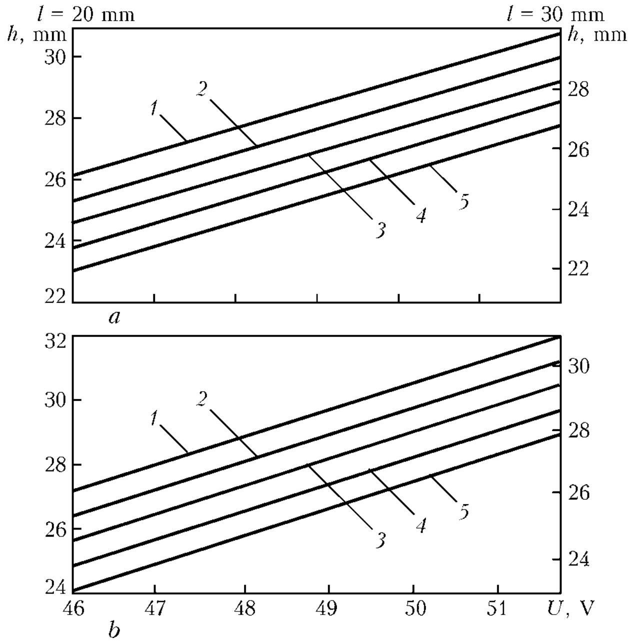

Figure 5. Nomograms for estimation of penetration depth h_p depending on slag pool voltage U, cladding speed v_{cl}, distance from electrode to clad edge l and kind of current, obtained at alternating (*a*) and direct (*b*) current: *1–5* — see Figure 4

sion coefficients by (1) and (2), mean root square errors were equal to 0.00036 and 0.05859, respectively, that is quite admissible at definition of indicated above parameters at ESC.

Proceeding from expressions (1) and (2), nomograms were built for determination of skull crust thickness depending on the slag pool voltage, cladding speed and flux grade (Figure 4), as well as maximum penetration depth, depending on slag pool voltage, cladding speed, distance from the electrode to the edge being clad and kind of current (Figure 5).

As it is seen from Figure 4, the thickness of skull crust decreases with the increase of slag pool voltage U and increases with increase of cladding speed v_{cl}. It can be explained by that the thickness of skull crust formed on the wall of a mould, is known to be determined by ESC parameters, i.e. by the conditions of heat supply from slag pool to skull crust and heat sink into the system of mould cooling [3, 4]. Meantime, the skull crust surface from the side of slag pool plays a part of mobile phase boundary. In quasi-stationary mode, heat supply from molten slag to phase boundary is equal to heat sink from it to cooling water. Heat flow to the mould wall increases at increase of voltage, i.e. more heat is supplied to the phase boundary than is removed from it. As the phase boundary temperature cannot change [4], partial melting of skull crust takes place that leads to the decrease of its thermal resistance and increase of heat sink. After this, the balance sets in between the supplied and removed heat, but the skull crust is already thinner.

With increase of cladding speed specific heat input of ESC process decreases, heat flow to water-cooled mould wall decreases, heat balance that forms with a thicker skull crust, is disturbed. It was established that when the slag pool voltage increases, the thickness of the skull crust decreases by a linear dependence, and when the cladding speed rises, it also increases practically by a linear dependence (see Figure 4). When using AN-8 flux, the thickness of skull crust obtained at the same parameters, is almost by 40 % thicker that in the case of AN-9U flux.

From Figure 5 it is evident that the depth of penetration increases at increase of the slag pool voltage, decrease of the cladding speed and distance from the electrode to the edge being clad. U has the biggest influence on it. Moving the electrode away from the edge within the limits of specified variation interval (10 mm) changes the penetration depth of the base metal by not more than 4 %. At DCRP ESC, the penetration depth is on average by 4.3 % greater than that at alternating current with the similar cladding modes.

Comparison of design values with the results of experiments on ESC for teeth with 22–23 modules showed their satisfactory agreement. The error did not exceed 10 % that is quite acceptable for engineering calculations.

CONCLUSIONS

1. When DC ESC is performed, the quality of deposited metal formation is considerably improved, the range of admissible fluctuations of mode parameters and the penetration depth increase.

2. Established dependences allow rather precisely forecasting the geometrical parameters of involute profile of the reconditioned tooth, when designing the forming fixtures that in some cases enables eliminating machining of working surfaces after their cladding.

3. Use of flux AN-9U is preferable when reconditioning the teeth of large-pitch gears by ESC.

4. Established quantitative dependences of cladding mode parameters are suitable for calculation of optimum parameters of ESC of teeth with 22–23 modules.

1. Kozulin, S.M., Lychko, Ig.I. (1987) Electroslag cladding of teeth of large-module gears. *Avtomatich. Svarka*, **3**, 62–64.
2. Spiridonov, A.A., Vasiliev, N.G. (1975) *Experimental design*. Sverdlovsk: S.M. Kirov UPI.
3. (1978) *Thermal processes in electroslag remelting*. Ed. by B.I. Medovar. Kiev: Naukova Dumka.
4. (1980) *Electroslag welding and cladding*. Ed. by B.E. Paton. Moscow: Mashinostroenie.

COOPERATION RAISES INVESTIGATION EFFICIENCY AND REDUCES COSTS

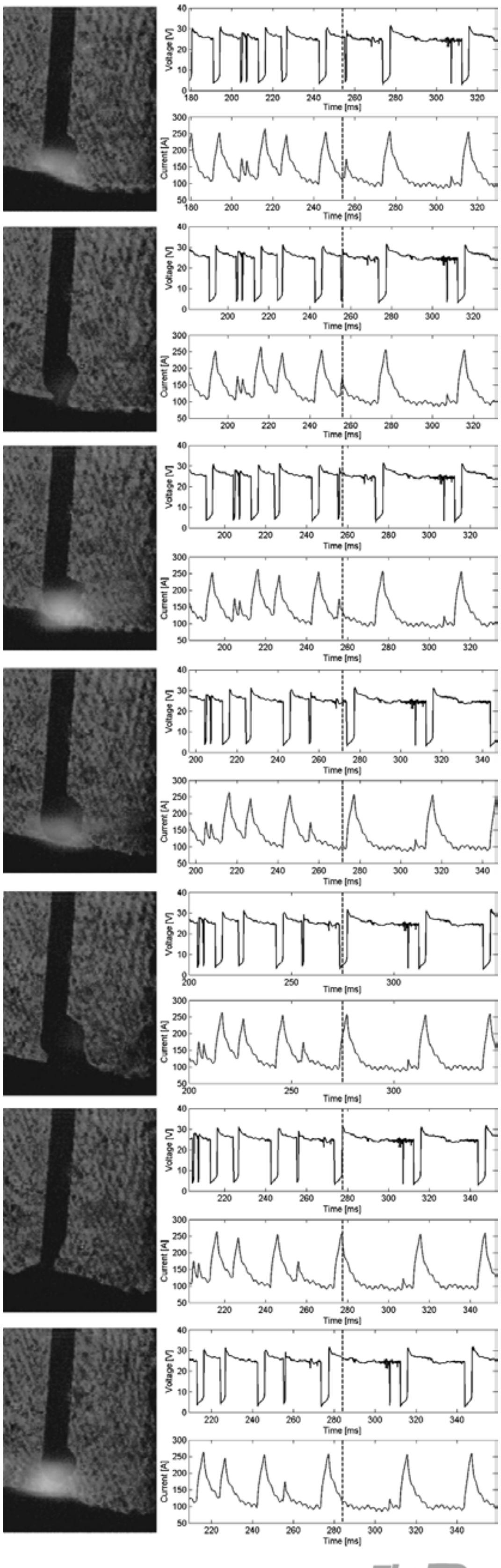

The arc behaviour and the metal transfer mode are ones of the most important factors determining welding quality (first of all, weld geometry and spatter generation rate). These factors data contribute to enhance operational features of power sources to be modernised as well as of ones under development, wire feeders and welding consumables. That is why video filming of the arc area is always desirable.

This technique becomes even more efficient being combined with synchronised registration of the voltage and current curves and when these two kind of data (video images and curves) are presented in combination as it is shown in the Figure on the right.

But only a few welding research centers worldwide can afford 70–100 US$ spending to be equipped with such laboratory installations (see the left Figure on the next page: *1* — high-speed video camera; *2* — arc voltage and welding current curves registration computerised system; *3* — light source (a laser); purpose developed software). Especially if we take into consideration that the rate of use of such a system does not exceed 1–2 days per month.

A way out from this situation is cooperation between welding research centers with mutual benefit as for those who need to conduct such investigations as for those who possess such facilities.

The cooperation between the E.O. Paton Electric Welding Institute Training and Qualification Center — PWI TQC (Ukraine) and the Federal University of Uberlandia — UFU (Brazil) may serve as an example of such a collaboration. The welding department of this university (LAPROSOLDA) is equipped with a complete set of a lab ware to conduct synchronized video filming of the arc area (see the right picture on the next page).

High-speed video cameras giving frame rate up to 2000 fps are used to present day. But recently a high-speed video system allowing frame rate up to 20000 fps has been purchased. Resolution, frame rate and recording time are interdependent. For example, a reduction in frame rate and / or resolution will increase recording times.

High-speed video recording systems can be used in research, test and production areas. Application of such lab ware allows conducting comprehensive and detailed examination of power source, wire feeder, and welding consumable operational features. For welding equipment and consumables producer it turns to be possible to demonstrate, for instance, that such-and-such power source or electrode wire provides with proper arc stability and favourable metal transfer mode. Such techniques allows finding out causes of,

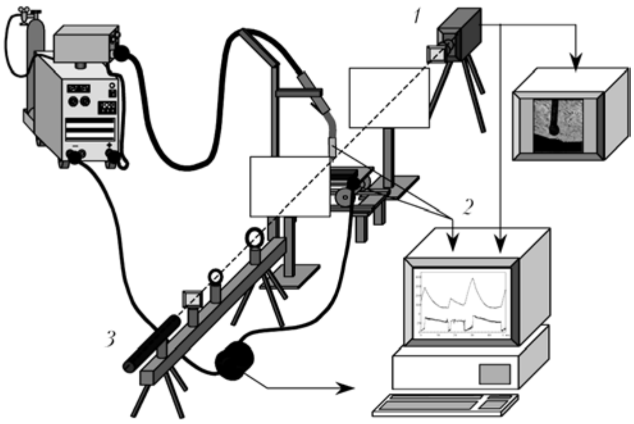

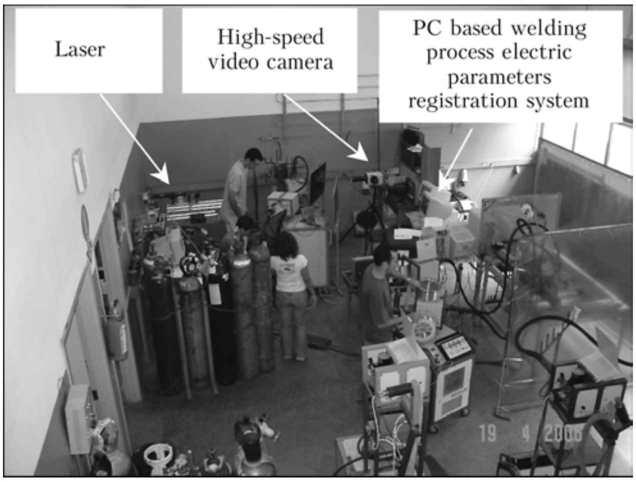

e.g. elevated spatter generation rate, arc instability and other welding process disturbances.

Besides of PWI TQC the other companies and firms, like OJSCs Electromachine-building plant «Firm SELMA» (Ukraine), Engineering-Technological Center «PROMETEJ» (Russia) and others are taking part in this cooperation.

Financial expenditure of partners of this cooperation is minimized due to the fact that the main interest of Brazilian colleagues is to conduct joint research works and then to publish papers in leading welding journals as it takes place with regards to «The Paton Welding Journal» where papers of authors from PWI and UFU are being published in a regular way.

PWI representatives are ready to render consulting and mediatorial assistance to institutions willing to joint this cooperation.

Our contact address:
The E.O. Paton Electric Welding Institute
Training and Qualification Center
11, Bozhenko str., Kiev, 03680, Ukraine
Tel.: (+380 44) 456 63 30
Fax: (+380 44) 456 48 94
E-mail: ponomarev@ukr.net

V. Ponomarev

PLASMA HARDFACING OF PARTS OF PIPELINE STOP VALVES AND PUMPS

At the Engineering Center of Wear-Resistant Coatings of the E.O. Paton Electric Welding Institute the technology, equipment and electrode materials have been developed for plasma hardfacing of shafts, rods, slide valves, piping stop valves, bushings and pump shafts and other components of the petrochemical equipment.

Installation of UD-417M type has been designed for plasma hardfacing allowing deposition of parts of type of a shaft of 30–300 mm diameter and 50–800 mm length using filler wire of 1.2–3.6 mm diameter. Dimensions of the installation: 1680×350××1750 mm. Mass — 600 kg. Power source — VDU-506.

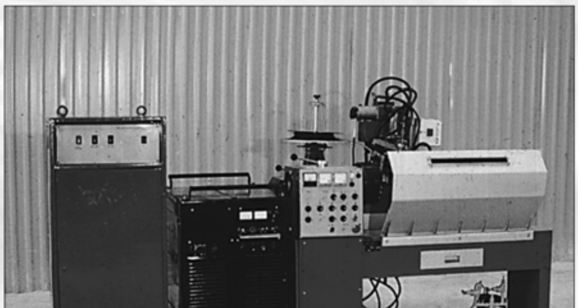

As electrode materials, the flux-cored wires PP-AN133, PP-AN157, PP-AN177, etc. are used. Technology of hardfacing provides: small share of parent metal in deposited layer; negligible welding deformations; good formation and high quality of deposited layer; required composition and properties of metal in the first deposited layer.

Proposals for co-operation. The Engineering Center of Wear-Resistant Coatings is fulfilling works on the contract base for the development of electrode materials and technological procedures of hardfacing; provids delivery, setting-up, putting into operation and implementation of installations UD-417M.

Contacts: Dr. Eremeev V.B.
Tel.: (38044) 287 89 48, 289 15 56